Analysis and Design for Quasi-Optical Structures

Thesis by

Polly Preventza

In Partial Fulfillment of the Requirements

for the Degree of

Doctor of Philosophy

California Institute of Technology

Pasadena, California

1999

(Submitted May 21, 1999)

To my parents and the memory of my uncle, Theodoros Papayianopoulos

Acknowledgements

First, I would like to thank my advisor, David Rutledge, for his support, guidance and advice. His insight and vision were priceless during my staying at Caltech, and I will endeavour to develop similar qualitites through the rest of my career. I am indebted to Mehran Matloubian, who fabricated the devices at Hughes Research Labs. I also wish to thank Emilio Sovero for his prompt response and efforts to help expedite my work in the modeling of grid amplifiers. For the fabricating efforts of the beam steering grid, I would like to thank Rob Mihailovich at Rockwell Science Center. Many thanks go to Jim Rosenberg for his suggestions and interesting conversations.

I am glad to have had the opportunity of knowing and working with many talented people at Caltech. I would like to thank Blythe Dickman not only for his great assistance with the quasi-optical measurements but also for his sincere friendship and our never-ending philosophical and religious discussions. I cannot imagine how I could have gone through this effort without the close friendship and support of John Davis. I will always remember our late-night hilarious discussions. I wish John the best of luck in his new job. I would like to thank Alina Moussessian who was a good example of quiet-strength and focus. Many thanks go to Mike De Lisio for his suggestions and the groundwork he laid for the modeling of the grid amplifiers. Great appreciation goes to Kent Potter, Irene Loera, Connie Rodriguez, Carol Sosnowski, Dale Yee, Dragan Maric, Jung-Chih Chiao, Victor Lubecke, Bob Weikle, Jon Hacker, Moonil Kim, Shi-Jie Li, Cheh-Ming Liu, Ute Zimmerman, Lee Burrows, and John Wright. To the newer members of the group, Lawrence Cheung, Scott Kee, Paul Khan, Ichiro Aoki, I wish them all the best. I have enjoyed meeting with many visitors to the MMIC group, including Ken Ichiro Natsume, Kazuhiro Uehara, Minoru Saga, Taavi Hirvonen, and Toshihisa Kamei. Great appreciation go to Prof. Bossaerts; it was

through his classes that I saw the opportunity to merge my technical background with a career in finance.

I have met two of my best friends throughout these years: The fun-loving, sharp and multifaceted Thanos Papadimitriou and the really "cool" Christos Kritikos. I thank them both for being my partners "in crime" all these years. Many thanks go to Jocelyn Pradeau for a very unique life experience. I would like to pay special tribute to my favourite roommates and very good friends George Mitsis (the artist) and George Panotopoulos (the engineer) for the terrific parties and for giving a positive meaning to the dull words "everyday routine". Many thanks go to the very good friends Konstantina Kioussis and Teddy Rellos. I only wish I had met them six years ago when I first came to US. I would also like to thank Chris Dellarocas for his advice and inspiring conversations. I am also thankful to Yiannis Anagnostakis for keeping my travelling spirit alive and kicking. Lila Yianopoulou and Nathalie Vovou deserve special thanks for always keeping me informed about the goings-on back in Greece. I will always remember my spinning instructor Kelly for her motivation and high energy. I will never forget Utta's healing power. Special thanks go to my friend Mike Sarris who helped me smooth out the difficulties of the last year and the frustrations of the job search.

Now I would like to give a special message to my immediate family. My beloved sister, Rania, has been a huge inspiration to me throughout my Ph.D program by teaching me never to give up. She is definitely the most determined person I have ever met in my life. I want to express my gratitude to my brother Thanos for his live and optimistic spirit and his new wife, Paroula, who always adds a touch of calm and serenity to our family. Finally I would like to thank my parents, Katerina and Alkiviadis for their truly unconditional support and love. Without their understanding and help this endeavour would have not been possible.

Everything you can imagine is real

— Pablo Picasso

You lost money, you lost nothing

You lost your pride, you lost something

You lost your courage, you lost everything

— Greek Philosopher

Analysis and Design for Quasi-Optical Structures

Abstract

Quasi-optical power combiners such as quasi-optical grids provide an efficient means of combining the output power of many solid-state devices in free space. Unlike traditional power combiners no transmission lines are used, therefore, high output powers with less loss can be achieved at higher frequencies. This thesis will detail three quasi-optical grids and their modeling. Two new models for analyzing quasi-optical grid amplifiers based on a finite-element simulator (HFSS) are presented and their validity is tested. A 36-element Ka-band grid amplifier is also described. The grid uses Flip-Chip InP HEMT's and has a peak gain of 4.8 dB at 36 GHz. A beam-steering method which includes microelectromechanical (MEM) switches on an insulating membrane is presented. The arrays are fabricated monolithically on highly- doped silicon by Rockwell Science Center. Processing challenges in fabricating the structures will be discussed. Measurements of s-parameters of capacitive arrays (Off state) are made and give promising results for the beam-steering grid. The design, construction and performance af a 36-element hybrid gid oscillator is also presented. The active devices are InP-based HEMT's. A locked frequency spectrum was achieved, with a Peak Effective Radiated Power (ERP) of 200 mW at 43 GHz. The grid is designed to minimize the substrate-mode power and produce an E-field with low side-lobes.

Contents

Chapter 1

Introduction

Millimeter-wave and sub-millimeter-wave systems, between 30 GHz–3 THz, have been an active area of reasearch in recent years. The field has benefited from the development of solid-state devices for up to 100 GHz. Millimeter-waves allow for smaller and lighter components as well as larger bandwidth than microwaves and a variety of commercial and military applications have been proposed and developed. Military applications include passive and active imaging systems, ground- or ship-based radars, and missile seekers. Commercial applications include automotive radar and collision-avoidance systems, personal communication systems, Wireless Local Area Networks (WLAN's) [1,2], navigational aid for aircrafts and ships [3,4]. Submillimeter-waves can also be used in atmoshperic remote sensing [5].

1.1. QUASI-OPTICAL POWER COMBINING

Vacuum electronics are still the dominant technology for power applications in the millimeter-wave region. On the other hand, the rapid development of many solid-state devices such as IMPATT's, Gunn diodes, RTD's, HBT's, GaAs pHEMT's, and InP-based HEMT's promises an inexpensive and more attractive way for the millimeter-wave systems. However, solid-state devices have low output power. For high power systems many individual devices must be combined. Circuit-based power combining techniques [6–9] have excellent performance in

the low- microwave region but they have serious limitations at higher frequencies. As the operating frequency increases, manufacturing difficulties, and conductor losses in waveguides or transmission lines, make the circuit-combining systems unpractical. Spatial or quasi-optical power combining methods address these difficulties. James Mink [10] proposed the use of quasi-optical power combining technique to combine the output powers of many solid-state devices in free space. This technique eliminates the transmission-line and waveguide losses, and is suitable for monolithic fabrication. Many quasi-optical devices have been developed in the past decade, including amplifiers [11–35], oscillators [36–45], phase shifters [50,51], multipliers [47–49], and mixers [46].

1.2. TECHNIQUES FOR MODELLING ACTIVE ARRAYS AND GRIDS

Clearly the first step required to analyze a quasi-optical array is to analyze the passive structure for a given excitation field. Once the array impedance is calculated, standard circuit design software, like Puff or HP's MDS can be used to simulate the interaction of the active devices in the array. Finite passive grids and arrays can be modeled using moment-method techniques, (EMF), three dimensional finite difference time-domain analysis, (3D-FDTD), and finite-element methods, (HFSS).

For simple geometric metal patterns like strips or bow-ties, the embedding impedance presented to the terminal of the devices can be calculated by the EMF analysis. The method is developed by Weikle [52] and De Lisio at Caltech [53]. The method assumes a two-dimensional infinite array with a uniform plane wave normally incident on it. Certain boundary conditions are imposed by the symmetry of the grid. Therefore, the analysis of the infinite array is reduced to a simpler analysis of the equivalent unit-cell with electric walls on the top and bottom and magnetic walls on the side (Fig. 1.1). Weikle assumed a constant surface current distribution on the strip while De Lisio used the method of moments to obtain a

more accurate approximation of the strip current.

(a)

(b)
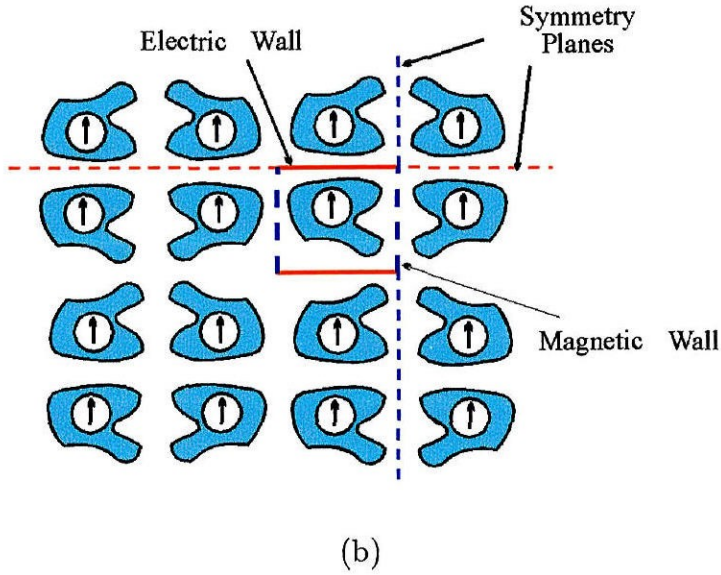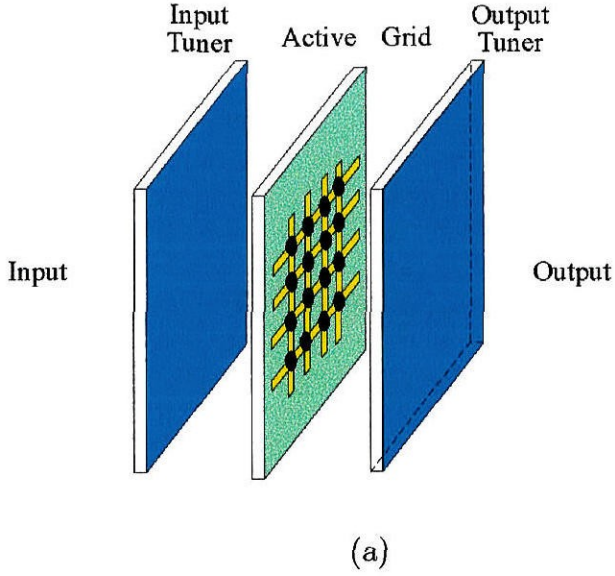
Fig. 1.1. (a) Perspective view of a quasi-optical grid. The active grid consists of an array of solid-state devices integrated on a metal grating and (b) Planar grid with two symmetry planes. The horizontal symmetry plane can be replaced with an electric wall and the vertical symmetry plane with a magnetic wall.

Once the current distribution on the metal strips is known, the impedance the structure presents to the incident wave is calculated by:

$$Z_{in} = -\frac{1}{I_o^2} \iint_{cell} \bar{E}_t \cdot \bar{J}_t \, dS. \qquad (1.1)$$

where I_o is the current in the strip. The EMF method has been applied successfully to the analysis of many grids [37–39,54]. It is evident from the discussion above that the EMF method relies on knowing the currents on a given radiating structure. As a result the method is primarily used for simple configurations on which the current distribution can be assumed with reasonable approximation. Another technique that assumes an infinite array is the full wave analysis. This technique does not depend on knowing the current distribution; it therefore allows for the analysis of more complicated structures. Two grid oscillators were designed using the full wave method [54]. The method is described in detail in [55].

Three-dimensional finite difference time-domain techniques have also been applied to analysis of grid structures [56–59]. A detail description of the method is beyond the scope of this thesis, and details could be found in [60,61]. FDTD handles complex metal patterns, inhomogenious dielectrics, ohmic losses, and edge diffraction.

The simulation technique used extensively throughout this thesis to model the two-dimensional periodic grid structures is the High Frequency Structure Simulation (HFSS). HFSS is a finite element method that calculates the full three-dimensional electromagnetic field inside a structure from which s-parameters are computed. The finite element method divides the full problem space into thousands of smaller tetrahedra (elements). The tetrahedra collection is called the mesh. There is a trade off between the size of the mesh, the accuracy and the computing capabilities. The accuracy depends on the size of the mesh. Meshes with thousands of elements give more accurate solutions than meshes with few elements. First, a solution is generated based on an initial mesh and then the

mesh is refined during an iterative process. When the s-parameters converge to a desired limit, the process stops and the solution is computed over a range of frequencies. Since generating a solution involves a matrix inversion with as many elements as there are tetrahedra nodes, significant computing power and memory must be available. HFSS version 1.0 was extremely slow in calculating the s-parameters for simple structures. Also it did not provide lossy materials. HFSS version 2.0 and 3.0 permitted lossy materials or resistor-type boundary conditions, but still it was extremely slow and it was used for strictly simple structures. The simulations in this thesis were carried out using ANSOFT HFSS version 5.0. This version drastically reduced the disk and memory usage and the CPU time. As a result more sophisticated metal patterns, lossy materials, and multilayer array geometries can be modelled more accurately. In version 6.0 manual refinement of the mesh is a new valuable feature. If there are very small dimensions in a large area and if the adaptive refinement would take too long to recognize it, the user could manually refine the mesh around it. Since the accuracy of the equivalent unit cell simulation depends on the assumption of a uniform array excitation and infinite periodic structure, the HFSS method ignores substrate mode and edge effects.

1.2. QUASI-OPTICAL GRID AMPLIFIERS

Quasi-optical grid amplifiers have been an active research area in recent years. Both hybrid and monolithic approaches have been exploited. A pair of transistors with orthogonal input and output lines form the unit cell as shown in Fig. 1.2. A horizontally polarized input beam excites rf currents on the horizontal gate leads. The output currents run in the vertical direction. These currents produce a vertically polarized output beam to the right. The polarizers tune the input and output circuits independently and they provide good input-output isolation. The first quasi-optical grid amplifier was developed by M. Kim *et al.*

[11] at Caltech. This was a 25-element MESFET grid amplifier. A 100-element HBT grid amplifier was also developed by M. Kim at Caltech [12]. Monolithic differential-pair chips were used by De Lisio in a 100-cell array [15]. A Similar design has been utilized for a 36-element monolithic amplifier grid operating in the 44 to 60 GHz range [19]. All these designs used crossed-dipole antennas for the input and output. A 16-element self-complimentary MESFET grid was developed by A. Moussessian [35]. This grid, unlike previous grid amplifiers, did not require differential-pair transistors, but used single transistors as active devices for each unit-cell.
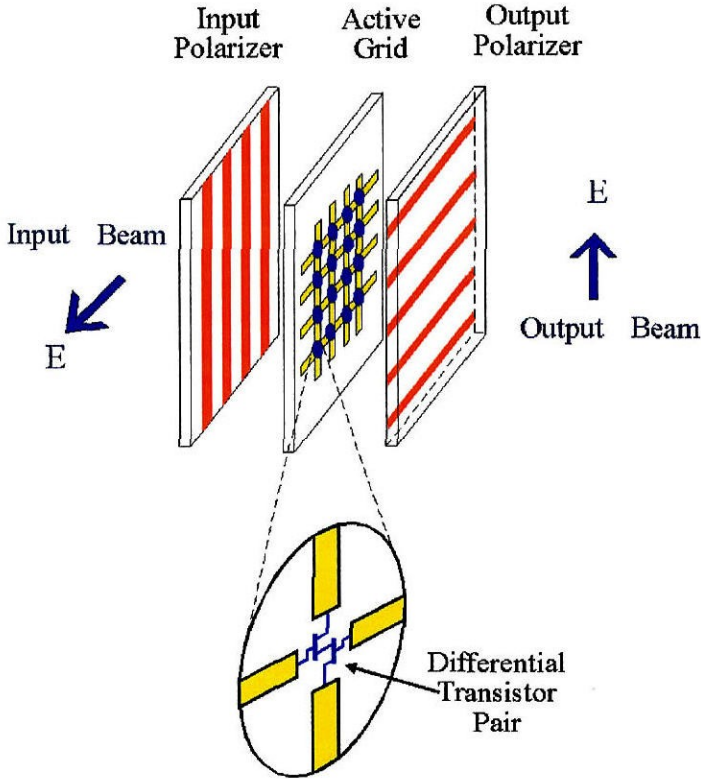
Fig. 1.2. A grid amplifier. The input beam is horizontally polarized and it enters the grid from the left. The output beam is vertically polarized and is radiated to the right.

# of transistors	Type	ETP	Freq. (GHz)	Gain (dB)	Efficiency (%)	Reference
512	pHEMT-Monolithic	5.3 W	35	9	13	B. Dickman, unpublished
	power MESFET	25 W	35	11		Hubert *et al.* [71]
112	pHEMT-Monolithic	2.9 W	38	9	8.3	E. Sovero *et al.* [70]
72	HBT-Monolithic	670 mW	40	5	4	C.-M. Liu *et al.* [18]
72	pHEMT-Monolithic		44 60	2.5 6.5		M.P. De Lisio *et al* [19]

Table 1.1. Quasi-optical Ka-band grid amplifiers.

Other types of quasi-optical amplifiers have been developed using patch antennas for the input and output [23-30], slot antennas [31-33,70] and probe antennas [22]. Table. 1.1 summarizes the performance of Ka-band grid amplifiers.

## 1.2. QUASI-OPTICAL GRID OSCILLATORS

A grid oscillator is shown in Fig. 1.3. It is a periodic, strongly coupled, oscillating structure based on integrating active devices directly into a planar array. The dc bias is fed along the horizontal leads. The radiating leads run in the vertical direction and the output beam is vertically polarized. The mirror provides feedback and it helps the devices to lock together. The first quasi-optical grid oscillator was developed at Caltech by Z.B. Popović, M. Kim and Rutledge [37]. Quasi-optical grid oscillators have been successfully reported [36–45].

metal mirror   active grid   dielectric tuning slab

E

Output Beam
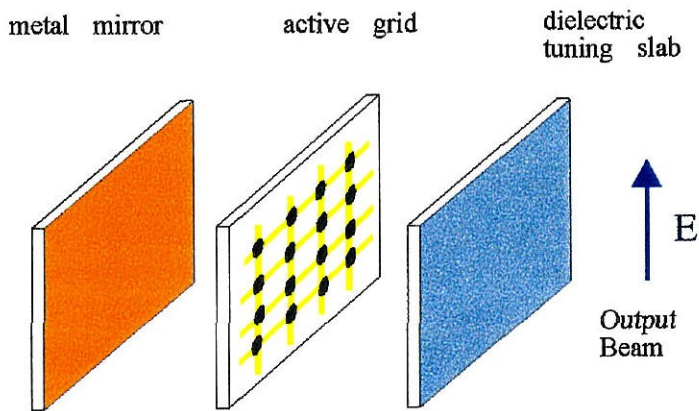
Fig. 1.3. A grid oscillator. The mirror and the dielectric slab provide tuning and help the devices to lock together.

1.3. QUASI-OPTICAL BEAM STEERING GRIDS

Quasi-optical monolithic diode-grids were first used as beam controllers [62-66].

30.00 μm
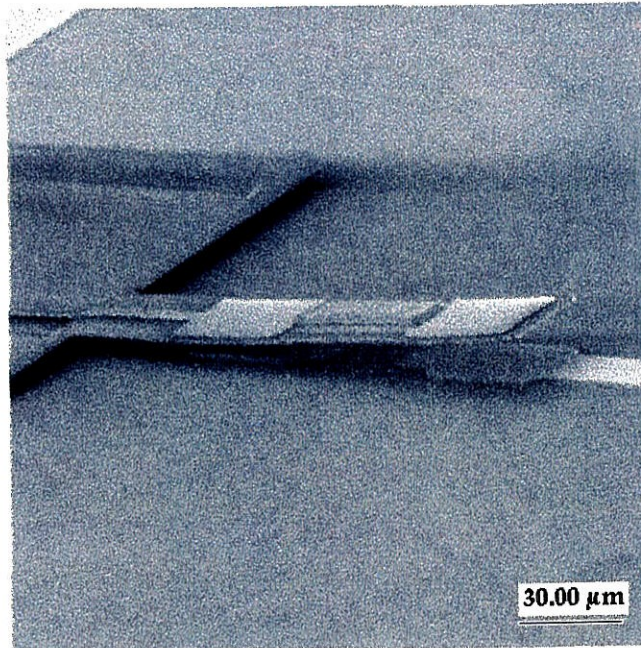
Fig. 1.4. A SiO_xN_y-membrane microswitch on silicon.

Type	Frequency (GHz)	No. of diodes (Schottky Varactor)	Phase shift	Reflection Loss	Reference
Reflection	93	1600	70°	6.5 dB	W. Lam *et al.* [62]
Reflection	120	7168	70°	3.5 dB	L.B. Sjogren *et al.* [63]
Reflection	60	7100	130°	2.7 dB	X. Qin *et al.* [66]

Table 1.1. Quasi-optical diode beam steering grids.

Table 1.2 summarizes the quasi-optical diode beam steering grids. Even though the diode-grid results are impressive, the series resistance of the Schottky diodes increases with the operating frequency thereby causing serious loss problems at sub-millimeter wavelengths. A new approach has been attempted by J.-C. Chiao at Caltech [67,68] that is based on passive elements instead of active devices which offer the advantage of low series resistances. The passive elements are microelectromechanical (MEM) switches on an insulating membrane. Switches developed by Yao [69] at the Rockwell Science Center have an electrical isolation of 50 dB and an insertion loss of 0.1 dB at 4 GHz. Fig. 1.4 shows a SiO_xN_y-membrane microswitch on silicon. By applying bias on the electrodes, the cantilever bridge experiences an electristatic force to bend the membrane downward until the electrodes contact. The stress of the membrane will separate the contacts when the bias is removed. The concept of a microswitch beam steering grid is shown in Fig.1.6. A vertically polarized wave is incident from the left, passe through several layers of microswitches and waveguides, and transmit with deflected angle on the right. Different settings of microswitches add different phase shifts to the propagating waves.
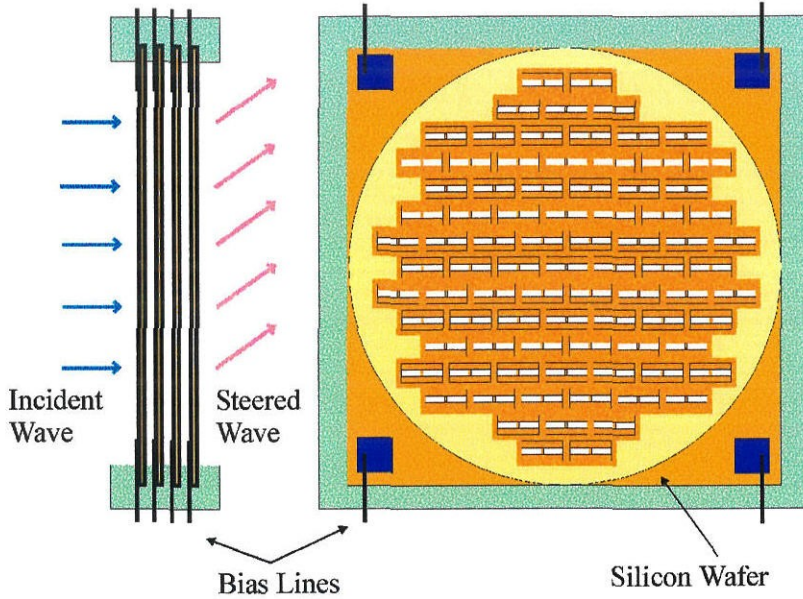
Fig. 1.5. The concept of a microswitch beam-steering grid. The incident wave enters on the left, passes through several layers of microswitches and waveguides and transmits on the right.

1.3. ORGANIZATION OF THE THESIS

Chapter 2 describes two new models for analyzing quasi-optical grid amplifiers based on a finite-element simulator (HFSS). Both the lumped-element equivalent circuit and the *s*-parameter model include mutual coupling effects and are an extension of the unit-cell transmission line model developed by De Lisio it et al. at Caltech [53,15]. These new models agree very well with previously published measurements [15]. The validity of the models is verified by measuring the *s*-parameters of three passive structures with different loads.

Chapter 3 discusses a 36-element Ka-band grid amplifier. The grid uses flip-chip InP HEMT's as the active devices. These chips were custom-made by Hughes Research Labs, Malibu. The initial measurements show that the grid had a 3 dB gain at 35 GHz.

In chapter 4, a beam-steering method which includes microelectromechan-ical (MEM) switches on an insulating membrane will be discussed. The arrays are fabricated monolithically on highly-doped silicon wafers by Rockwell Science Center. In this chapter, HFSS simulations of a 35 GHz and a 94 GHz 6-layer 2-bit controlled structure are carried out. The chapter will also describe the pro-cessing challenges in fabricating the structures. Measurements of s-parameters of a rectangular-window array with capacitive metal patterns are made to verify the resonant frequencies.

Chapter 5 discusses the design, construction and performance of a 36-element hybrid grid oscillator. The active devices are InP-based High Electron Mobility Transistors (HEMT's). A locked frequency spectrum was achieved, with a peak Effective Radiated Power (ERP) of 200 mW at 43 GHz. The grid was designed to minimize the power in the substrate modes and produce an E-field with low side-lobes.

References

[1] Y. Takimoto, "Recent activities on millimeter wave indoor LAN system development in Japan," *IEEE MTT-S Digest, Orlando,* pp. 405-408, 1995.

[2] H.H. Meinel, "Recent advances on millimeter-wave PCN system development in Europe," *IEE MTT-S Digest, Orlando,* pp. 401-404, 1995.

[3] L.Q.Bui, Y.Alon, D. Neilson, "Extended range coverage of an Imaging Radar system with Feed-Mounted 94 Ghz MIMIC Low Noise Amplifier and external ILO," *1992 IEEE MTT-S Digest,* pp. 687-690, 1992.

[4] P.F. Goldsmith, C.-T.Hsieh, G.R. Huguenin, J. Kapitzky, E.L. Moore, "Focal Plane Imaging Systems for Millimeter Wavelenghts," *IEEE Trans. Microwave Theory Tech.,* vol. 41, pp. 1664-1675, Oct. 1993.

[5] J.W. Waters, P.H. Siegel, "Applications of Millimeter and Submillimeter Thechnology to Earth's Upper Atmosphere: Results to Date and Potential for the Future," *The 4th International Symposium on Space Terahertz Technology,* Los Angeles, CA, March 1993.

[6] K. Chang, C. Sun, "Millimeter-Wave Power Combining Techniques," *IEEE Trans. Microwave Theory Tech.,* vol. 31, pp. 91-107, Feb. 1993.

[7] K.J. Russell, "Microwave Power Combining Techniques," *IEEE Trans. Microwave Theory Tech.,* vol. 27, pp. 472-478, May 1979.

[8] M. Know *et al.,* "400 W X-band GaAs MMIC CW amplifier," *IEEE MTT Symposium Digest, Orlando,* pp. 1605-1608, 1995.

[9] K. Kurokawa, "The single-cavity multiple-device oascillator," *IEEE Trans. Microwave Theory Tech.,* vol. 19, pp. 793-801, Oct. 1971.

[10] J.W. Mink, "Quasi-Optical Power Combining of Solid-State Millimeter-Wave Sources," *IEE Trans. Microwave Theory Tech.,* vol. 34, pp. 273-279, Feb. 1986.

[11] M. Kim, J.J. Rosenberg, R.P. Smith, R.M. Weikle, J.B. Hacker, M.P. De Lisio, D.B. Rutledge, "A Grid Amplifier," *IEEE Microwave Guided Wave Lett.,* vol. 1, pp. 322-324, Nov. 1991.

[12] M. Kim, E.A. Sovero, J.B. Hacker, M.P. De Lisio, J.-C. Chiao, S.-J. Li, D.R. Gagnon, J.J. Rosenberg, D.B. Rutledge, "A 100-Element HBT Grid Amplifier," *IEEE Trans. Microwave Theory Tech.*, vol. 41, pp. 1762–1771, Oct. 1993.

[13] D.B. Rutledge, A. Moussessian, M.P. De Lisio, C.-M. Liu, J.J. Rosenberg, "Modelling of Transistor Grid Amplifiers," *1994 IEEE MTT-S Int. Microwave Symp.*, Workshop Notes, WFFA: Circuit Level Design and Modelling of Quasi-Optical Circuits and Systems, pp. C.1–C.16, 1994.

[14] C.-M. Liu, E.A. Sovero, M.P. De Lisio, A. Moussessian, J.J. Rosenberg, D.B. Rutledge, "Gain and Stability Models for HBT Grid Amplifiers," *1995 IEEE AP-S Int. Symp. Dig.*, pp. 1292–1295, 1995.

[15] M.P. De Lisio, S.W. Duncan, D.-W. Tu, C.-M. Liu, A. Moussessian, J.J. Rosenberg, D.B. Rutledge, "Modelling and Performance of a 100-Element pHEMT Grid Amplifier," *IEEE Trans. Microwave Theory Tech.*, vol. 44, pp. 2136–2144, December 1996.

[16] C.-M. Liu, "Monolithic Grid Amplifiers," Ph.D. Thesis, California Institute of Technology. Pasadena, CA, 1996.

[17] C.-M. Liu, E.A. Sovero, W.J. Ho, J.A. Higgins, D.B. Rutledge, "A Millimeter-Wave Monolithic Grid Amplifier," *Int. Journal of Infrared and Millimeter Waves*, vol. 16, pp. 1901–1910, Nov. 1995.

[18] C.-M. Liu, E.A. Sovero, W.J. Ho, J.A. Higgins, M.P. De Lisio, D.B. Rutledge, "Monolithic 40-GHz 670-mW HBT Grid Amplifier," *1996 IEEE MTT-S Int. Microwave Symp.*, pp. 1123–1126, 1996.

[19] M.P. De Lisio, S.W. Duncan, D.-W. Tu, S. Weinreb, C.-M. Liu, D.B. Rutledge, "A 44-60 GHz Monolithic pHEMT Grid Amplifier," *1996 IEEE MTT-S Int. Microwave Symp.*, pp. 1127–1130, 1996.

[20] C.-Y. Chi, G.M. Rebeiz, "A Quasi-Optical Amplifier," *IEEE Microwave Guided Wave Lett.*, vol. 3, pp. 164–166, June 1993.

[21] T.P. Budka, M.W. Trippe, S. Weinreb, G.M. Rebeiz, "A 75 GHz to 110 GHz Quasi-Optical Amplifier," *IEEE Trans. Microwave Theory Tech.*, vol. 42, pp. 899–901, May 1994.

[22] N. Kolias, R.C. Compton, "A Microstrip-Based Unit Cell for Quasi-Optical Amplifier Arrays," *IEEE Microwave Guided Wave Lett.*, vol. 3, pp. 330–332, Sept. 1993.

[23] T. Mader, J. Schoenberg, L. Harmon, Z.B. Popović, "Planar MESFET Transmission Wave Amplifier," *Electronics Lett.*, vol. 29, pp. 1699–1701, Sept. 1993.

[24] H.S. Tsai, R.A. York, "Polarization-Rotating Quasi-Optical Reflection Amplifier Cell," *Electronics Lett.*, vol 29, pp. 2125–2127, Nov. 1993.

[25] N. Sheth, T. Ivanov, A. Balasubramaniyan, A. Mortazawi, "A Nine HEMT Spatial Amplifier," *1994 IEEE MTT-S Int. Microwave Symp. Dig.*, pp. 1239–1242, 1994.

[26] J.S.H. Schoenberg, S.C. Bundy, Z.B. Popović, "Two-Level Power Combining Using a Lens Amplifier," *IEEE Trans. Microwave Theory Tech.*, vol. 42, pp. 2480–2485, Dec. 1994.

[27] T. Ivanov, A. Mortazawi, "Two Stage Double Layer Microstrip Spatial Amplifiers," *1995 IEEE MTT-S Int. Microwave Symp. Dig.*, pp. 589–592, 1995.

[28] J. Schoenberg, T. Mader, B. Shaw, Z.B. Popović, "Quasi-Optical Antenna Array Amplifiers," *1995 IEEE MTT-S Int. Microwave Symp. Dig.*, pp. 605–608, 1995.

[29] J.S.H. Schoenberg, T.B. Mader, J.W. Dixon, B.L. Shaw, Z.B. Popović, "Quasi-Optical Antenna Array Amplifiers," submitted to *IEEE Trans. Microwave Theory Tech.*, March 1995.

[30] T. Ivanov, A. Balasubramaniyan, A. Mortazawi, "One- and Two-Stage Spatial Amplifiers," *IEEE Trans. Microwave Theory Tech.*, vol. 43, pp. 2138–2143, Sept. 1995.

[31] H.S. Tsai, M.J.W. Rodwell, R.A. York, "Planar Amplifier Array With Im-

proved Bandwidth Using Folded-Slots," *IEEE Microwave Guided Wave Lett.*, vol. 4, pp. 112–114, April 1994.

[32] H.S. Tsai, R.A. York, "Quasi-Optical Amplifier Array using Direct Integration of MMICs and 50 Ω Multi-Slot Antennas," *1995 IEEE MTT-S Int. Microwave Symp. Dig.*, pp. 593–596, 1995.

[33] J. Hubert, J. Schoenberg, Z.B. Popović, "High-Power Hybrid Quasi-Optical Ka-Band Amplifier Design," *1995 IEEE MTT-S Int. Microwave Symp. Dig.*, pp. 585–588, 1995.

[34] J.A. Higgins, E.A. Sovero, W.J. Ho, "44-GHz Monolithic Plane Wave Amplifiers," *IEEE Microwave Guided Wave Lett.*, vol. 5, pp. 347–348, Oct. 1995.

[35] A. Moussessian, "Quasi-Optical Active Antennas," Ph.D. Dissertation, California Institute of Technology, CA, 1997.

[36] Z.B. Popović, M. Kim, D.B. Rutledge, "Grid Oscillators," *Int. J. Infrared Millimeter Waves*, vol. 9, pp. 647–654, July 1988.

[37] Z.B. Popović, R.M. Weikle, M. Kim, D.B. Rutledge, "A 100-MESFET Planar Grid Oscillator," *IEEE Trans. Microwave Theory Tech.*, vol. 39, pp. 193–200, March 1990.

[38] R.M. Weikle, M. Kim, J.B. Hacker, M.P. De Lisio, D.B. Rutledge, "Planar MESFET Grid Oscillators Using Gate Feedback," *IEEE Trans. Microwave Theory Tech.*, vol. 40, pp. 1997–2003, Nov. 1992.

[39] J.B. Hacker, M.P. De Lisio, M. Kim, C.-M. Liu, S.-J. Li, S.W. Wedge, D.B. Rutledge, "A 10-Watt X-Band Grid Oscillator," *1994 IEEE MTT-S Int. Microwave Symp. Dig.*, pp. 823–826, 1994.

[40] P. Preventza, M. Matloubian, D.B. Rutledge, "A 43-GHz AlInAs/GaInAs/ InP HEMT Grid Oscillator," to be presented at *The IEEE MTT-S Int. Microwave Symp.*, June 1997.

[41] H. Kondo, M. Hieda, M. Nakayama, T. Tanaka, K. Osakabe, and K. Mizuno, "Millimeter and submillimeter wave quasi-optical oscillator with multi-

elements," *IEEE Trans. Microwave Theory Tech.*, vol. 40, pp. 857-863, May 1992.

[42] M.P. De Lisio, J.F. Davis, S.-J. Li, D.B. Rutledge, J.J Rosenberg, "A 16-element tunnel diode grid oscillator," *1995 IEEE AP-S Int. Symp. Dig.*, Newport Beach, CA, pp. 1284-1287, 1995.

[43] S.C Bundy, T.B. Mader, Z.B. Popović, "Quasi-Optical VCO's," *IEEE Trans. Microwave Theory Tech.*, vol. 41, pp. 1775-1781, Oct. 1993.

[44] A.C. Oak and R.M Weikle II, "A Varactor tuned 16-element MESFET grid oscillator," *1995 IEEE AP-S Int. Symp. Dig.*, Newport Beach, CA, pp. 1296-1299, 1995.

[45] W.A. Shiroma, B.L. Shaw, Z.B. Popović, "A 100-transistor quadruple grid oscillator," *IEEE Microwave Guided Wave Lett.*, vol. 4, pp. 350-351, Oct. 1994.

[46] J.B. Hacker, R.M. Weikle, M. Kim, M.P. De Lisio, D.B. Rutledge, "A 100-Element Planar Schottky Diode Grid Mixer," *IEEE Trans. Microwave Theory Tech.*, vol. 40, pp. 557–562, March 1992.

[47] H.-X.L. Liu, L.B. Sjogren, C.W. Domier, N.C. Luhmann, Jr., D.L. Sivco, A.Y. Cho, "Monolithic Quasi-Optical Frequency Tripler Array with 5-W Output Power at 99 GHz," *IEEE Electron Device Lett.*, vol. 14, pp. 329–331, July 1993.

[48] J.-C. Chiao, A. Markelz, Y. Li, J. Hacker, T. Crowe, J. Allen, D.B. Rutledge, "Terahertz Grid Frequency Doublers," presented at *The 6th Int. Symp. Space Terahertz Tech.*, March 1995.

[49] A. Moussessian, M.C. Wanke, Y. Li, J.-C. Chiao, F.A. Hegmann, S.A. Allen, T.W. Crowe, D.B. Rutledge, "A Terahertz Grid Frequency Doubler," to be presented at *The IEEE MTT-S Int. Microwave Symp.*, June 1997.

[50] W.W. Lam, H.Z. Chen, K.S. Stolt, C.F. Jou, N.C. Luhmann Jr., D.B. Rutledge, "Millimeter-Wave Diode Grid Phase Shifters," *IEEE Trans. Microwave*

Theory Tech., vol. 36, pp. 902–907, May 1988.

[51] L.B. Sjogren, H.-X.L. Liu, X.-H. Qin, C.W. Domier, N.C. Luhmann Jr., "Phased Array Operation of a Diode Grid Impedance Surface," *IEEE Trans. Microwave Theory Tech.*, vol. 42, pp. 565–572, April 1994.

[52] R.M. Weikle, "Quasi-optical planar grids for Microwave and Millimeter-wave Power Combining," Ph.D. Thesis, California Institute of Technology, Pasadena, CA, 1992.

[53] M.P. De Lisio, "Hybrid and Monolithic Active Quasi-Optical Grids," Ph.D. Thesis, California Institute of Technology, Pasadena, CA, 1996.

[54] S.C. Bundy, Z.B. Popović, "A generalized analysis for grid oscillator design," *IEEE Trans. Microwave Theory Tech.*, vol. 42, pp. 2486-2491, Dec. 1994.

[55] S.C. Bundy, "Analysis and Design of Grid Oscillators," Ph.D. Thesis, University of Colorado, Boulder, CO, 1994.

[56] H.-S. Tsai, R.A. York, "FDTD analysis of folded-slot and multiple slot antennas on thin substrates," *IEEE Trans. Antennas Prop.,* vol. AP-44, pp. 217-226, Feb. 1996.

[57] A. Alexanian, N.J. Kolias, R.C. Compton, R.A. York, "FDTD analysis of quasi-optical arrays using cyclic boundary conditions and Berenger's PML," *IEEE Microwave Guided Wave Lett.*, vol. 6, pp. 138, March 1996.

[58] J.-P. Berenger, "A perfectly matched layer for the absorption of electromagnetic waves," *J.Comput. Phys.*, 114, pp. 185-200, 1994.

[59] N.J. Kolias, R.C. Compton, "A microstrip based quasi-optical polarization rotator array," *IEEE MTT-Symposium digest (Orlando)*, pp. 773-776, June 1995.

[60] B. Toland, J. Lin, B. Houshmand, T. Itoh, "FDTD analysis of an active antenna," *IEEE Microwave Guided wave Lett.*, vol. 3, pp. 423-425, Nov. 1993.

[61] V.A. Thomas *et al.,* "FDTD analysis of an active antenna," *IEEE Microwave Guided Wave Lett.*, vol. 4, pp. 296-298, Sept. 1994.

[62] W. Lam, C. Jou, H. Chen, K. Stolt, N. Luhmann, D.B. Rutledge, "Millimeter-Wave Diode-Grid Phase-Shifters," *IEEE Trans. Microwave Theory and Tech.*, pp. 902-907, no. 5, May 1988.

[63] L.B. Sjogren, H.L. Liu, X.H. Qin, C.W. Domier, N.C. Luhmann, "Phased Array Operation of a Diode Grid Impedance Surface," *IEEE Trans. Microwave Theory Tech.*, vol. 42, pp. 565-572, April 1994.

[64] W.W. Lam, "Millimeter-Wave Monolithic Schottky Diode-Grid Phase-Shifters," Ph.D. Dissertation, California Institute of Technology, 1987.

[65] Lance B. Sjogren, "A Multi-Function Millimeter-Wave Schottky Diode Array Electronic Beam Controller," Ph.D. Dissertation, University of California, Los Angeles, 1992.

[66] X.H. Qin, W.M. Zhang, C.W. Domier, N.C. Luhmann, W. Berk, S. Duncan, D.W. Tu, "Monolithic millimeter-Wave Beam Control Array," *Digest of IEEE Microwave Theory and Techn. Symp.*, MTT-S95, WE3F-F4, pp. 1669-1672, 1995.

[67] J.-C. Chiao, "Quasi-Optical Components for Millimeter and Submillimeter Waves," Ph.D. Dissertation, California Institute of Technology, 1996.

[68] J.-C. Chiao, D.B. Rutledge, "Microswitch Beam-Steering Grid," *Int. Conference on Millimeter and Submillimeter Waves and Applications*, S.Diego, CA, Jan. 1994.

[69] J.Jason Yao, M.Frank Chang "A surface micromachined miniature switch for telecommunications applications with signal frequencies from DC up to 4 GHz," *The 8th International Conference on Solid-State Sensors and Actuators, Stockholm, Sweden*, pp. 384–387, 1995.

[70] E.A. Sovero, J.B. Hacker, J.A. Higgins, D.S. Deakin, A.L. Sailer "A Ka-Band Monolithic Quasi-Optic Amplifier," *1998 IEEE MTT-S Digest*, pp. 1453–1456, 1998.

[71] J. Hubert, L. Mirth, S. Ortiz, A. Mortazawi "A 4-Watt Ka-Band Quasi-

Optical Amplifier," *to be presented at the 1999 IEEE MTT-S, Anaheim, CA* June, 1999.

Chapter 2

Modeling of Quasi-Optical Arrays

In this chapter, two models for analyzing quasi-optical grid amplifiers based on a finite-element simulator are presented. The models are deduced from the High Frequency Structure Simulation (HFSS) of the whole unit cell. In the first model simulations of single elements of the structure are carried out that result in a lumped-element equivalent circuit. The second model finds the full scattering parameters in an approach that is similar to the calibration of a vector network analyzer. The new two models include mutual coupling effects and are an extension of the unit-cell transmission-line model developed by De Lisio *et al.* By using these models, the gain of a 10×10 hybrid X-band grid amplifier has been accurately predicted. To further test the validity of the model three passive structures with different loads have been fabricated and tested using a new focused-beam network analyzer that we developed.

2.1. INTRODUCTION

Two techniques have been reported for the modeling of quasi-optical systems. The first technique assumes an infinite array, allowing the grid to be reduced to a single unit cell with electric and magnetic walls as symmetry planes [1-4]. The unit cell of an amplifier grid is shown in Fig. 2.1. The cell is 7.3 mm on a side. The input beam is coupled to the gates of the transistor through the horizontal input leads, which also supply the gate bias. The output beam
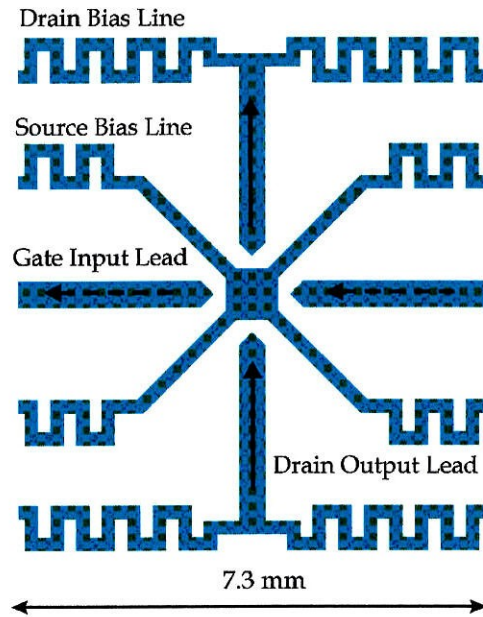
Fig. 2.1. Unit cell of a 100-element, X-band grid amplifier. The arrows indicate the direction of rf currents.
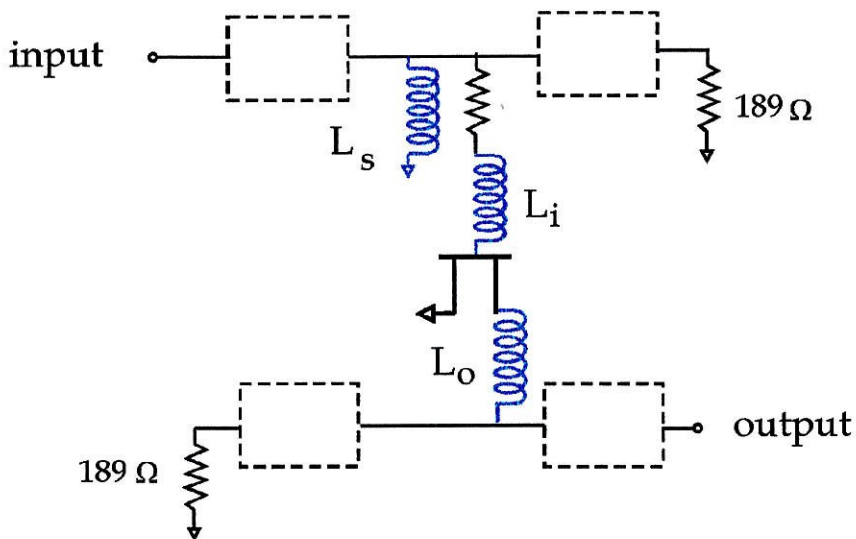
Fig. 2.2. The half-cell transmission-line equivalent circuit model for the grid amplifier.
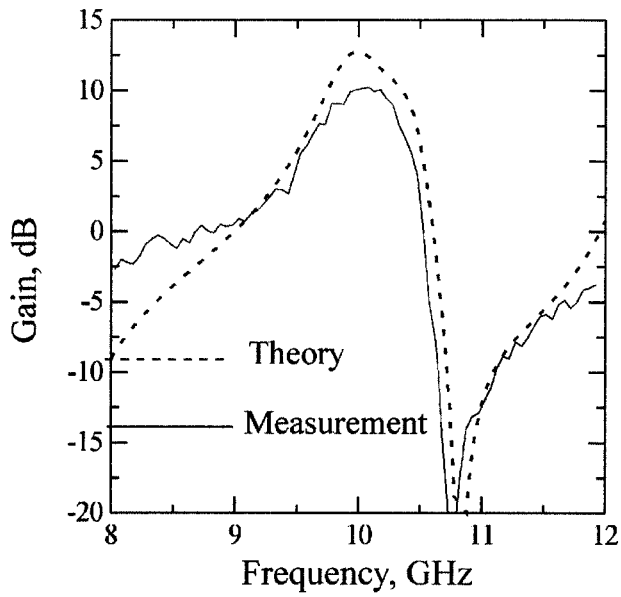
Fig. 2.3. Grid amplifier gain versus frequency. The grid is tuned for peak gain at 9 GHz.
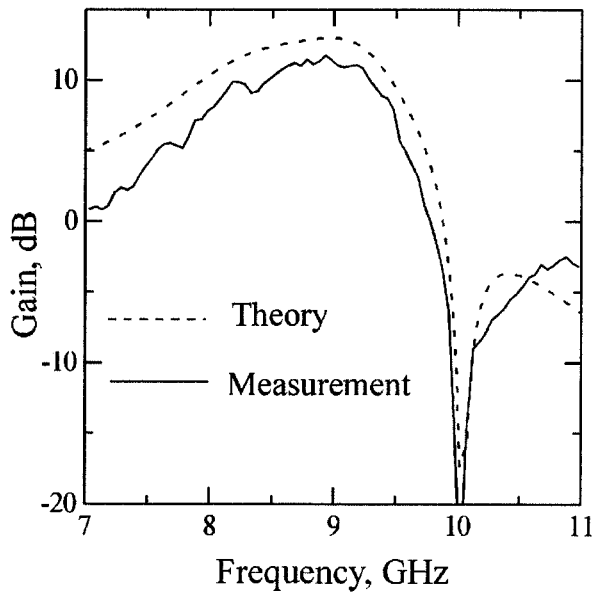
Fig. 2.4. Grid amplifier gain versus frequency. The grid is tuned for peak gain at 10 GHz.

is radiated from the vertical drain leads. Both input and output leads are 0.4-mm wide. Bias to the drain and the source is provided by the thin meandering lines, which are 0.2-mm wide. DeLisio *et al.* [1] developed a transmission-line equivalent circuit for this unit cell that is shown in Fig. 2.2. Inductors L_i and L_o represent coupling through the input and output leads, and L_s represents the inductance of the bias lines. Numerical values for L_i and L_o are computed by using the method of moments to estimate the surface current distribution on the metal strips and then the driving-point impedance is calculated using the induced emf technique, developed by Weikle at Caltech [5,6]. The numerical value for the shunt bias-line inductance, L_s, is empirically determined. This model neglects the mutual coupling between the lines. Fig. 2.3 and Fig. 2.4 show the measured and the modelled gain of the amplifier when it is tuned for 9 GHz and 10 GHz. The model used overpredicts the gain by 3 dB.
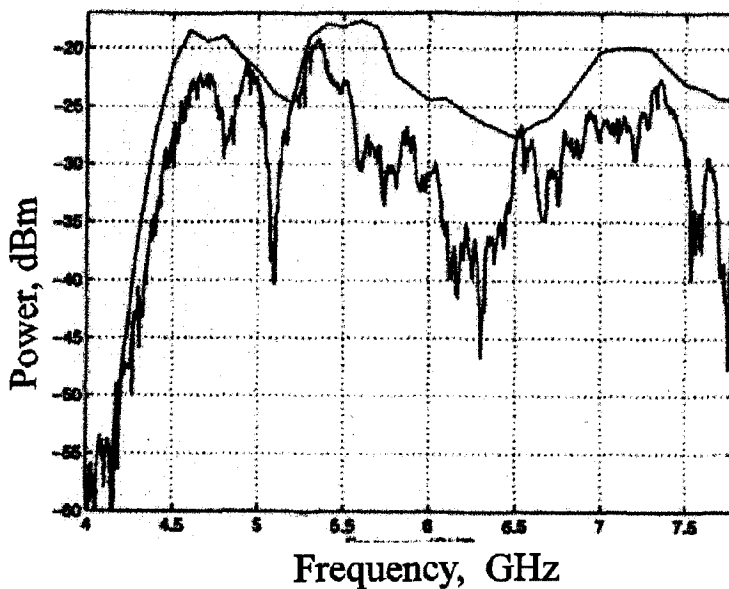
Fig. 2.5. Output for a 2×2 grid amplifier system, measurement and simulation [7].

The second technique [7,8], is developed by M.B. Steer at North Carolina State University. The model uses the method of moments to simulate the full grid. The analysis incorporates surface modes, and includes the edge effects of the array. This technique is used to model the nonlinear performance of a 2×2 quasi-optical grid amplifier system and compromises were made in the complexity of the system. The 2×2 grid amplifier has a simple metal pattern, so presumably the model may not be accurate for more complicated metal shapes. Fig. 2.5 shows the comparison between the simulation results and measurements. This model also overpredicts the gain by as much as 3 dB.

Advancement in finite-element analysis techniques, such as Ansoft's High Frequency Structure Simulator (HFSS) [9], allows an accurate and fast solution for the electromagnetic modeling of arbitrarily-shaped, passive, three-dimensional structures. In this chapter, two new models that are an extention of the unit-cell transmission-line model and include mutual coupling effects are developed based on HFSS simulations. It is also shown that the new models agree very well with previously published measurements [1], even though substrate modes and edge effects are not included. The unit-cell approximation was used extensively to model the performance of both amplifiers and oscillators. Substrate mode propagation was not significant for the grid amplifiers. However, for certain phase distributions among the active devices of an oscillator grid, substrate modes may be strongly excited as shown in chapter 5. To further validate the new models [10], a comparison between measurements of passive arrays and simulations is presented.

2.2. MODELING OF THE UNIT CELL

2.2.1. LUMPED-ELEMENT EQUIVALENT CIRCUIT

The first model developed accounts for the coupling between the gate lead

and the meandering bias lines. In order to find the coupling coefficient, M, three simulations are performed. The first simulation finds the inductance of the horizontal lead, L_g. Fig. 2.6a shows the gate lead of the half-cell on a 15-mil Duroid substrate ($\varepsilon_r = 2.2$), as it is exactly simulated in HFSS. The planar structure is bounded by the E and H-walls of the waveguide. The excitation appears at port 1. The equivalent circuit is shown in Fig. 2.6b and it perfectly matches the HFSS as seen in Fig. 2.7. The second simulation finds the impedance of the meandering line, L_b. The planar structure, the equivalent circuit and the agreement between them are presented in Fig. 2.8 and 2.9.
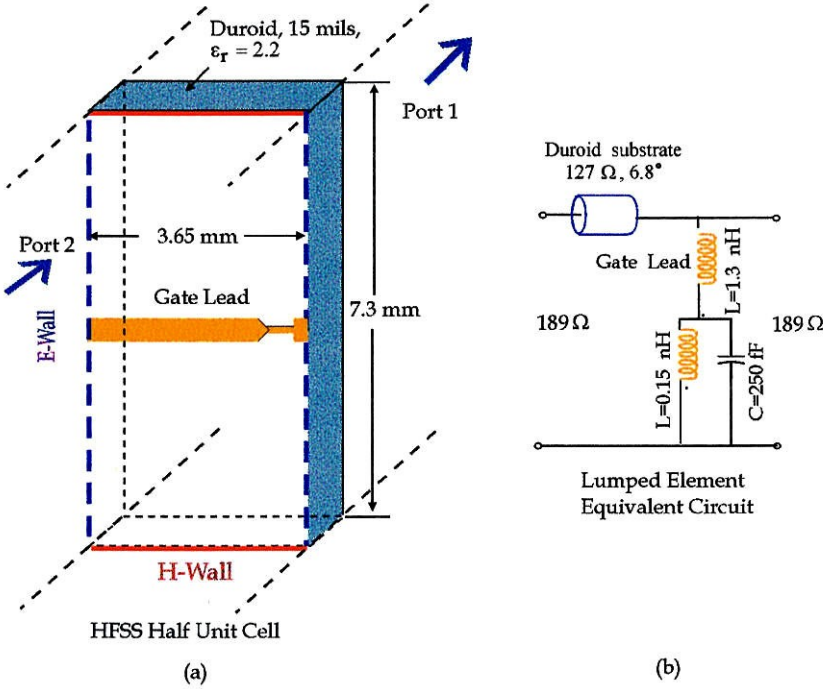
Fig. 2.6. (a) Waveguide representation of half-cell as simulated in HFSS and (b) the equivalent lumped-element circuit.
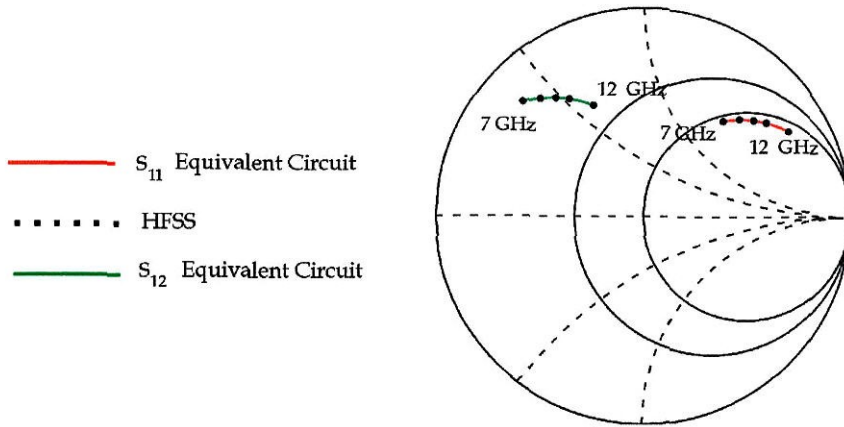
Fig. 2.7. *S*-parameters of the structure in Fig. 2.6 calculated from the equivalent lumped-element circuit and in HFSS.
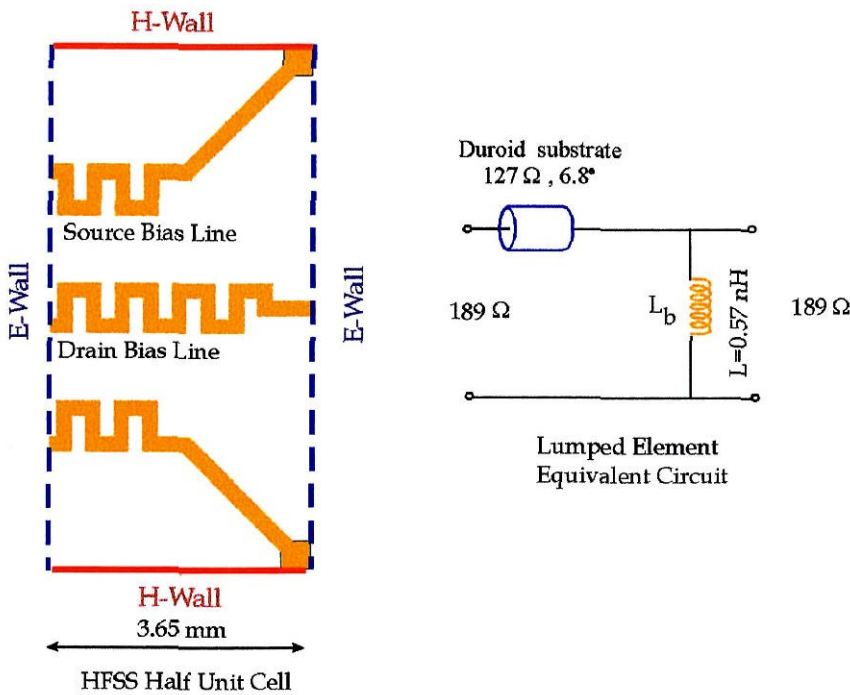
Fig. 2.8. Half-cell with only the meandering line of the input circuit. Magnetic walls are imposed on top and bottom and electric walls are imposed on the sides.
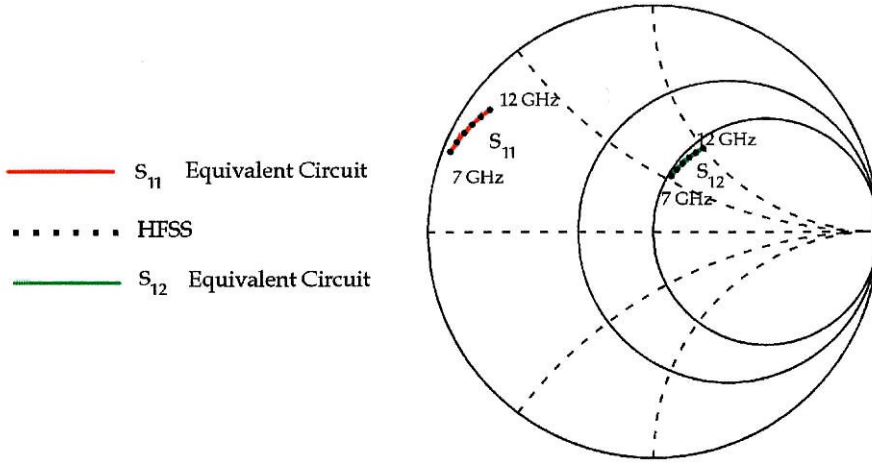
Fig. 2.9. S-parameters of the structure in Fig. 2.8: HFSS versus lumped-element model.
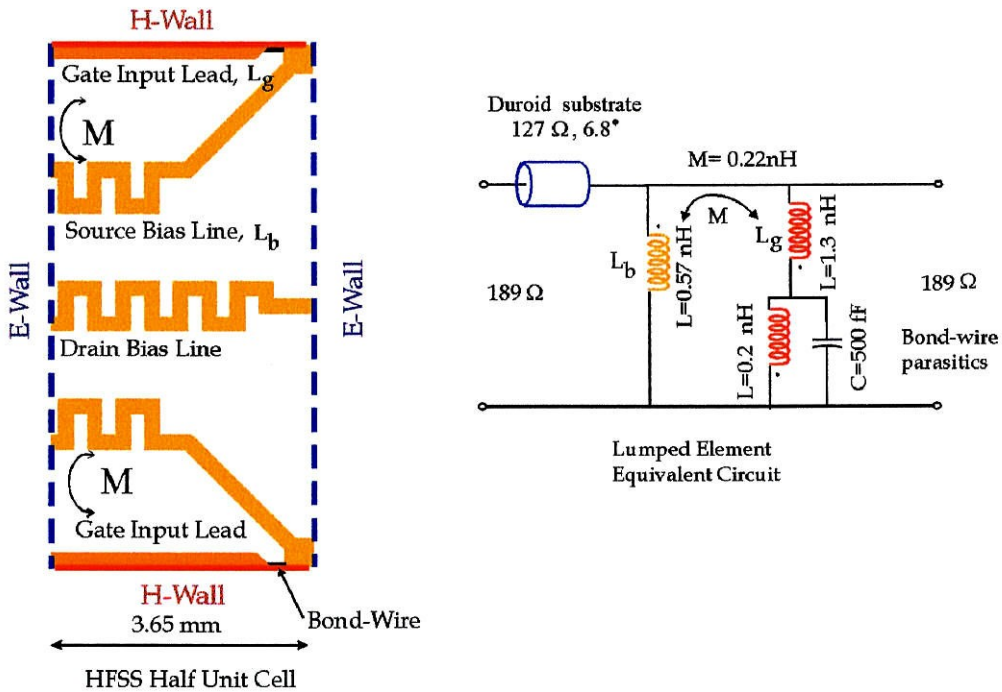
Fig. 2.10. Half unit cell for the input circuit. There is mutual coupling between the gate input lead and the meandering bias lines. The bond-wire that is also simulated in HFSS is equivalent to a parallel LC combination shown in the lumped element equivalent circuit on the right.
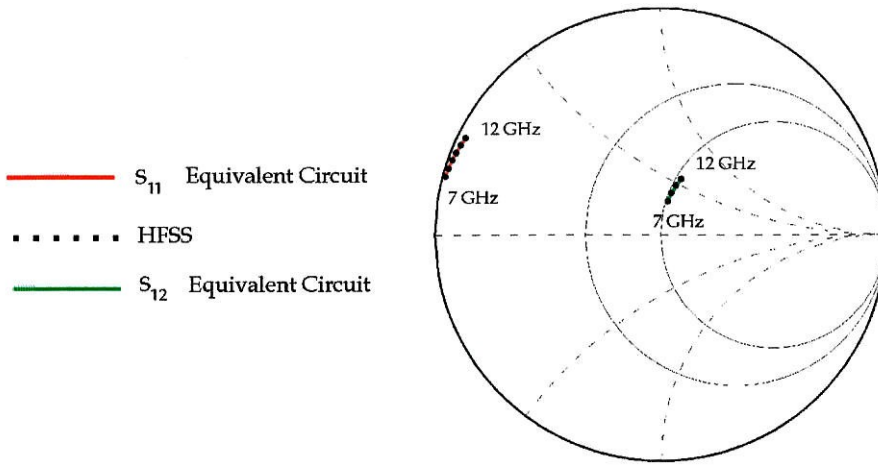
Fig. 2.11. S-parameters for the structure in Fig.2.10: HFSS versus lumped-element model.
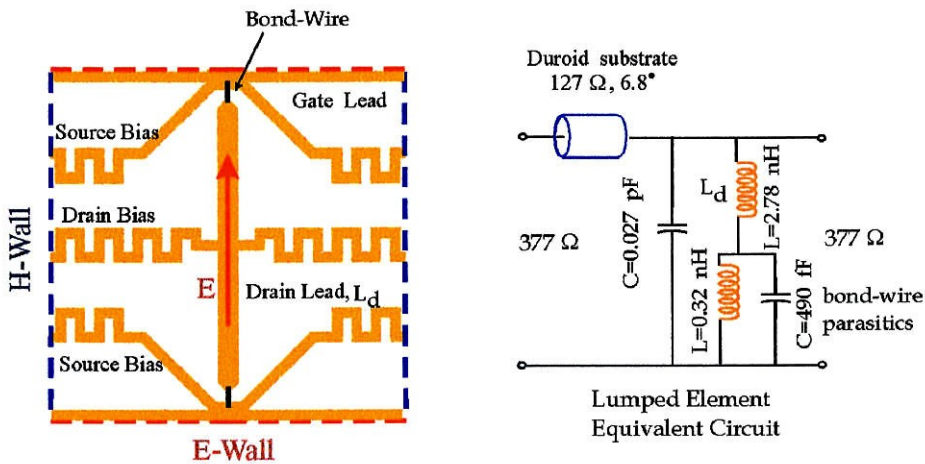
Fig. 2.12. HFSS and lumped element equivalent circuit for the output circuit of the grid amplifier. The electric field is vertically polarized.
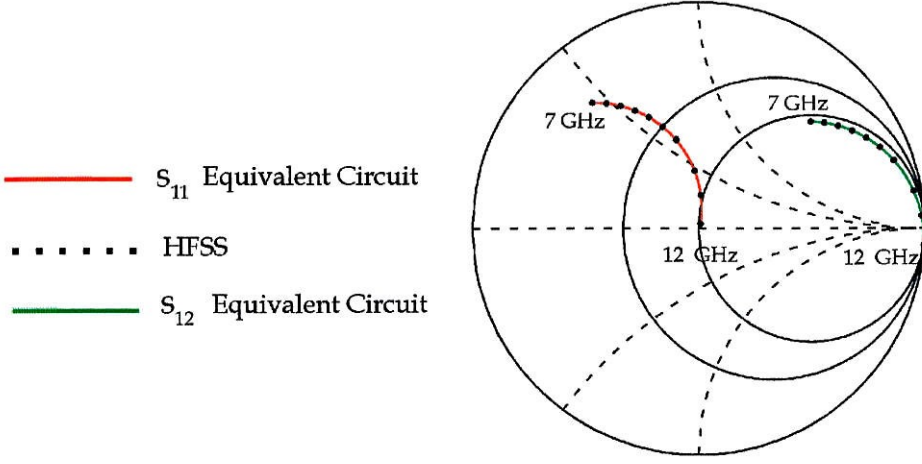
Fig. 2.13. *S*-parameters for the structure in Fig. 2.12: HFSS versus lumped-element equivalent circuit.

The last simulation finds the combined impedance of both the gate and bias lines, L_{tot}. The coupling coefficient, M, is determined by the following equation:

$$L_{tot} = \frac{L_b L_g - M^2}{L_b + L_g + 2M}. \tag{2.1}$$

The last step is to change the polarization and to find the equivalent circuit for the vertical output leads. For a vertically polarized electric field, the unit cell is shown in Fig. 2.12. The equivalent circuit is represented by an inductance, L_d, in series with the LC combination that simulates the bond-wire effect. Capacitive coupling, $C = 0.027\,\mathrm{pF}$, between the gate and the meandering lines is also taken into account.

The simulations of the input and output circuits of the amplifier result in the assembly presented in Fig. 2.14. This lumped-element equivalent circuit deduced from HFSS accounts for the coupling between the gate lead and the bias lines. Other parasitic elements such as the inductance of the bond wires and the finite conductivity of the metal are also included in the simulations.
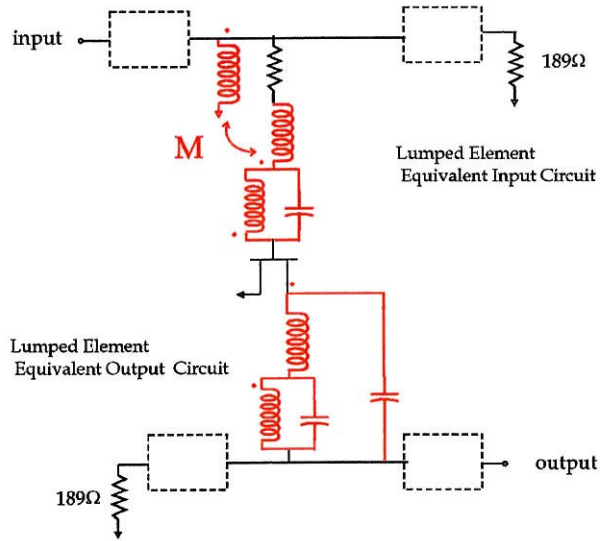
Fig. 2.14. The half-cell lumped-element equivalent circuit model for the grid amplifier.
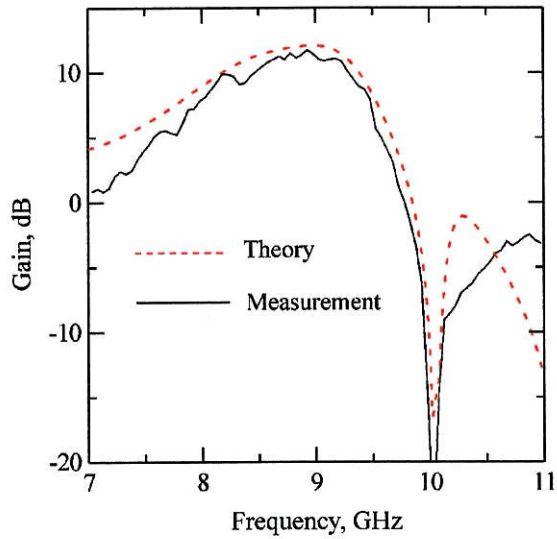
Fig. 2.15. Grid amplifier gain versus frequency. The grid is tuned for peak gain at 9 GHz.
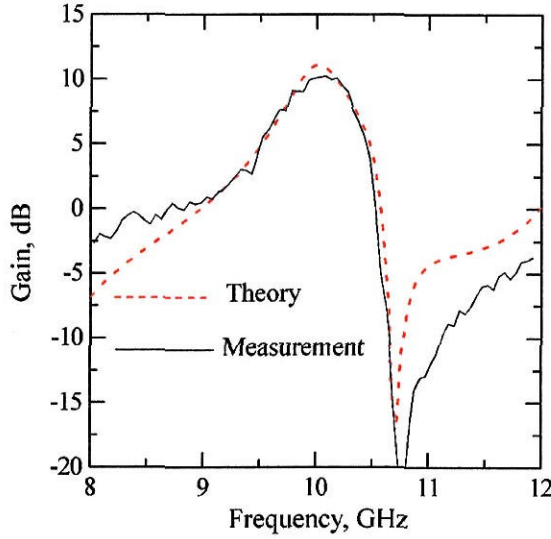
**Fig. 2.16.** Grid amplifier gain versus frequency. The grid amplifier is tuned for peak gain at 10 GHZ.

Fig. 2.15 and 2.16 show the measured and modelled gain of the amplifier tuned at $10\,\text{GHz}$ and $9\,\text{GHz}$ respectively. The model predicts a gain that is only $0.5\,\text{dB}$ higher than measured.

2.2.2. The scattering-parameter model

Fig. 2.17 shows a three-port grid half-cell. Such a structure can be modelled using a three-port s-parameter matrix. Ports 1 and 2 are the front and back of the grid respectively, and port 3 is the internal port on the grid cell where the device will be attached. The internal port is exposed at the edge of the grid where well-defined loads can be connected. The three-port structure can be solved directly for the s-parameters. Reciprocity can be applied so that $s_{12} = s_{21}$, $s_{13} = s_{31}$, and $s_{23} = s_{32}$ and the s-parameter matrix of the grid is simplified
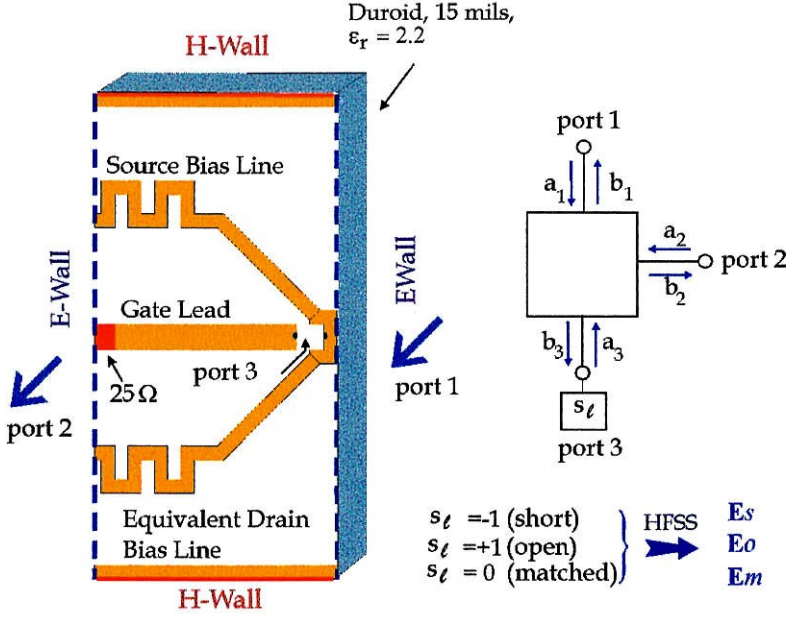
Fig. 2.17. Three-port half-cell. A short, an open and a 75Ω load are attached at the third port.

to the following matrix:

$$
s = \begin{pmatrix} s_{11} & s_{12} & s_{13} \\ s_{12} & s_{22} & s_{23} \\ s_{13} & s_{23} & s_{33} \end{pmatrix} \tag{2.2}
$$

We can now apply a technique that is analogous to the calibration of a network analyzer. This method directly utilizes data obtained from HFSS two-port simulations. Three different loads are placed across the internal port. This reduces the strucutre to a two-port. Typically the loads are a short circuit, an open circuit, and a matched load. Simulations of the structure are carried out for each of the three loads placed at the active device location. These three two-port s-parameter files, $\tilde{e}_m$, $\tilde{e}_s$, $\tilde{e}o$, correspond to the matched termination, short-circuit, and open-circuit, respectively. These calibration s-parameters can

then be used to find the two-port s-parameters of the grid using

$$s = \begin{pmatrix} e_{11m} & e_{12m} & s_{13} \\ e_{21m} & e_{22m} & s_{23} \\ s_{31} & s_{32} & s_{33} \end{pmatrix} \qquad (2.3)$$

where

$$s_{33} = \frac{e_{21s} + e_{21o} - 2e_{21m}}{e_{21o} - e_{21s}} \qquad (2.4)$$

$$s_{13} = s_{31} = \sqrt{(e_{11m} - e_{11s})(1 + s_{33})} \qquad (2.5)$$

$$s_{23} = s_{32} = \sqrt{(e_{22m} - e_{22s})(1 + s_{33})} \qquad (2.6)$$

This procedure is done twice, once for each polarization. The resulting pair of s-matrices is incorporated into the overall amplifier model as shown in Fig. 2.18. Fig. 2.19 shows the comparison between the measured amplifier gain tuned for peak gain at 10 tsGHz with the gain predicted with the scattering-parameter model. The agreement is very good.
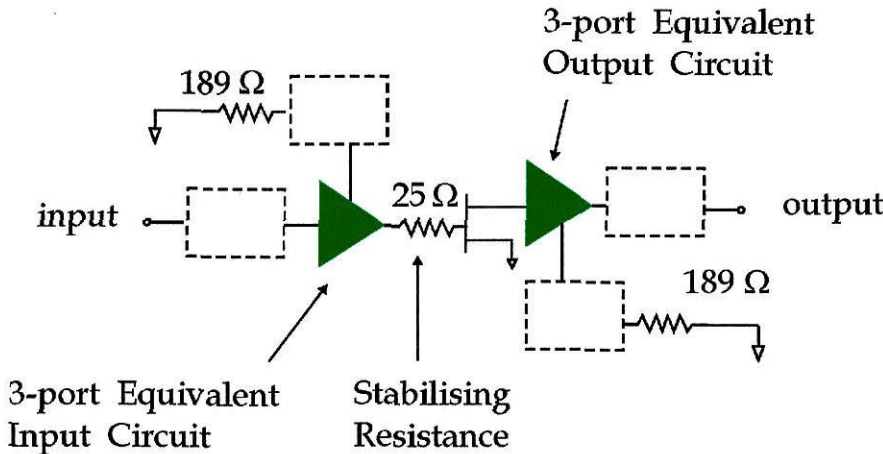
Fig. 2.18. The scattering parameter assembly for the grid amplifier.
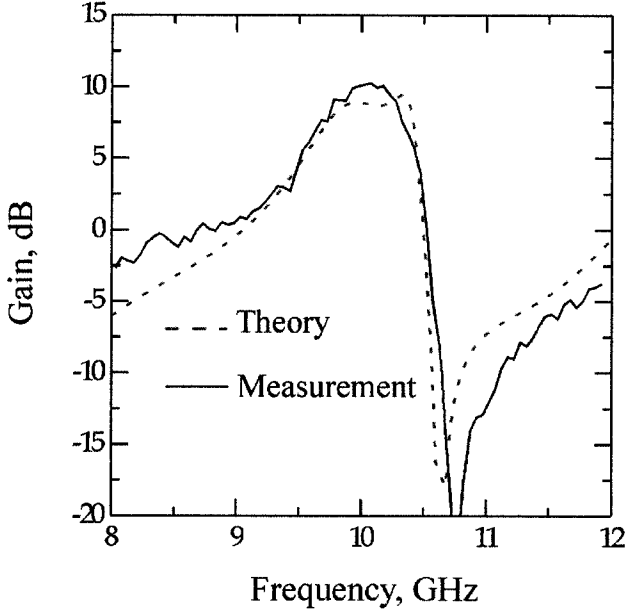
Fig. 2.19. Grid amplifier gain versus frequency. The grid amplifier is tuned for peak gain at 10 GHZ.

2.3. PASSIVE STRUCTURES

To validate the use of the HFSS in the design of the grid amplifiers, three 23×23-element passive structures with short circuits, open circuits and 75Ω terminations have been modelled and tested [9]. Fig. 2.20 shows the passive grid layout. The configuration is very similar to the topology of a grid amplifier. The unit cell is 2 mm on a side, and it is a less complicated version of the cell analyzed in section 2.2.1 and 2.2.2. The horizontal and vertical leads that correspond to the gate and drain leads are 200 μm wide. For simplicity the bias lines are thin straight lines instead of the meandering-shape and are 10 μm wide.

35
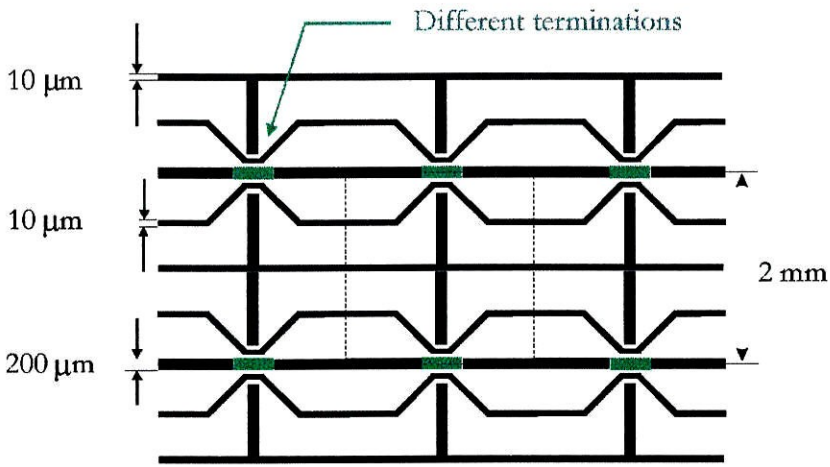
Fig. 2.20. Passive array. The black lines are metal and the green area is the location of the devices and the various terminations.
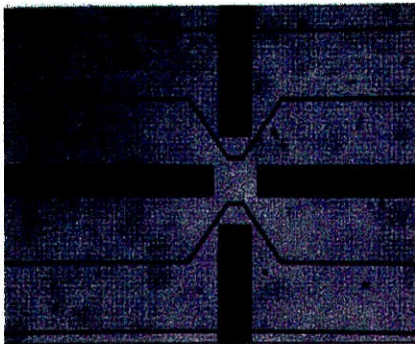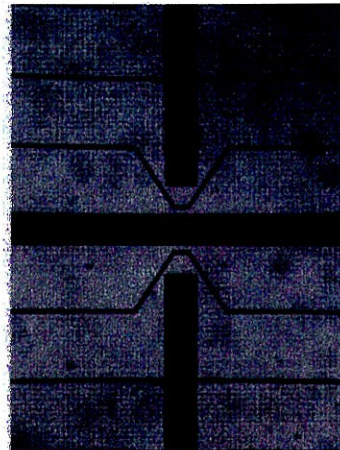
(a)   (b)

Fig. 2.21. Photograph of the passive structures: Open circuit array (a), short circuit array (b).

The arrays were fabricated by Rockwell International Science Center. The substrate used is a 0.635-mm thick, 75-mm diameter GaAs wafer. Based on the modelling discussions from the previous section, three simulations are performed for each passive grid and lumped-element equivalent circuits are constructed. Fig. 2.22 shows the half-unit cell for the circuit with the short termination at the third port, and Fig. 2.23 shows the s-parameters for this structure. The coupling coefficient, M, between the horizontal lines is $M = 125$ pH.
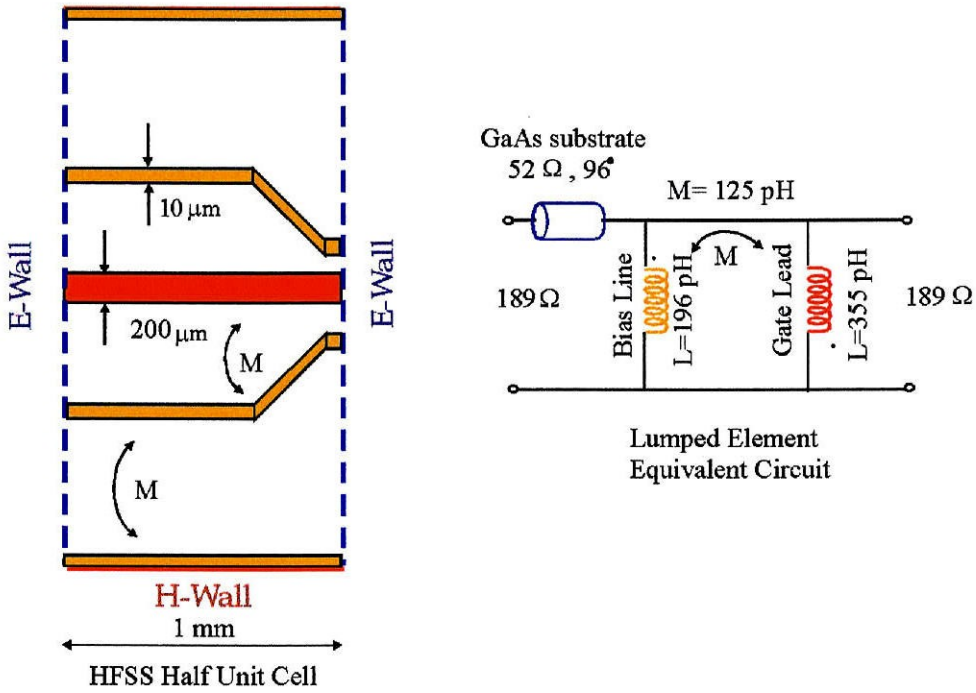
Fig. 2.22. Half-cell for the passive structure with the short termination and its equivalent circuit.
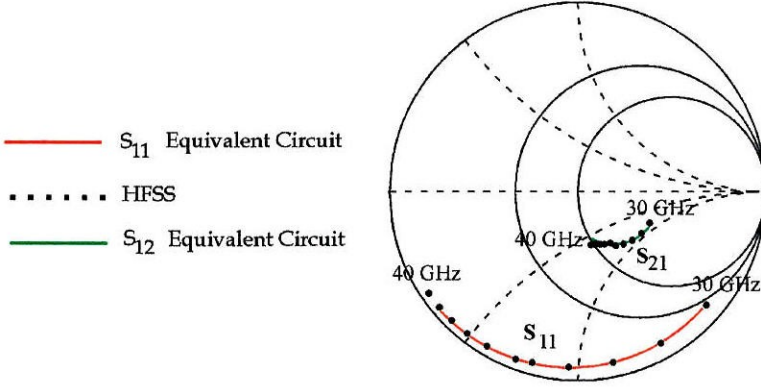
Fig. 2.23. *S*-parameters for the structure in Fig. 2.22: HFSS versus lumped-element model.

Fig. 2.24 shows the half unit cell with the open termination at the third port This load corresponds to a capacitor, $C = 113\,\text{fF}$, in series with the equivalent inductance, $M = 226\,\text{pH}$, of the horizontal lines. HFSS simulation takes into account the finite conductivity of the gold, $\sigma_{Au} = 3\times10^7\,\text{S/m}$. The effect of the finite conductivity is to reduce the magnitude of the *s*-parameters. Fig. 2.25 shows the scattering parameters for the structure with the open terminations when the finite conductivity is taken into account (b), and when it is not (a). In the third structure, a $75\,\Omega$-resistance is attached at the third port. For horizontally polarized beam the equivalent circuit is just a series combination of a resistor with the equivalent inductance of the horizontal lines. Fig. 2.26 shows the passive array and Fig. 2.27 shows the *s*-parameters of the cell. In all three cases the scattering parameters obtained from HFSS and the *s*-parameters deduced from the lumped-element equivalent circuits are in excellent aggreement.
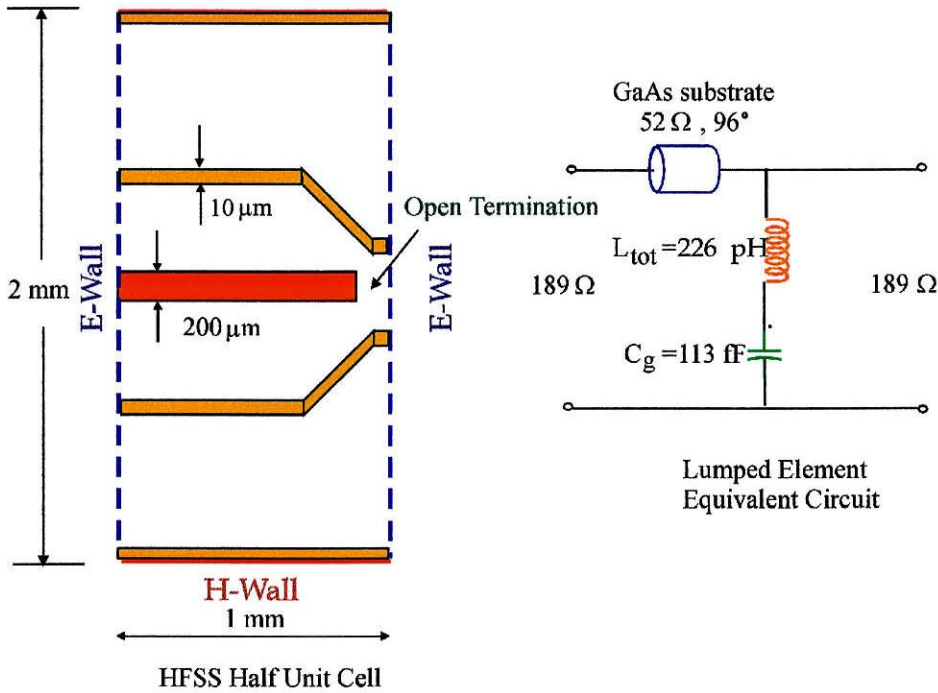
Fig. 2.24. Half-cell for the passive structure with the open termination and its equivalent circuit.
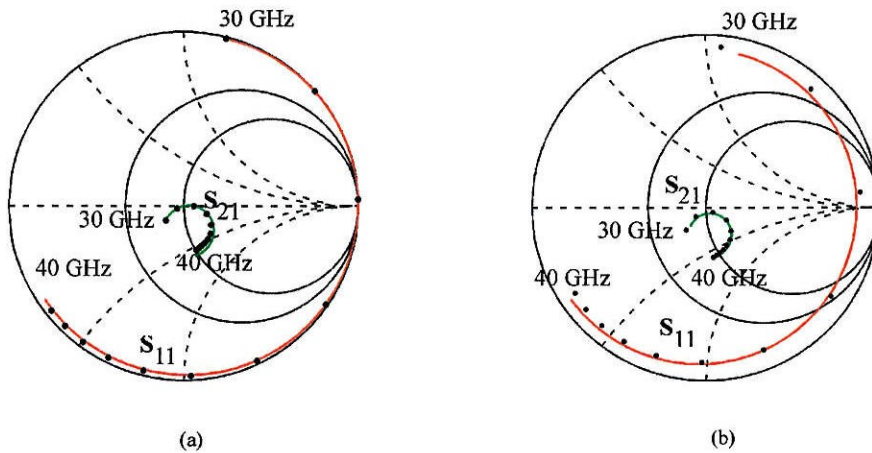
Fig. 2.25. *S*-parameters for the structure in Fig. 2.24: HFSS versus lumped-element model.
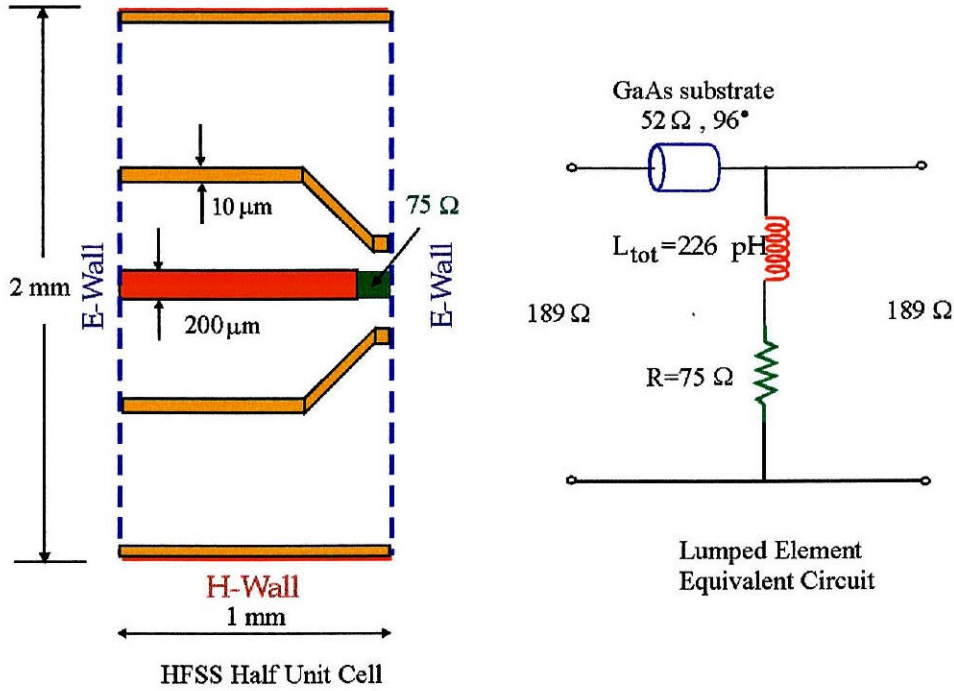
Fig. 2.26. Half-cell for the passive structure with the 75Ω termination and its equivalent circuit.
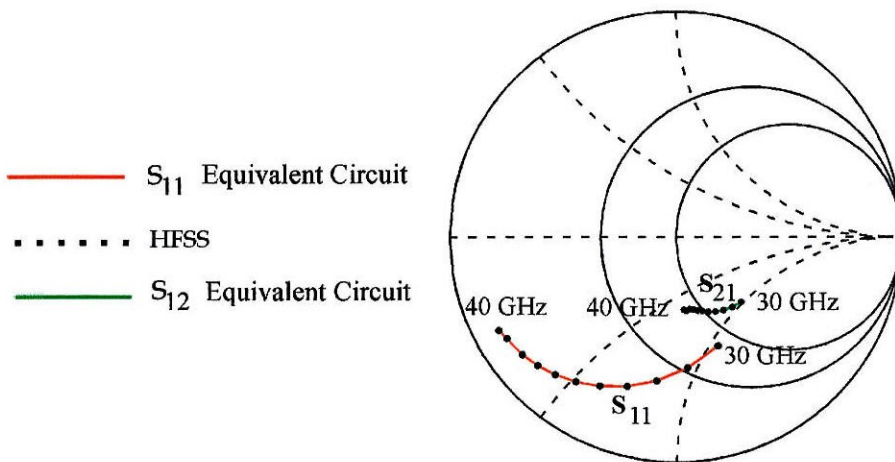
Fig. 2.27. *S*-parameters for the structure in Fig. 2.26: HFSS versus lumped-element model.

2.4. Focused Gaussian Beam Set-Up

2.4.1. Measurement System

The quasi-optical measurement set-up shown in Fig. 2.28 is an extention of the lens-focused reflectometer developd by Gagnon [11] to a full two-port system. Ghodgaonkar and Varadan [12-14] used a similar technique and succesfully characterized complex permittivities and permeabilities of materials.
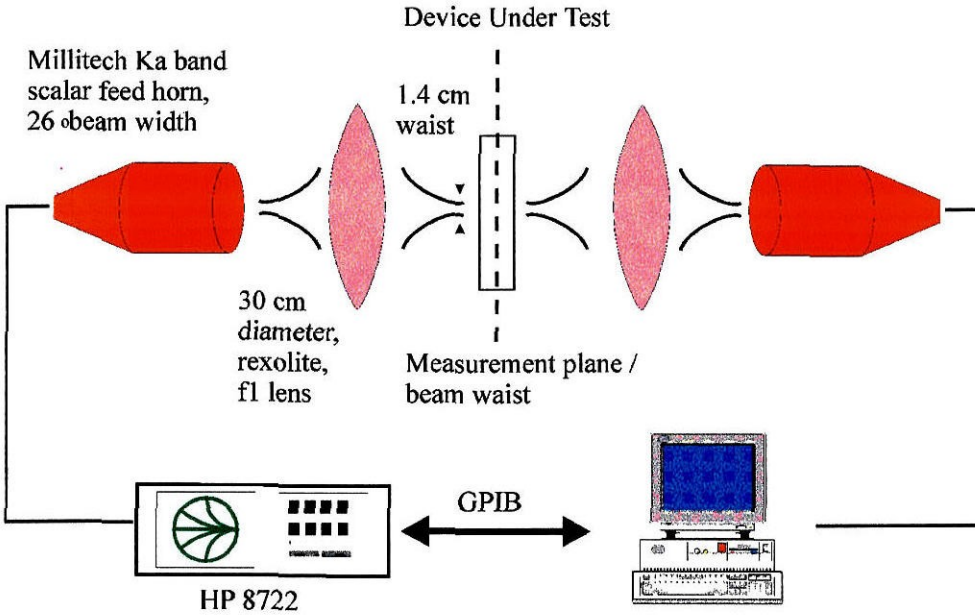
Fig. 2.28. Gaussian-beam measurement set-up.

The technique described in this chapter uses two bi-convex rexolite lenses. The ratio of focal distance, F to diameter of the lens, D (F/D) is equal to one and D is approximately 30 cm. Two Millitech SFH scalar corrugated horn antennas driven by an HP8722D vector network analyzer are used to transmit and receive the gaussian beam. The field distribution of these scalar feed horns is independent of the angle and their radiation pattern is azimuthally symmetric, making them

ideal devices for illuminating symmetric structures. The network analyzer is used to make both magnitude and phase measurements of *s*-parameters of the samples in free-space. A computer is used to facilitate the calibration routine and store the calibration data. The two lenses along with the transmit and receive horns have been mounted on a carriage and the distance between them can be changed with an accuracy of 1 mil. The system can be used over the entire bandwidth (28.5-40 GHz).

A photograph of the system is shown in Fig. 2.29.
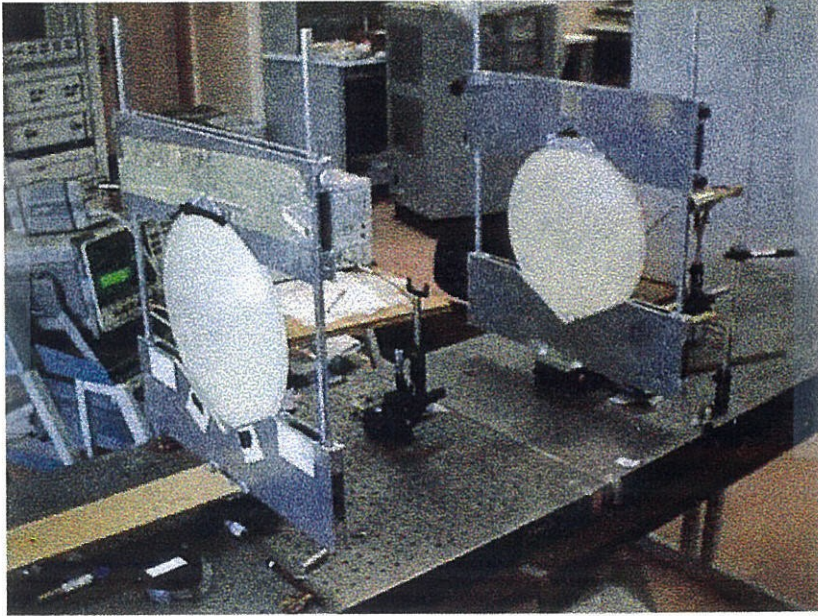
Fig. 2.29. Photograph of measurement set-up.

The two lenses focus the gaussian beam down to a beam-waist. The measurements were performed in the beam-waist location, at the focal distance, where the gaussian beam has a plane wavefront and a minimum beam radius (w_o) as shown in Fig. 2.30. The constant phase front allows the incident beam to be treated like a TEM wave propagating in the z-direction.
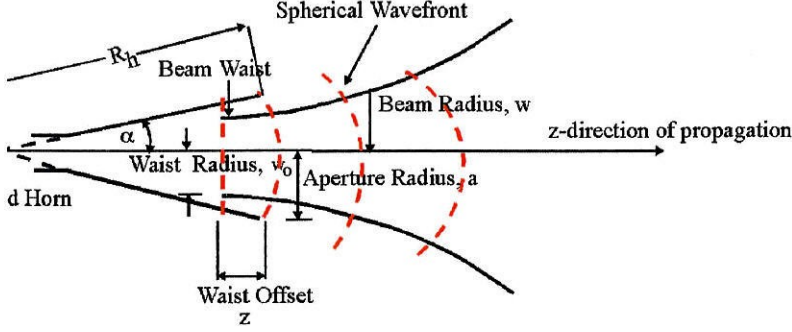
Fig. 2.30. Gaussian beam.

As the beam propagates the plane wave becomes spherical with radius R. To determine the beam-waist radius and location we use the following formulas [15]:

$$w_o = \frac{w}{\sqrt{1 + (\frac{\pi w^2}{\lambda R})^2}} \qquad (2.7)$$

$$z = \frac{R}{1 + (\frac{\lambda R}{\pi w^2})^2} \qquad (2.8)$$

where $w = 0.644a$, $\alpha = 7.5°$ and $R = R_h$ as shown in Fig. 2.30. In our case the beam radius is $w_o = 14\,mm$ and $z = 30.5$ cm. A detailed discription of the gaussian beam propagation can be found in [16].

2.6.2 CALIBRATION PROCEDURES

Clearly the first step is to calibrate the measurement system in free-space. For the reflection measurements the calibration was implemented with three standards, namely a short (a large sheet of aluminum at the measurement plane), an offset short and a match (a large section of absorber at some distance from the measurement plane).
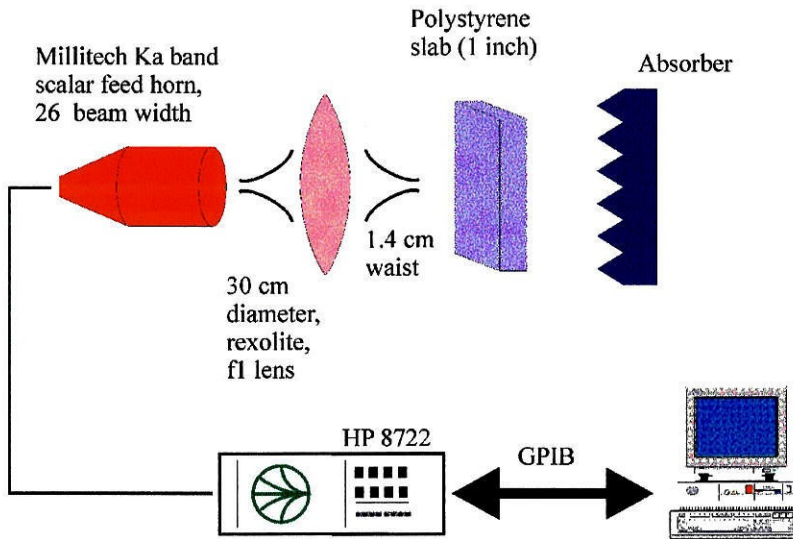
Fig. 2.31. Set-up for the reflection measurements of the polysterene slab.

The software for this calibration technique is written by Blythe Dickman at Caltech. For the transmission measurements only a thru calibration is required. The through standard is realized by keeping the distance between the two antennas equal to twice the focal distance. To check the calibration, measurements were made on a polysterene slab, by Blythe Dickman at Caltech. The measurement set-up is shown in Fig. 2.31. A piece of absorber was placed behind the rexolite slab for the reflection measurement and provides isolation from the environment. Fig. 2.32 shows excellent agreement between simulation and measurement. Time-domain gating has been used to eliminate multiple reflections from the lenses and horns. To implement time-domain gating the inverse Fourier transform of frequency-domain data is obtained that corresponds to the time-domain s_{11} and s_{21} response. Then the gating is applied over the time-domain response that includes the main reflection response and multiple reflections within the slab. Then, the Fourier transform of the gated time-domain response is taken that gives the frequency domain s-parametrs. The result is that the gated re-

sponse is a smooth curve which is the average of the ungated response. A detailed discussion of this technique is described by Ghodgaonkar *et al.* [12-14].
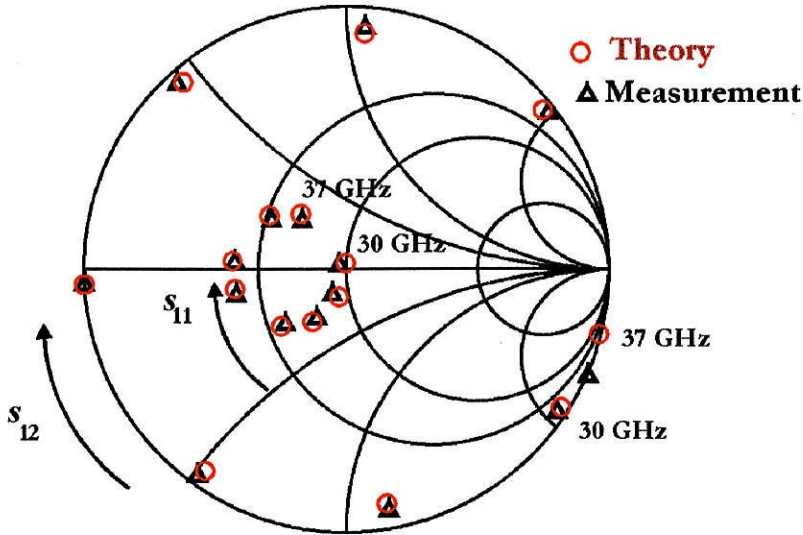

**Fig. 2.32.** Transmission and reflection measurements of a 2.5- cm polysterene slab (er=2.45).

The measured performances of the passive structures with the three different terminations are shown in Fig. 2.33–2.35. Agreement between the scattering-parameter model and the measurements is good. Gating has been used to eliminate the multiple reflections from the lenses and the horns.
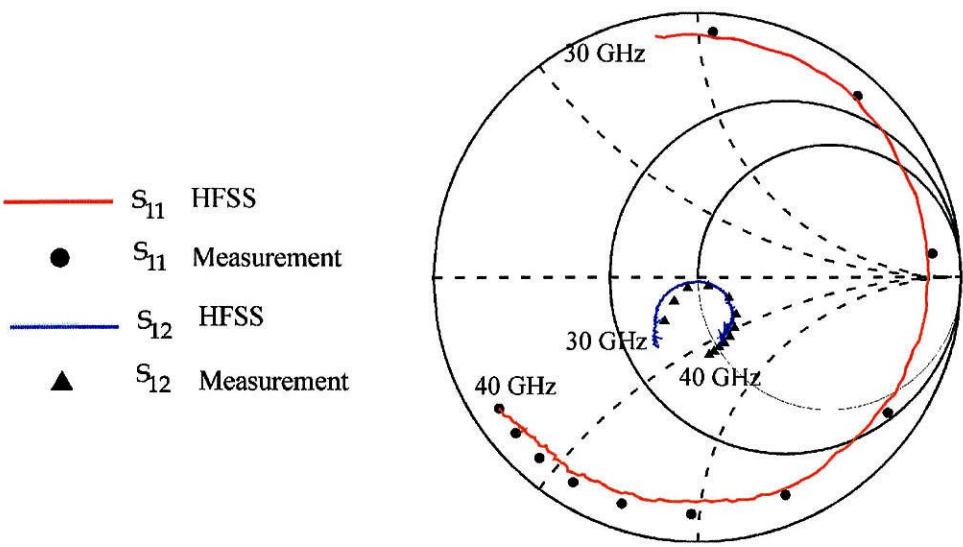
Fig. 2.33. Simulated and measured scattering parameters of the passive array with open-circuit terminations. The red line shows the measurement.
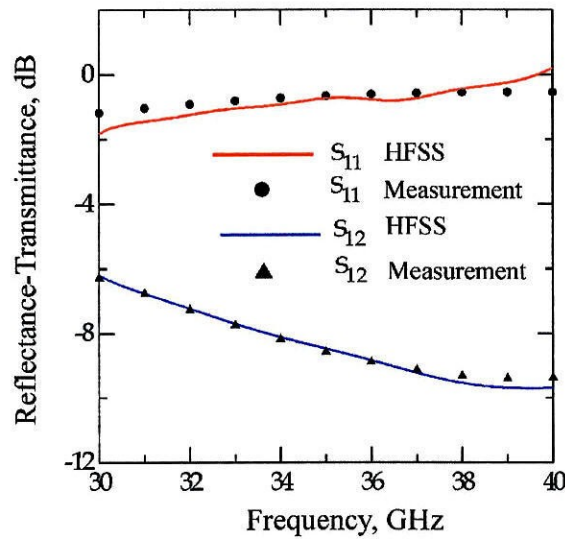
Fig. 2.34. Simulated and measured scattering parameters of the passive array with short-circuit terminations. The red line shows the measurement.
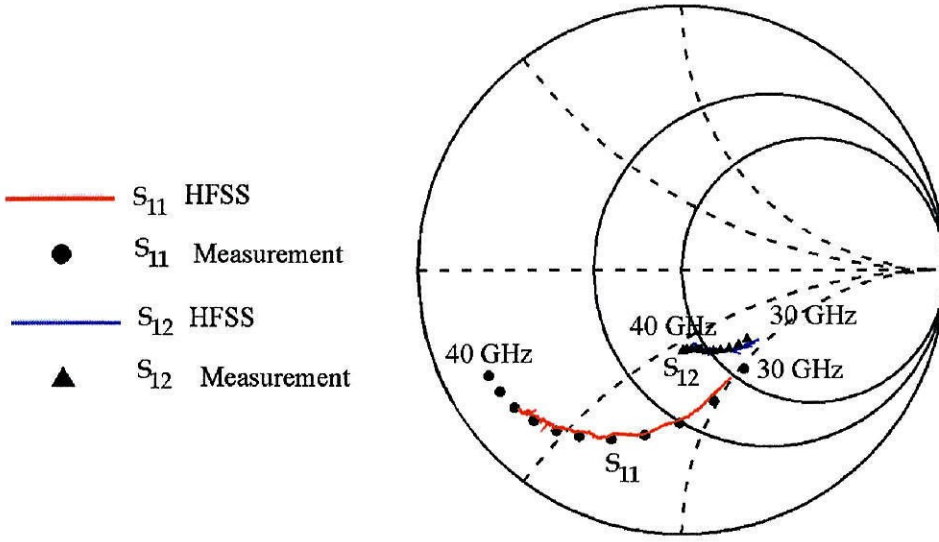
Fig. 2.35. Simulated and measured scattering parameters of the passive array with 75Ω termi-nations. The red line shows the measurement.

2.5 SUMMARY

In this chapter, two models for the design of quasi-optical grid amplifiers based on Ansoft HFSS have been presented. These models account for mutual coupling between the lines of the grid and for parasitic inductances. The models were used to accurately predict the gain of a 10×10 grid amplifier even though substrate modes and edge effects are neglected. On the other hand, M.B. Steer in his full-wave analysis of a 2×2 grid amplifier, included edge effects and sub-strate modes but limited the layout of a unit cell to a simple metal shape and overpredicted the gain of the array. Finally, the scattering parameter model was validated by measuring the scattering parameters of three passive arrays with different terminations.

References

[1] M.P. De Lisio, S.W. Duncan, D.-W. Tu, C.-M. Liu, A. Moussessian, J.J. Rosenberg, D.B. Rutledge, "Modelling and Performance of a 100-Element pHEMT Grid Amplifier," *IEEE Trans. Microwave Theory Tech.*, vol. 44, pp. 2136–2144, Dec. 1996

[2] C.-M. Liu, E.A. Sovero, M.P. De Lisio, A. Moussessian, J.J. Rosenberg, D.B. Rutledge, " Gain ans Stability Models for HBT Grid Amplifiers" *IEEE AP-S Int. Symp. Dig.*, pp. 1292–1295, 1995.

[3] C.-M. Liu, E.A. Sovero, W.J. Ho, J.A. Higgins, M.P. De Lisio, D.B. Rutledge, "Monolithic 40-GHz 670-mW HBT Grid Amplifier," *IEEE MTT-S Int. Microwave Symp.*, pp. 17–31, 1996.

[4] M.P. De Lisio, S.W. Duncan, D.-W. Tu, S. Weinreb, C.-M. Liu, D.B. Rutledge, "A 44-60 GHz Monolithic pHEPT Grid Amplifier," *IEEE MTT-S Int. Microwave Symp.*, pp. 32–56, 1996.

[5] Robert M. Weikle, II, "Quasi-Optical Planar Grids for Microwave and Millim eter-Wave Power Combining," *Ph.D. Dissertation*, California Institute of Technology, 1992.

[6] Z.B. Popovic, R.M. Weikle, M. Kim, D.B. Rutledge, "A 100-MESFET Planar Grid Oscillator," *IEEE Trans. on Microwave Theory and Tech.*, pp. 823–826, 1994.

[7] M.A. Summers, C.E. Christoffersen, A.I. Khalil, S. Nakazawa, T.W. Nuteson, M.B. Steer, J.W. Mink, "An Integrated electromagnetic and nonlinear circuit simulation environment for spatial power combining systems," *IEEE MTT-S Int. Microwave Symp. Dig.*, pp. 1473–1476, June 1998.

[8] F.Nusseibeh, T.W Nuteson, J. Patwardhan, M.A Summers, C.E. Christoffersen, J. Kreskovsky, M.B. Steer, "Computer Aided Engineering Environment for Spatial Power Combining Systems," *IEEE MTT-S Int. Microwave Symp. Dig.*, pp. 1073–1076, June 1997.

[9] Ansoft Corp. HFSS Version 5.0.

[10] Polly Preventza, Blythe Dickman, E. Sovero, M.P. De Lisio, J.J. Rosenberg, D.B. Rutledge, "Modeling of Quasi-Optical Arrays" *IEEE MTT-S Int. Microwave Symp.*, June 1999.

[11] D.R. Gagnon, "Highly Sensitive Measurements With a Lens-Focused Reflectometer," *IEEE Trans. on Microwave Theory and Tech.*, (39), pp. 2237–2240, Dec. 1991.

[12] D.K. Ghodgaonkar, V.V. Varadan, V.K. Varadan, "Free-Space Measurement of Complex Permittivity and Complex Permeability of Magnetic Materials at Microwave Frequencies," *IEEE Trans. on Instrumentation and Measurement*, vol. 39, pp. 387–394, April 1990.

[13] D.K. Ghodgaonkar, V.V. Varadan, V.K. Varadan, "A free-space method for measurement of dielectric constants and loss tangents at microwave frequencies," *IEEE Trans. on Instrumentation and Measurement*, vol. 38, pp. 789–793, 1989.

[14] V.V. Varadan, R.D. Hollinger, D.K. Ghodgaonkar, V.K. Varadan, "Free-Space, Broadband Measurements of High-Temperature, Complex Dielectric Properties at Microwave Frequencies," *IEEE Trans. on Instrumentation and Measurement.*, vol. 40, pp. 842–846, Oct. 1991.

[15] Richard J. Wylde, Derek H. Martin, "Gaussian Beam-Mode Analysis and Phase-Centers of Corrugated Feed Horns," *IEEE Trans. on Microwave Theory and Tech.*, vol. 41, pp. 1691–1699, Oct. 1993.

[16] Paul F. Goldsmith, "Quasi-Optical Systems," *IEEE PRESS*.

[17] D. Rytting, "Advances in microwave error correction techniques," *Hewlett-Packard, RF and MW Symp.*, pp. 5954–8378, June 1987.

[18] D. Rytting, "Let time domain response provide additional insight into network behaviour," *Hewlett-Packard, RF and MW Symp.*, pp. 5952–6660, Mar. 1985.

49

Chapter 3

Ka Band Flip-Chip Amplifier

This chapter discusses a 36-element Ka-Band Flip-Chip InP High Electron Mobility Transistor (HEMT) grid amplifier. The gain model for the grid amplifier is presented in chapter 2. The active devices are custom-made differential-pair flip-chip HEMT's, fabricated at Hughes Research Laboratories by Dr. Mehran Matloubian. The flip-chip technology has many advantages for the development of quasi-optical arrays: It optimizes the substrates separately from the semiconductor array, it potentially increases the array size for higher output powers without suffering from yield problems, it uses an automated assembly to build the quasi-optical arrays, it reduces the cycle time for new array development and finally it could integrate different device technologies onto the same array substrate. The amplifier has a measured gain of 3 dB at 34.5 GHz.

3.1. INTRODUCTION

A quasi-optical grid amplifier is a two-dimensional periodic array that can be considered as a free-space power combiner. Many field effect and HBT transistors have been used to develop grid amplifiers. Both hybrid (discrete devices individually attached on a separate substrate) and monolithic designs have been successful. The approach is shown in Fig. 3.1. Differential pairs of transistors with orthogonal input and output lines form the unit cell.
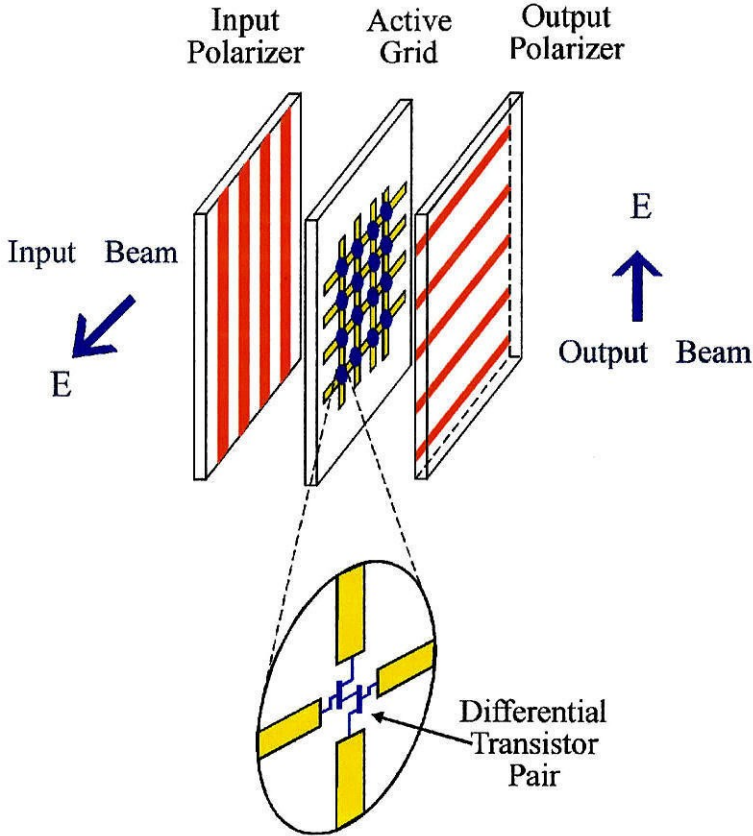
Fig. 3.1. Grid amplifier. A horizontally polarized beam is incident from the left. The output beam is vertically polarized and radiates to the right. The metal-strip polarizers tune the input and output independently.

A horizontally polarized input beam is incident from the left, it excites rf currents on the horizontal-input lead, and the transistor is driven in the differential mode. The output currents are vertically polarized. Independent tuning is provided by the input and output strip-polarizers. These polarizers provide good isolation between the input and output circuit and they reduce the risk for potential feedback oscillations.

The first grid amplifier was a 25-element MESFET grid amplifier developed by Moonil Kim at Caltech [1]. The second grid amplifier was also developed by Moonil Kim at Caltech [2]. This grid used 100 custom-made differential-pair HBT chips (cells) fabricated by Rockwell International Center. It operated between 8 GHz and 12 GHz with a maximum gain of 10 dB, and a 3 dB gain bandwidth of 1 GHz. The measured noise figure was 7 dB and the saturated output power was 450 mW. A hybrid differential-pair pHEMT grid was also demonstrated by De Lisio *et al.* [3]. This is a 100-cell array that had a 3 dB bandwidth of 15% at 9 GHz. The amplifier grid had a minimum noise figure of 3 dB and 12 dB gain at 9 GHz. A similar but monolithic design approach has been used for a 36-element amplifier grid operating in the 44 to 60 GHz range [4]. The operating frequency range of the amplifier could be varied by varying the position of external tuning elements. A maximum gain of 6.5 dB was measured at 44 GHz and the bandwidth when the amplifier was tuned at 54 GHz was 6%. Also a 36-element monolithic HBT amplifier grid [5,6] has been developed. The peak gain of the array is 5 dB at 40 GHz. The amplifier output power is 670 mW. Other monolithic millimeter-wave quasi-optical arrays have been demonstrated. Slot-patch amplifier arrays using HBT's [7] and HEMT's [8] have been reported by Rockwell Science Center. Following the success of these amplifiers, a new high power monolithic Ka-band grid amplifier is currently being designed by Blythe Dickman at Caltech and is being fabricated by Rockwell Science Center.

3.2. FLIP-CHIP TECHNOLOGY

Monolithic designs have a lot of advantages especially in millimeter-wave frequencies. They are more compact and they have lower assembly cost because they use a single integrated circuit-chip. On the other hand they have many disadvantages such as higher overall cost for the fabrication, difficult integration of different device technologies, it is hard to scale to larger array sizes and finally

the heat removal can be very difficult. Hybrid circuits are fabricated by individually attaching and bonding the devices to a substrate. One main advantage of the hybrid technology is that different substrates with various dielectric constants can be used. Materials other than GaAs, Si or other semiconductor can be utilized like Alumina, AlN that are insulators with high thermal conductivity. This greatly reduces the operating temperature of the transistors and the cost. Table 3.1 shows the cost in $/cm^2 for different substrates.
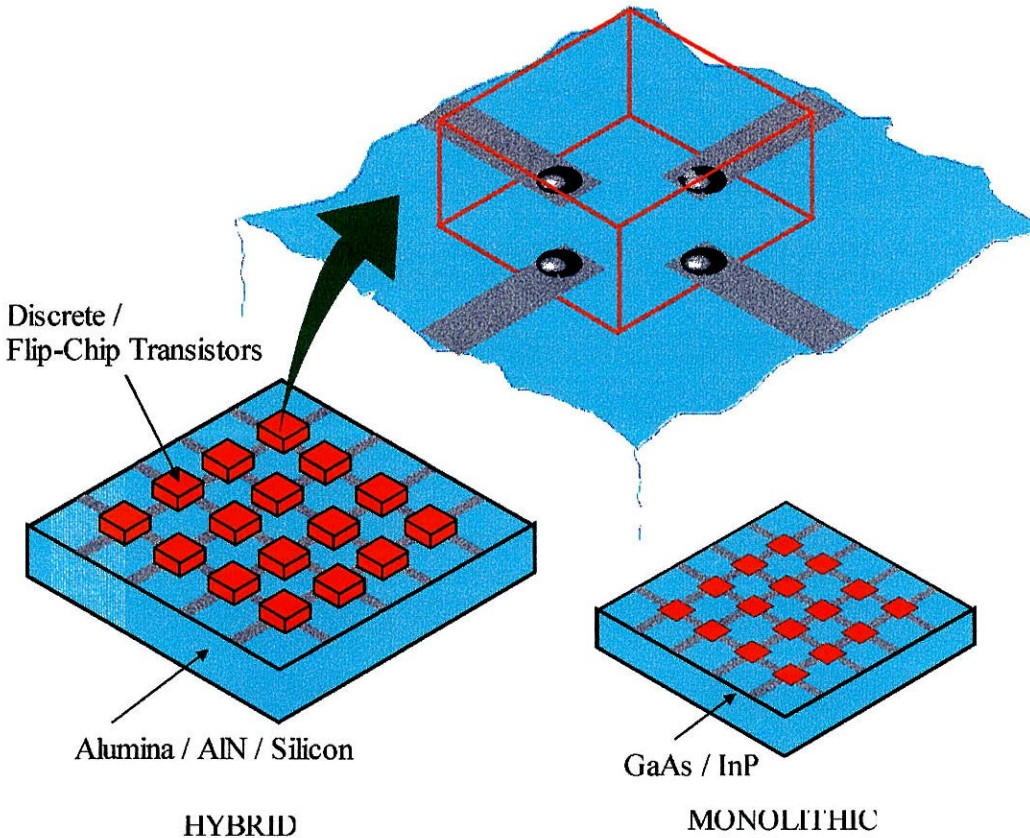
Fig. 3.2. Flip-Chip quasi-optical array. The Flip-Chip technology utilizes substrates with different dielectric constants and thermal conductivities as opposed to the monolithic approach.

Other advantages of the Flip-Chip technology include integration of different device technologies, feasible replacement and easy repair of the array elements as opposed to a monolithic array. In addition, a Flip-Chip array would potentially have a higher yield because the devices are diced and tested before they are mounted on the substrate. On the other hand, there is an additional cost of mounting each transistor individually. The Flip-Chip approach developed at Hughes is shown in Fig. 3.2. Hughes makes hemispherical solder bumps that have a radius of only $25\,\mu$m and has developed the equipment for mounting them automatically and accurately. Fig. 3.3(a) shows a $0.25\,$mm^2 HEMT chip with a $50\,\mu$m diameter SnPb bumps with height of $25\,\mu$m. Fig. 3.3(b) shows the photograph of a $17\,$GHz flip-chip VCO, where the integration of different device technologies is demonstrated.

Another advantage of Flip-Fhip technology that is especially important at millimeter-wave frequencies is the elimination of the bond wires and their parasitic inductance. Fig. 3.4 shows a comparison of interconnect loss between wirebond and Flip-Chip. At millimeter wave frequencies, Flip-Chip interconnects have significantly lower loss than wire-bonds [9].

SUBSTRATE	COST \$ /cm^2
Duroid	0.10
High Resistivity Silicon	0.30
Aluminum Nitride	1.25
GaAs (with epi layer)	30
InP (with epi layer)	75

Table 3.1. Comparison of substrate cost.
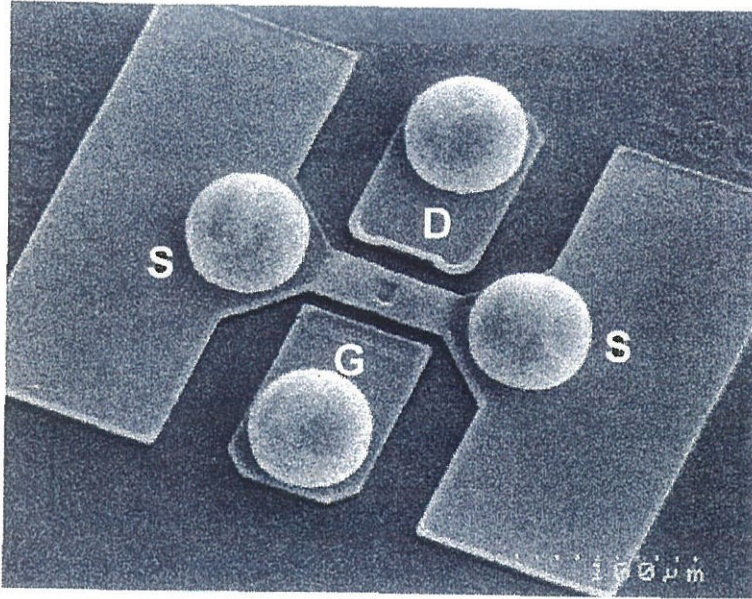
(a)
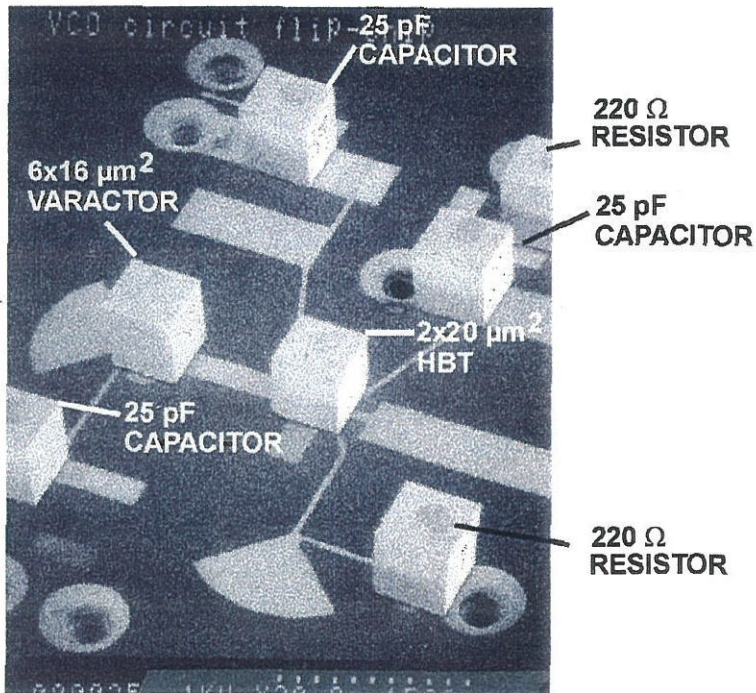
(b)

Fig. 3.3. (a) Photograph of a HEMT transistor with $50\,\mu$m diameter SnPb bumps with height of $25\,\mu$m. (b) Photograph of a 17 GHz Flip-Chip VCO.
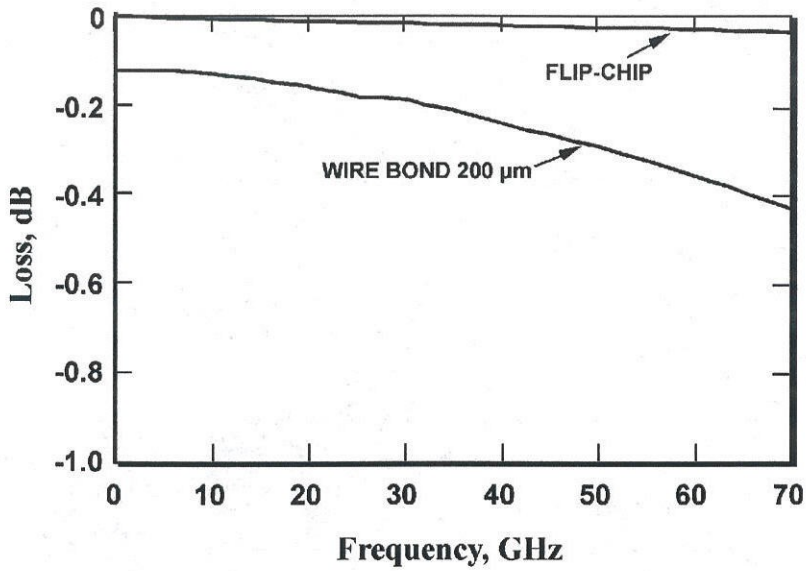
Fig. 3.4. Comparison of interconnect loss. Wire-bond vs Flip-Chip.
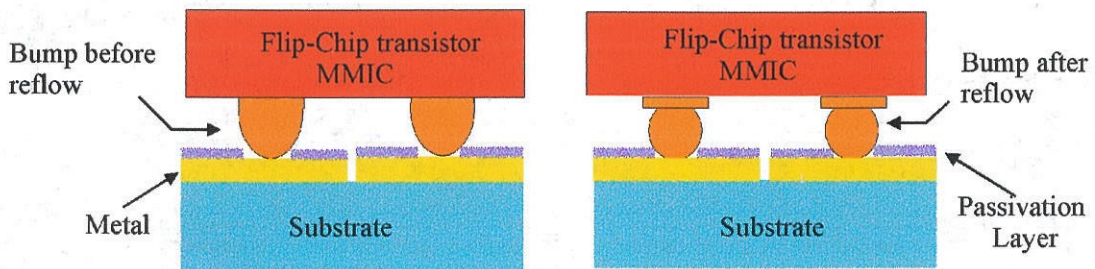
Fig. 3.5. Self-alignment of Flip-Chip components after solder reflow.

Fig. 3.5 demonstrates how after solder reflow the chip self-aligns to the metal pad. Alignment accuracy of $\approx 2\,\mu$m using placement accuracy of $25\,\mu$m can be acheived.

3.3. GRID AMPLIFIER MODELLING

The grid amplifier configuration is shown in Fig. 3.6. The grid is constructed on a substrate with a relative dielectric constant ε_r and thickness t_s.
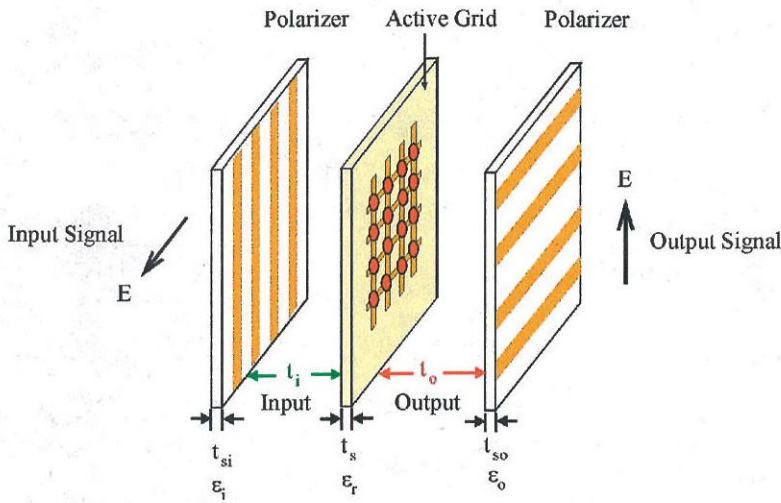
Fig. 3.6. Perspective view of a grid amplifier.
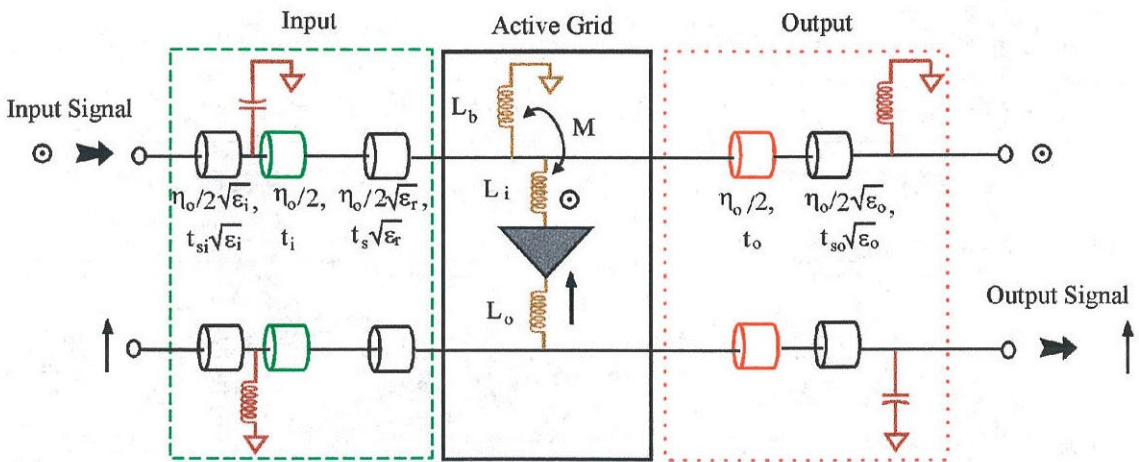
Fig. 3.7. Transmission-line equivalent circuit for the half-cell model of the amplifier configuration of Fig. 3.6.

The input and output polarizers are metallic gratings constructed on substrates with dielectric constants ε_i and ε_o, and thicknesses t_{si} and t_{so}. The polarizers are located a distance t_i and t_o from the grid. By exploiting the symmetry of the grid, a unit-cell [10,11] can be defined that greatly simplifies the analysis of the grid. A transmission-line equivalent circuit for the amplifier configuration of Fig. 3.6 is shown in Fig. 3.7. Transmission lines with appropriate electrical lengths and characteristic impedances represent the air gaps and the substrates. The free-space portions between the polarizers and the grid are represented by transmission lines with characteristic impedance $\eta_o = 377\Omega$ (the transverse electromagnetic-TEM wave impedance for free-space), and electrical lengths $t_{i,o}$.
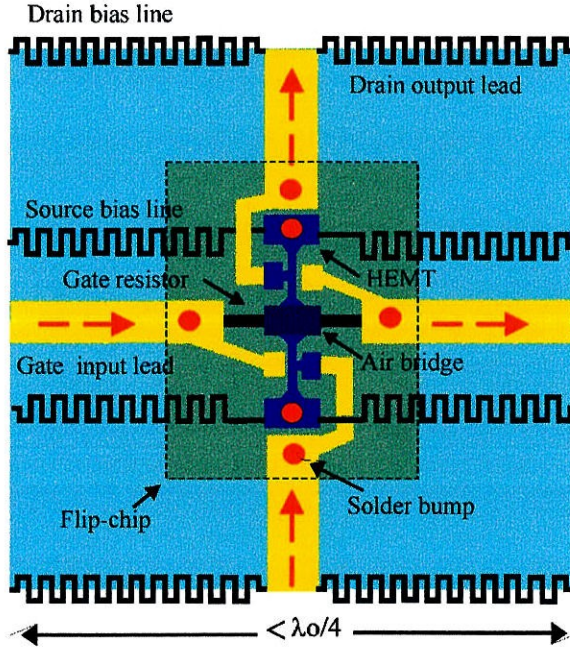
Fig. 3.8. Unit cell for a Flip-Chip transistor grid.

The polarizers are also modelled as transmission lines with characteristic impedance $\eta_o/\sqrt{\varepsilon_{i,o}}$ where ε_i and ε_o are the relative dielectric constants of the

substrates for the input and output polarizers respectively. The electrical lenghts of the polarizers are $t_{si,so}\sqrt{\varepsilon_{i,o}}$. For a wave polarized along the direction of the metal strips, the polarizer is modelled as an inductor, and for a wave polarized orthogonal to the metal strips, the polarizer is modelled as a capacitor. Fig. 3.7 shows the equivalent transmission line circuit that corresponds to a half cell. The characteristic impedances of free space and all transmission lines become half of the values mentioned above while the electrical lengths remain the same. Inductors L_i and L_o represent coupling through the input and output leads, and L_b represents the inductance of the bias lines. The mutual coupling, M, between the gate lead and the bias lines is also taken into account. The mutual coupling effect was discussed in chapter 2. Fig. 3.8 shows the unit cell of the Flip-Chip amplifier.

3.4. BIAS LINES

The thin bias lines for the source and the drain are horizontally directed, and they appear in the equivalent transmission line circuit as a shunt inductance, L_b. To avoid shorting out the input of the grid, these lines should be made highly reactive thus increasing the input-lead inductance. To achieve high bias-line inductance without increasing the dimensions of the unit cell, different shapes were attempted. Various bias-lines configurations were simulated using HFSS. The corresponding half-unit cells and their equivalent inductances are shown in Fig. 3.9. We see that as the effective length of the lines, increases the reactive impedance also increases. The Ω-line, shown in Fig. 3.9d, has the highest impedance and the straight line, shown in Fig. 3.9a, has the lowest impedance. All lines have the same width, $10\,\mu m$, and the simulations are carried out from $30\,GHz$ to $40\,GHz$. The cell is $1\,mm$ on the side.
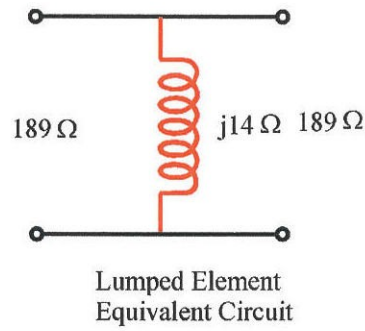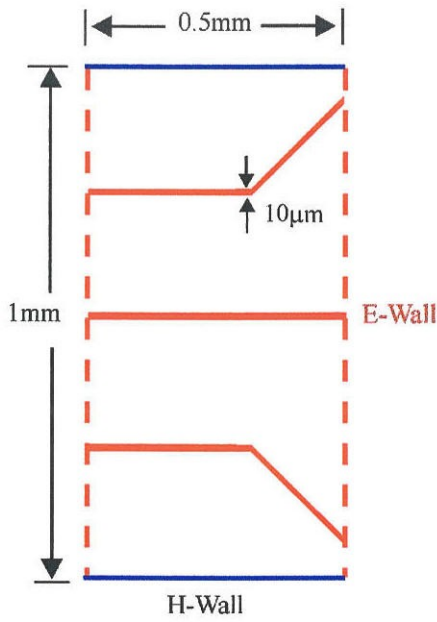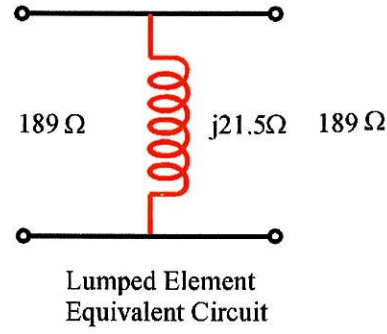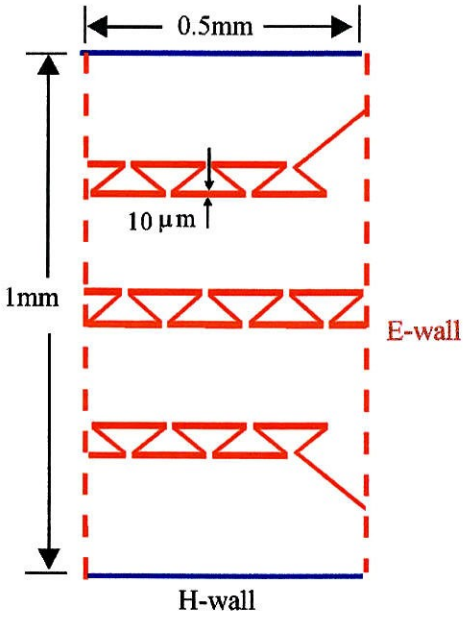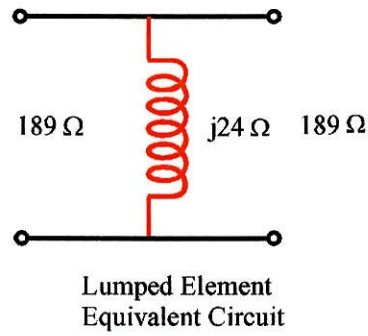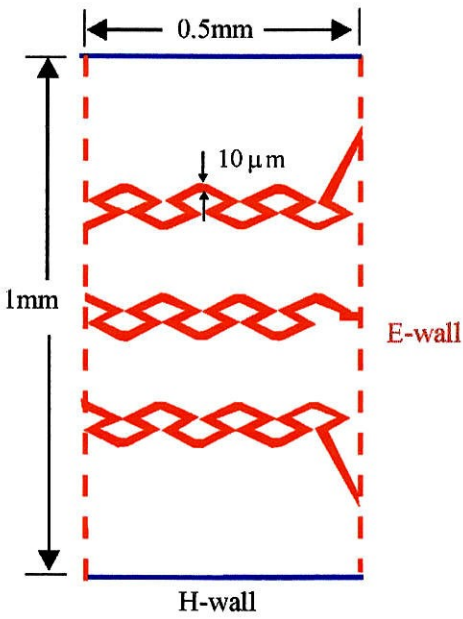
(a)
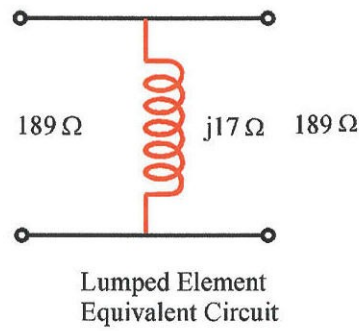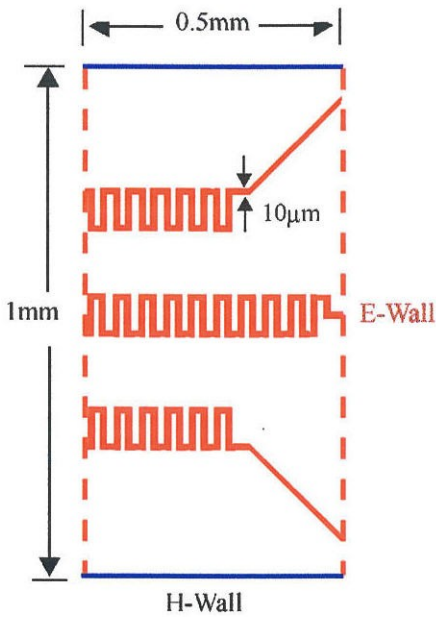
(b)

**Fig. 3.9.** HFSS for various bias-line configurations and their equivalent circuits.

60

(c)

(d)

Fig. 3.9. (continued)

Fig. 3.10 shows the effect of the mutual coupling on the total inductance of the bias lines. A straight 10-μm wide line has lower inductance than a meandering line with the same width. Simulations for two and three parallel meandering lines are carried out. It is seen that due to the mutual coupling between the lines, two parallel meandering lines have less than half the value of the inductance of the parallel combination of two isolated single meandering lines.
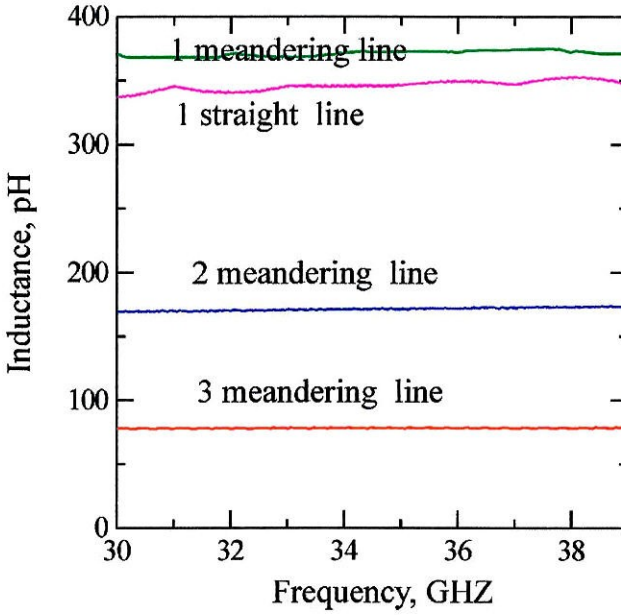
Fig. 3.10. Comparison of inductance values for one, two and three meandering lines.

3.5. Grid Design and Construction

The differential-pair chips used in this project were fabricated by Hughes Research Labs in Malibu by Dr. Mehran Matloubian. The active devices are AlInAs/GaInAs/InP Flip-Chip HEMT's. The total gate width per transistor is 100 μm distributed among four fingers. Further details regarding the device can be found in [12].
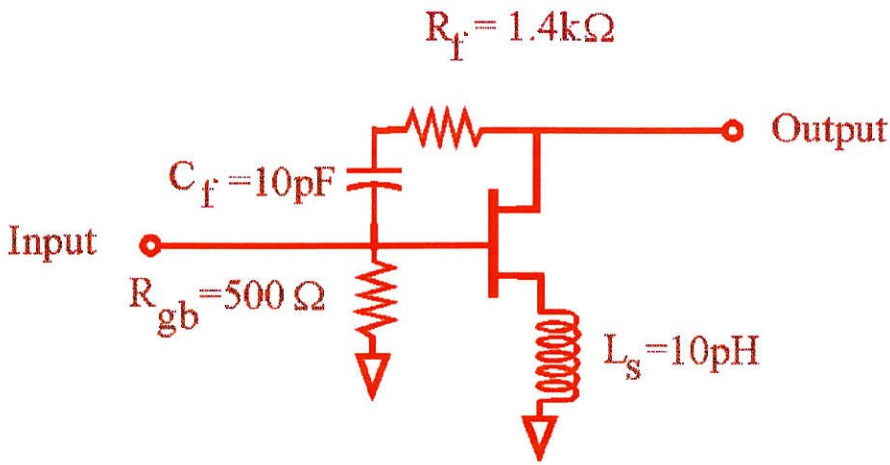
**Fig. 3.11.** Half-cell transistor with feedback elements.
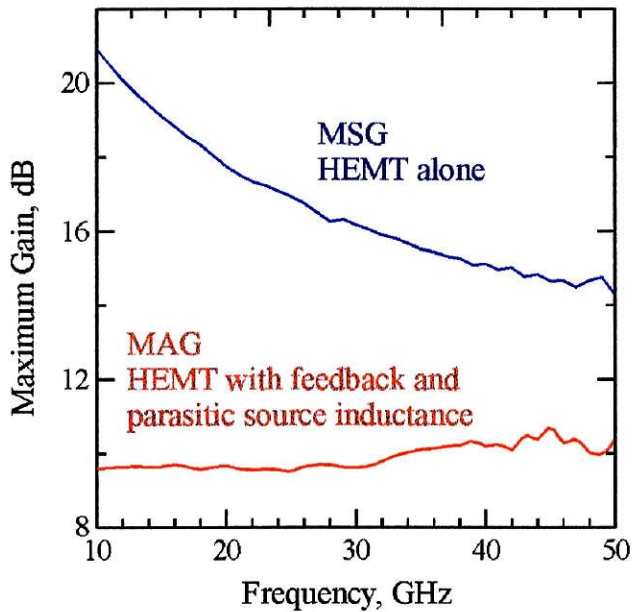
Fig. 3.12. Maximum stable gain of the HEMT with and without the feedback and source inductance.

The sources of two HEMT's are tied together to form a differential pair.

The control terminal can be externally biased. The 1-kΩ resistor allows the gate control bias voltage to pass from cell to cell. The gate draws bias current at the μA range. The gate bias resistor passes under the air-bridged source connection. To help stabilize the amplifier (two-port stability), a 1.4-kΩ resistor and a 10-pF capacitor are added as feedback elements. Fig. 3.11 shows a single HEMT with the gate bias resistor R_{gb}, and the gate-drain feedback network R_f and C_f. Parasitic inductance of $L_s = 10pH$ is also added. Fig. 3.12 shows the Maximum Stable Gain (MSG) for the HEMT, and the Maximum Available Gain (MAG) for the transistor with the feedback and the parasitic source inductance. These elements tend to reduce the gain available from the transistor. At 35 GHz the MSG for the HEMT is 16 dB and the MAG for the transistor with the R_{gb}, R_f and C_f is 10 dB.

The unit cell is shown in Fig. 3.13. The cell is 1 mm on the side. The input lead is 274-μm wide and the output lead is 10-μm wide. Bias to the drain and the source is provided by the Ω- line.
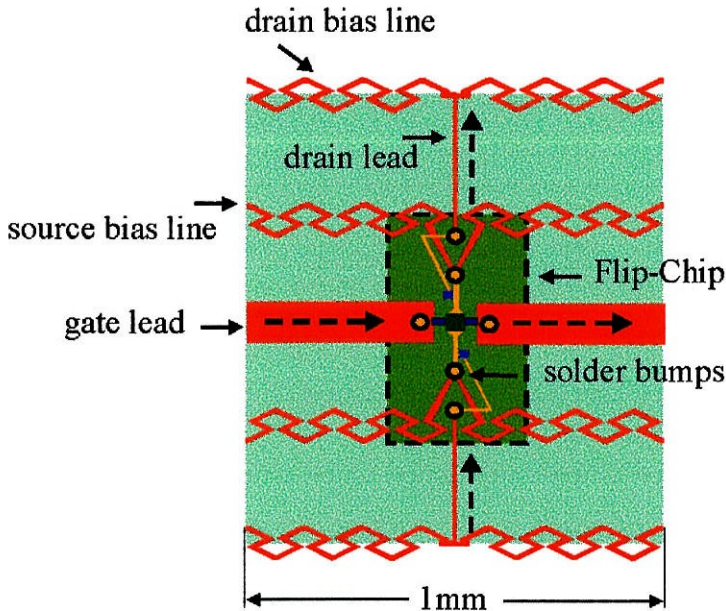
Fig. 3.13. The grid amplifier unit-cell. Arrows indicate the direction of rf currents.
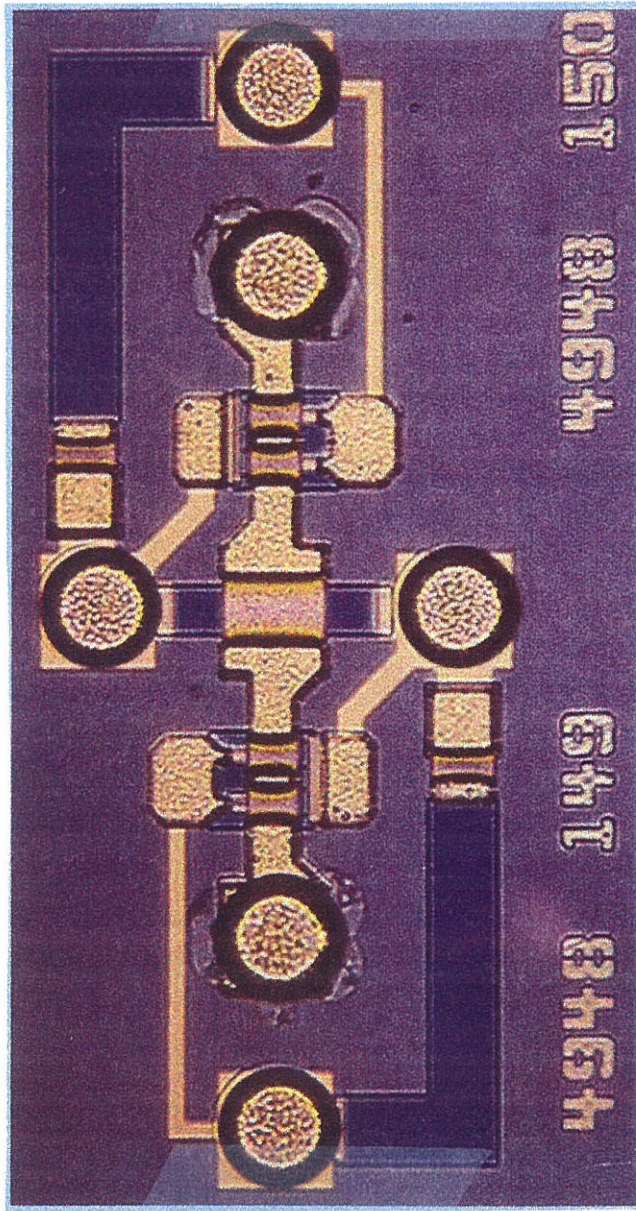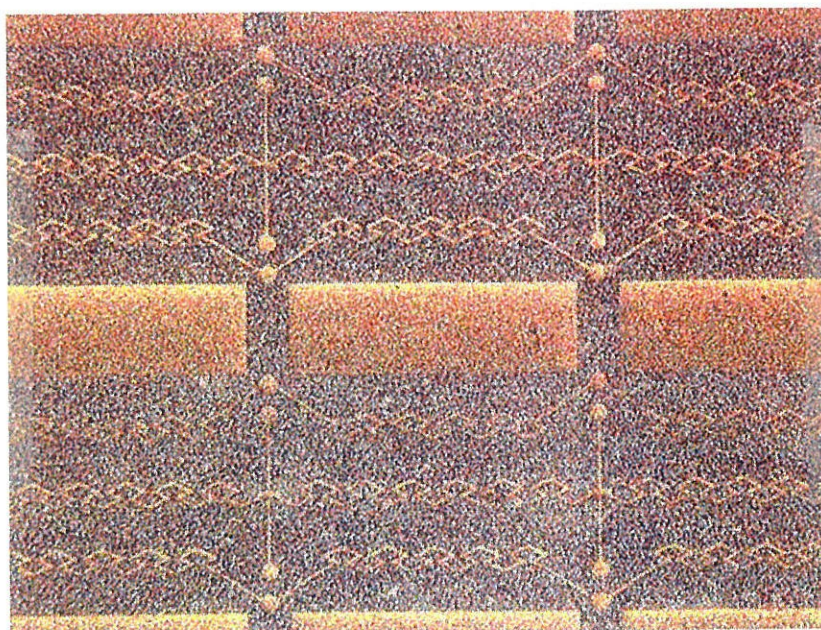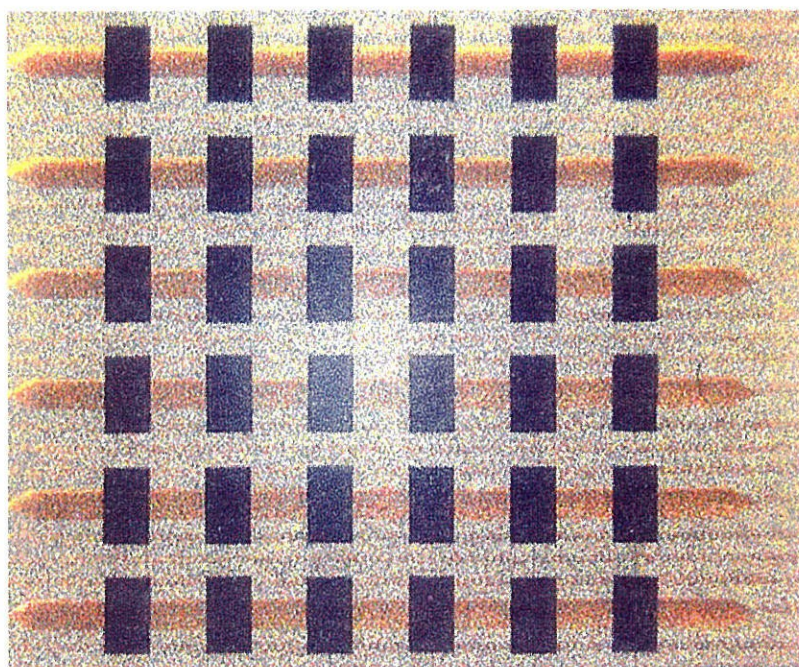
Fig. 3.14. The Flip-Chip differential pair HEMT.

As it was discussed in section 3.4, the Ω-bias line is highly reactive to avoid shorting out the input of the grid. At the same time, the increasing effective length and the small width increases the resistance of the line, thereby causing
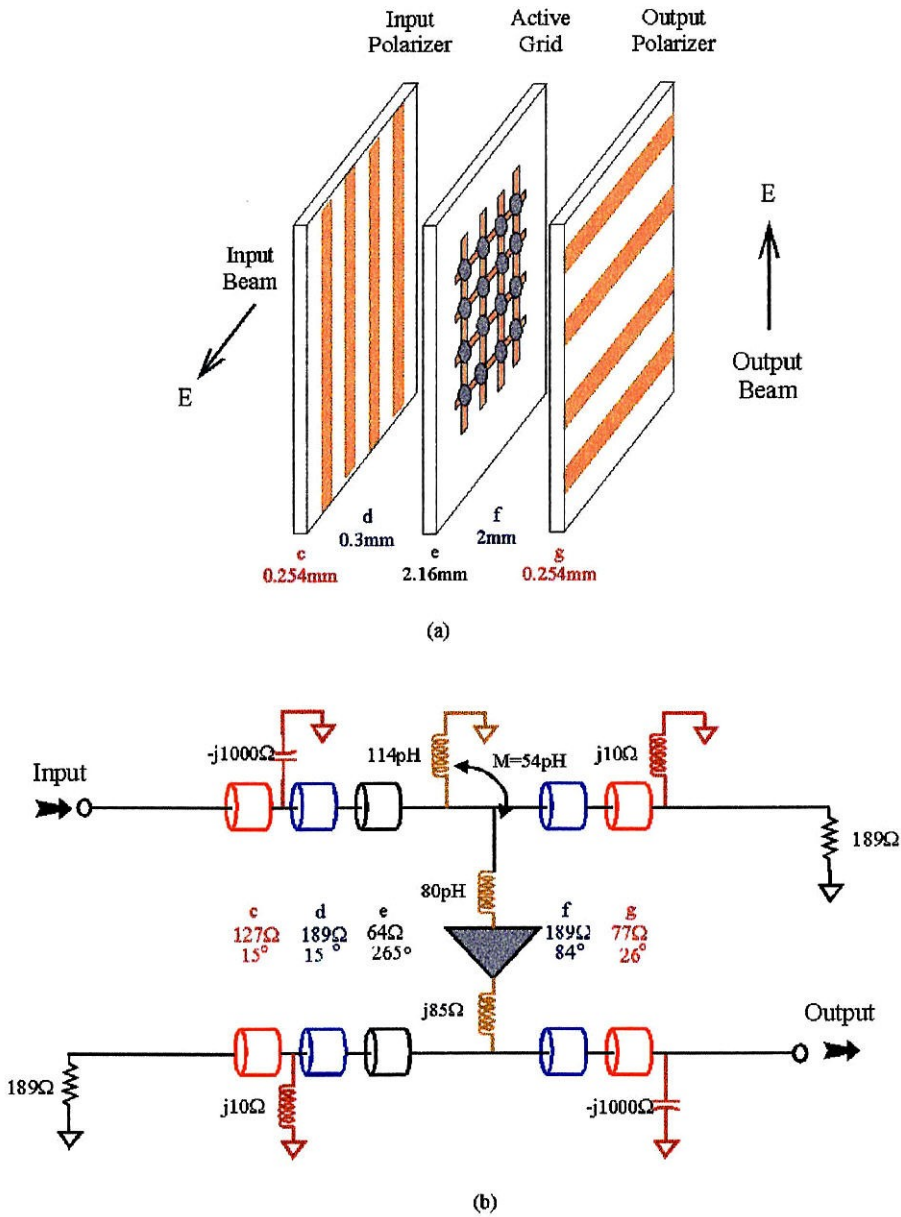
(a)

(b)

Fig. 3.15. (a) Photograph of several unit cells and (b) photograph of the entire 36-element grid with the Flip-Chips attached on the AlN substrate.

a voltage drop. A photograph of the chip is shown in Fig. 3.14. A 6×6 array of these cells was fabricated onto a 85-mil Aluminum Nitride with a relative dielectric constant of 8.6.


(a)

(b)

Fig. 3.16. (a) The assembled amplifier grid and (b) the transmission-line equivalent circuit model for the amplifier tuned at 35 GHz.

Fig. 3.15(a) shows a photograph of several unit cells without the flip-chips attached. Fig. 3.15(b) shows the entire 36-element HEMT grid amplifier.

3.6. THERMAL BEHAVIOUR

The active devices are mounted on a thick (2.16 mm) aluminum nitride substrate. AlN has a high thermal conductivity (170 W/m/°C) that greatly reduces the operating temperature of the transistors and consequently could improve the amplifier performance.
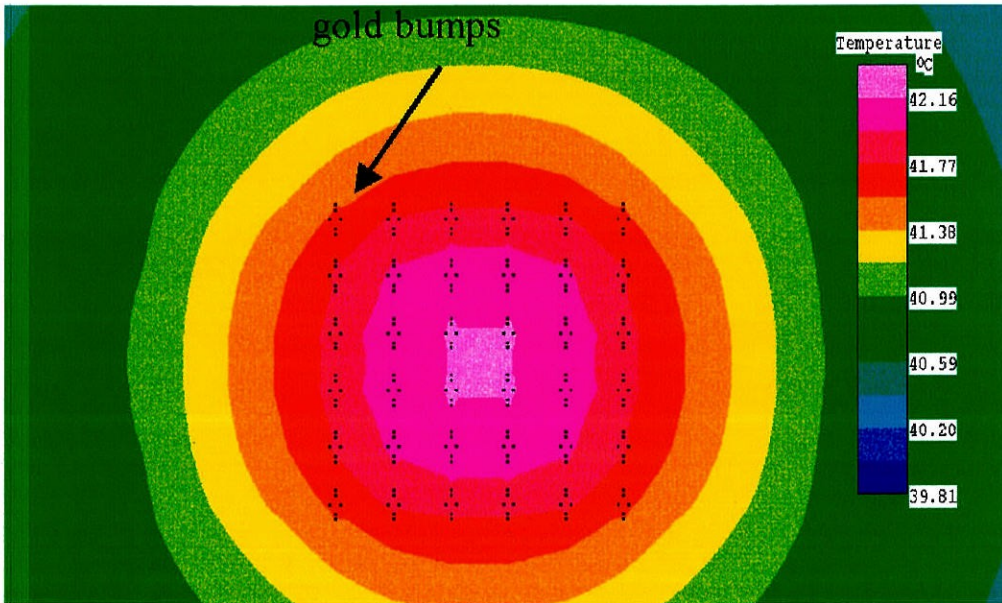
Fig. 3.17. Temperature rise due to the gold bumps and the AlN substrate.

Other substrate candidates would be Si and diamond that also have a high thermal conductance: 150 W/m/°C, and ≈1000 W/m/°C respectively. To calculate the temperature rise due to the solder bumps and the AlN carrier, we assume that each differential pair dissipates 60 mW. The substrate is 5.08 cm on the side and it is 2.16 mm thick. The bumps are assumed to be square, 50 μm on the side and 25 μm high. The bumps are made of gold that has a thermal conductivity of

296 W/m/°C. Fig. 3.17 shows the temperature profile due to the bumps and substrate. The peak temperature rise is 42°C, assuming each transistor dissipates 60 mW. Figure 3.18 shows the temperature profile for the same grid, assuming water cooling is applied to the back of the grid. Then, the peak temperature rise is only 2°C.
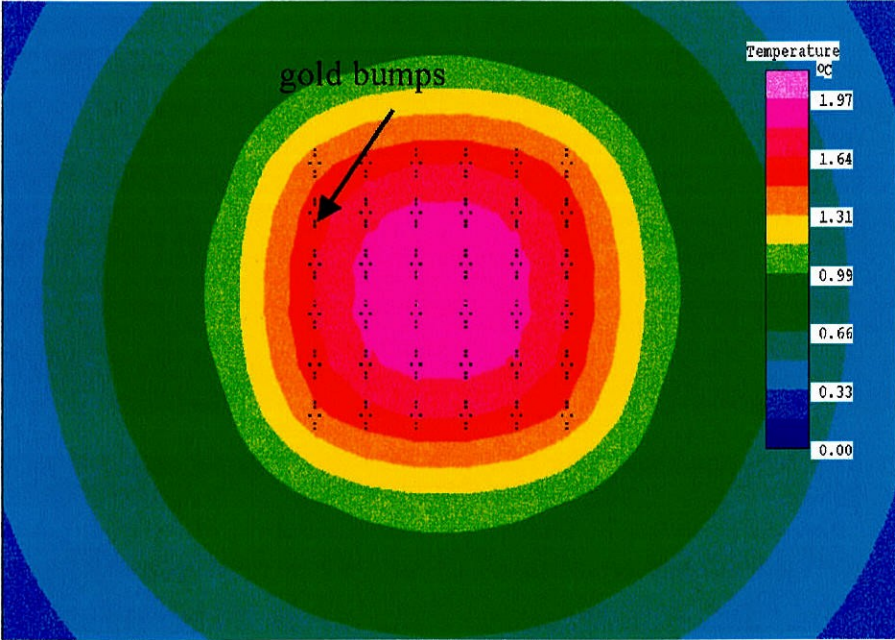

Fig. 3.18. Temperature rise due to the gold bumps and the AlN substrate. Water cooling is applied to the back of the grid.

3.6. GAIN MEASUREMENTS

The gain measurement technique is the same as the one discussed in section 2.6. The assembled grid is shown in Fig. 3.16. The polarizers are built on Duroid slabs. The input polarizer is built on a 10-mil Duroid with low dielectric constant, $\varepsilon = 2.2$. The output polarizer is also built on 10-mil Duroid substrate with $\varepsilon = 6$. Fig. 3.17 shows the gain of the amplifier. The peak gain is 3 dB. No tuners were

used in the input and output circuits to optimize the gain. The grid was biased at a drain voltage of 2 V and a total drain current of 800mA. The gates are biased at a gate voltage of -0.38 V. At this point, the measurements stopped because of a shorted transistor. Then, each row has been tested individually to try to locate the bad device. Two shorted devices have been disconnected. The new measurement of the amplifier gain (34 devices) is shown in Fig. 3.18. The peak gain of the amplifier is 4.8 dB.
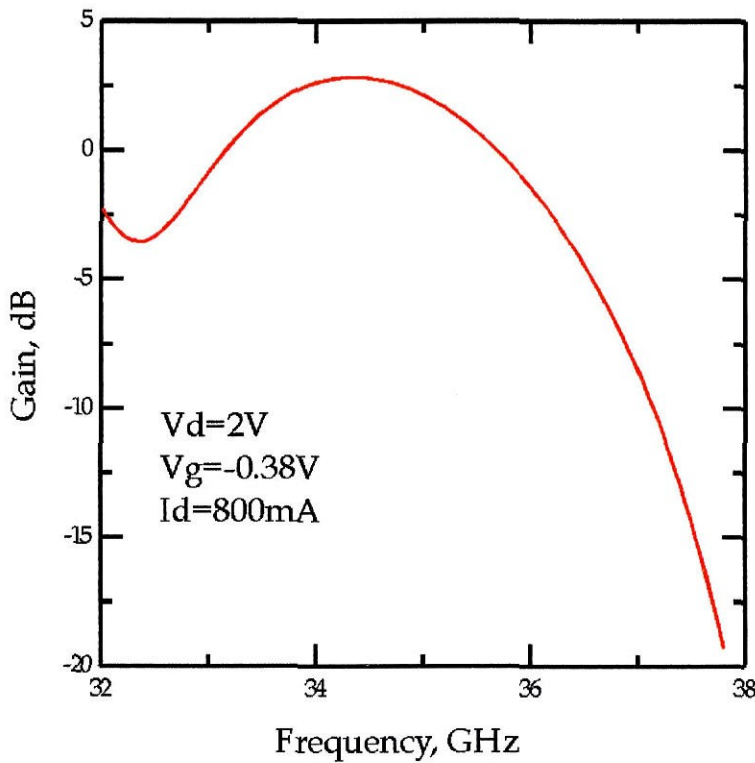

Fig. 3.17. Measured amplifier gain versus frequency.

A new design has been attempted, where straight lines replace the Ω-bias lines. The new design was the result of concerns that the effective length and the width of the Ω-line will cause voltage drop across the rows. The fabricated grid is shown to have leaking gates. Fig. 3.19 shows the voltage drop at the gates of the devices as it is measured from cell to cell across each row. The constant

slope of the plot shows that the proportion of the current that each transistor leaks, is the same for all devices across a row.
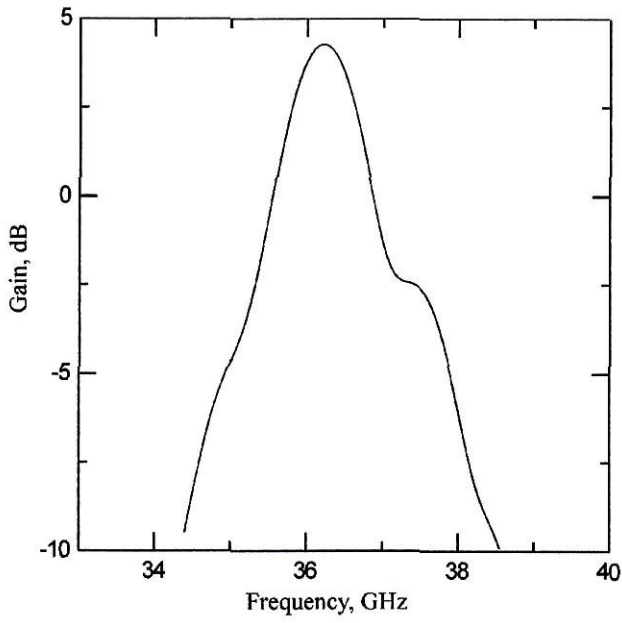
Fig. 3.18. Measured amplifier gain versus frequency.
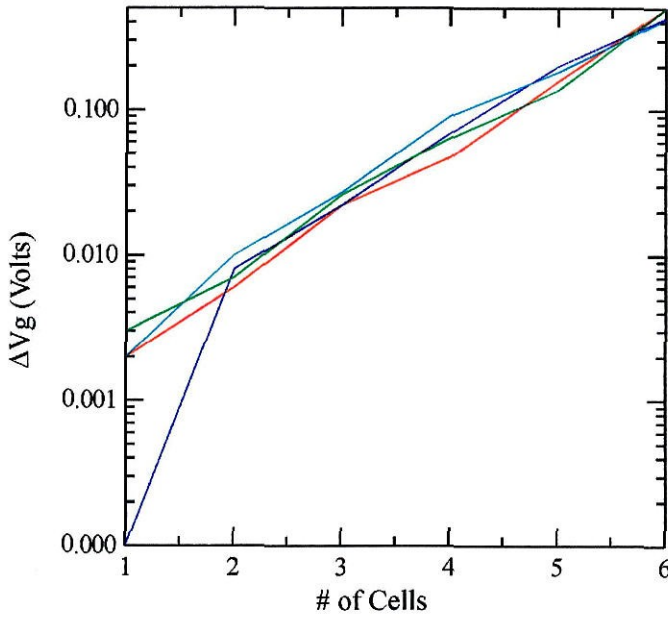
Fig. 3.19. Gate voltage drop from cell to cell across a row.

References

[1] M. Kim, J.J. Rosenberg, R.P. Smith, R.M. Weikle, J.B. Hacker, M.P. De Lisio, D.B. Rutledge, "A Grid Amplifier," *IEEE Microwave Guided Wave Lett.*, vol. 1, pp. 322–324, Nov. 1991.

[2] M. Kim, E.A. Sovero, J.B. Hacker, M.P. De Lisio, J.-C. Chiao, S.-J. Li, D.R. Gagnon, J.J. Rosenberg, D.B. Rutledge, "A 100-Element HBT Grid Amplifier," *IEEE Trans. Microwave Theory Tech.*, vol. 41, pp. 1762–1771, Oct. 1993.

[3] M.P. De Lisio, S.W. Duncan, D.-W. Tu, C.-M. Liu, A. Moussessian, J.J. Rosenberg, D.B. Rutledge, "Modelling and Performance of a 100-Element pHEMT Grid Amplifier," *IEEE Trans. Microwave Theory Tech.*, vol. 44, pp. 2136–2144, December 1996.

[4] M.P. De Lisio, S.W. Duncan, D.-W. Tu, S. Weinreb, C.-M. Liu, D.B. Rutledge, "A 44-60 GHz Monolithic pHEMT Grid Amplifier," *1996 IEEE MTT-S Int. Microwave Symp.*, pp. 1127–1130, 1996.

[5] C.-M. Liu, E.A. Sovero, W.J. Ho, J.A. Higgins, D.B. Rutledge, "A Millimeter-Wave Monolithic Grid Amplifier," *Int. J. Infrared Millimeter Waves*, vol. 16, pp. 1901–1910, Nov. 1995.

[6] C.-M. Liu, E.A. Sovero, W.J. Ho, J.A. Higgins, M.P. De Lisio, D.B. Rutledge, "Monolithic 40-GHz 670-mW HBT Grid Amplifier," *1996 IEEE MTT-S Int. Microwave Symp.*, pp. 1123–1126, 1996.

[7] J.A. Higgins, E.A. Sovero, W.J. Ho, "44-GHz Mpnolithic Plane Wave Amplifiers," *IEEE Microwave Guided Lett.*, MGWL-5, pp. 347–348, October 1995.

[8] E.A. Sovero, Y. Known, D.S. Deakin, A.L. Sailer, J.A. Higgins, "A PHEMT-Based Monolithic Plane Wave Amplifier for 42 GHz," *1996 IEEE MTT-S Int. Microwave Symp.*, pp. 1111–1114, 1996.

[9] Baumann, *26th. European Microwave Conf.*, Sept. 1996.

[10] Z.B. Popovic, R.M. Weikle, M. Kim, and D.B. Rutledge, "A 100-MESFET planar grid oscillator," *IEEE Trans. Microwave Theory Tech.*,vol. 39, pp. 193–200, March 1996.

[11] J.B. Hacker, R.M. Weikle, "Quasi-optical grid arrays," in *Frequency Selective Surface and Grid Array*, T.K. Wu, ed., Wiley, New York, 1995, pp. 249–324.

[12] M. Matloubian, L.M. Jelloian, A.S. Brown, L.D. Nguyen, L.E. Larson, M.J. Delaney, M.A. Thompson, R.A. Rhodes, and J.E. Pence, "V-Band High-Efficiency High-Power AlInAs/GaInAs/InP HEMT's," *IEEE Trans. Microwave Theory Tech.*, vol. 41, pp. 2206-2209, 1993.

Chapter 4

Beam Steering Grid

This chapter proposes a beam-steering method which includes microelec-
tromechanical (MEM) relays on an insulating membrane. The microswitch beam-
steering arrays are fabricated monolithically on highly-doped silicon wafers and
they could provide discrete phase-shifts. In this chapter, finite-element (HFSS)
simulations of a 35 GHz and a 94 GHz 6-layer 2-bit controled structure are car-
ried out. The 94 GHz design predicts maximum loss of 2 dB and maximum phase
error of 1°. The 35 GHz design predicts maximum loss of 2 dB and maximum
phase error of 10°. The chapter will also describe the approaches examined for
the fabrications of membrane-suspended MEM switches. The most promising
technology approach, involves the reactive ion-etching (RIE) of silicon-on-oxide.
Finally measurements of s-parameters of a rectangular-window array with ca-
pacitive metal patterns are done for the design of 94 GHz to verify the resonant
frequencies.

4.1. INTRODUCTION

Quasi-optical beam-steering grids have been developed using diodes at mil-
limeter wavelengths. Qin *et al.* [1,2] has shown that monolithic arrays of
Schottky-contact varactor diodes can produce useful switching and phase shifting
functions. A relatively constant loss of 2.7 dB across a phase-shift range of some
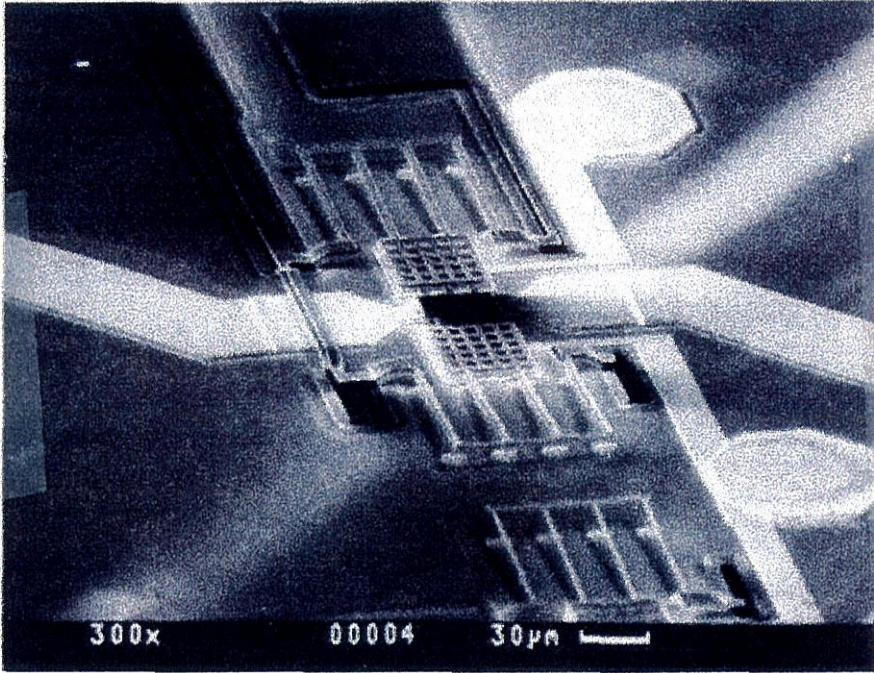130° at 60 GHz was demonstrated.

Fig. 4.1. Micrograph image of a micromachined RF switch design fabricated at Rockwell International Center.
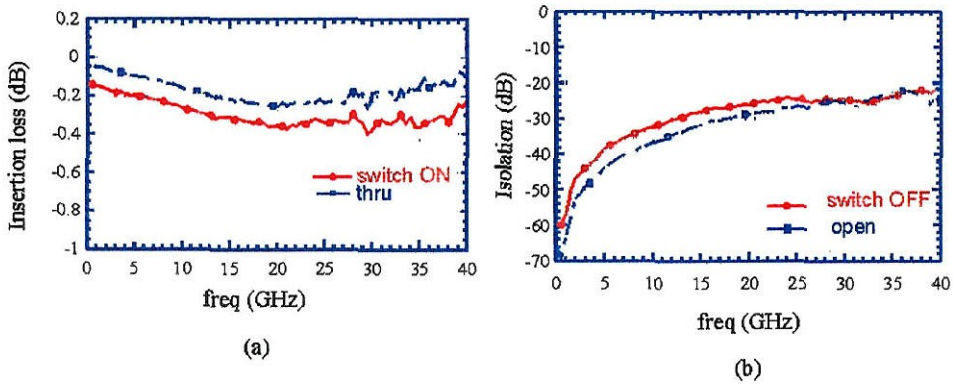

(a)

(b)

Fig. 4.2. Insertion loss and isolation of the RF switch shown in Fig. 4.1.

Choudhury *et al.* [3] developed a beam steering array with Schottky-barrier diodes mounted on GaAs that has a phase shift greater than 70° over most of the 92 to 98- GHz frequency range. A 24 dB ON/OFF ratio and a 2.2 dB transmission loss with one single layer and a 42 dB ON/OFF ratio with a 4 dB loss with two layers is also reported at 60 GHz [1,2].

Even though the diode-grid results are impressive, the series resistance associated with the Schottky diodes increases with the operating frequency thereby causing serious loss problems at millimeter and submillimeter wavelengths. The approach presented in this chapter is based on passive elements instead of active elements which offer the advantage of low series resistances and therefore have the potential for low loss. Yao [4], at the Rockwell International Science Center, developed a surface micromachined miniature switch on a semi-insulating GaAs substrate using a suspended silicon dioxide microbeam as the cantilever arm, a platinum-to-gold electrical contact, and electrostatic actuation as the switching mechanism. The switch has an electrical isolation of -50 dB and an insertion loss of 0.1 dB at 4 GHz. Fig. 4.1 shows a micrograph image of a micromachined RF switch design. The switch is fabricated at the Rockwell International Science Center and has an electrical isolation of -25 dB and an insertion loss of 0.3 dB up to 40 GHz (Fig. 4.2). These are very promising results compared with the state-of- the-art technology that uses compound solid state switches such as GaAs MESFET's [5,6] and PIN diodes [7]. The latter switches have a large insertion loss (typically 1 dB) in the ON state and a poor electrical isolation in the OFF state when the signal frequency becomes greater than 1 GHz. MEMS (Micro-Electro-Mechanical-Systems) technology is an enabling alternative. Based on the MEMS technology, switches are fabricated on SiO_xN_y-membranes suspended on etched highly doped $< 100 >$ silicon wafers. There are several processing challenges in fabricating such a structure. One challenge is protection of the frontside MEM structure during backside substrate removal. Another is making the final membrane flat after the many processing steps involved in MEM structure fabrication. Finally, rigidity of the membrane is required for this application since the relay involves mechanical contact to a metal structure on the membrane. The most promising technology approach involves the reactive ion etching (RIE) of silicon-on-oxide.
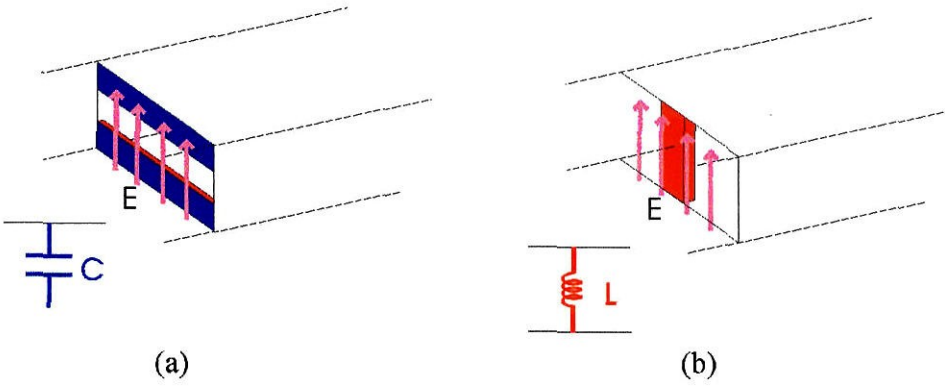
Fig. 4.3. Metal patterns in waveguides and their equivalent circuits.

4.2. TRANSMISSION-TYPE BEAM STEERING

Fig. 4.3 shows the metal patterns in waveguides and their equivalent circuits that simulate the ON/OFF states of the switches by changing the phases of the propagating waves. On the left is a capacitive iris, with an equivalent transmission-line cicruit of a shunt capacitance that corresponds to the OFF state of the switch and causes a phase delay. On the right is an inductive strip, with an equivalent transmission-line circuit of a shunt inductor that corresponds to the ON state of the switch and causes a phase advance. The incident electric field is vertically polarized. Fig. 4.4 shows the transmission-type beam-steering approach. The beam steerer is assembled as a stack of silicon wafers separated by free-space. An incident wave enters the grid from the left side passes through several layers that represent either inductive or capacitive reactances and then reradiates from the right side into free space. Proper free-space electrical lengths between the wafers and the layout of the grid are adjusted to minimize the reflection loss. The number of the layers used in the array determines the steering resolution and the direction of the beam is set by the settings of the binary switches.
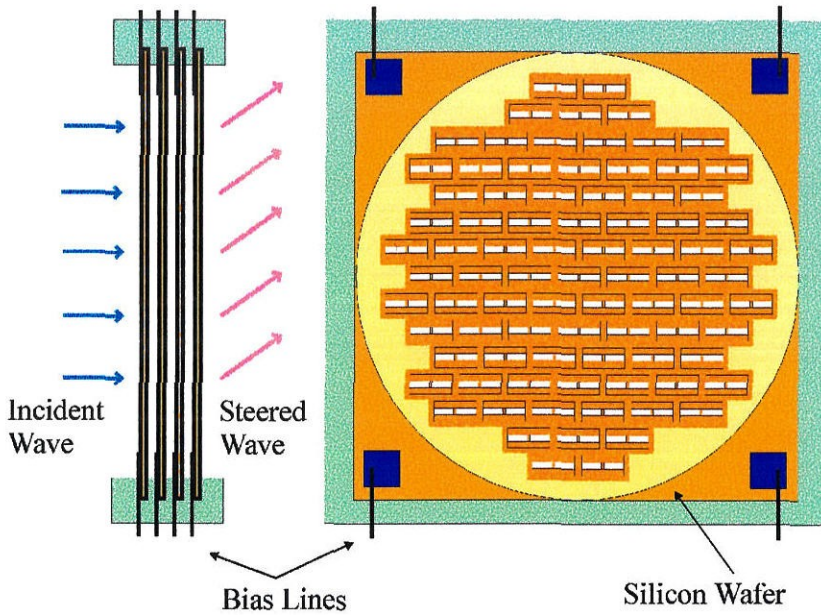
Fig. 4.4. Transmission-type beam steering approach.The incident wave from the left, after passing through layers of switches and waveguides reradiates from the right into free-space. The free-space electrical lenghts and the switch settings are chosen to maximize the transmittance coefficient. The bias lines control the voltage contact.

4.3. 94 GHz Design

4.3.1 Pyramidal Structure

The unit-cell waveguide method is used to simulate the incidence of a TEM-wave on the array by Ansoft's HFSS (High Frequency Structure Simulator) [8]. Fig. 4.5 shows the structure without any metal patterns on it. The unit cell has electric walls on the top and the bottom, and magnetic walls on the sides. Port 1 and 2 are the front and back side of the grid. The unit cell is further reduced by symmetry to a quarter-piece that allows a higher-speed simulation of a simpler structure. The design goal is to minimize the reflection loss by adjusting the
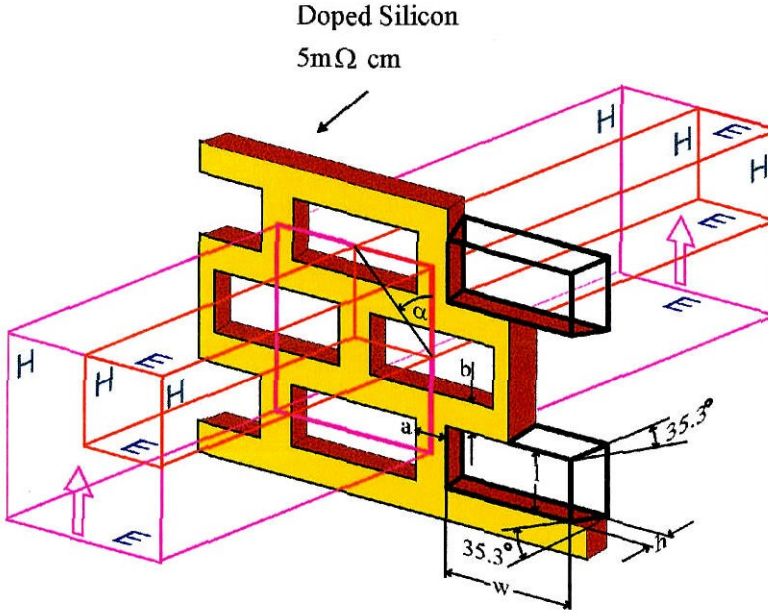
Fig. 4.5. Unit-cell waveguide simulation. The quarter unit-cell greatly decreases the complexity of the simulation. The silicon wafer is 5.5 mils thick and has a low resistivity of $\rho_{Si} = 5m\Omega$ cm.

waveguide dimensions, the thickness of the wafer and the spacings.

The first structure attempted is based on the Ph.D. thesis of Jung-Chih Chiao [9]. The design proposed by Ken-Ichiro Natsume [10] at the California Institute of Technology, is an equilateral-triangular-lattice array of rectangular windows with $l = 1.15$ mm ($0.36\lambda_o$), $w = 2.42$ mm ($0.76\ \lambda_o$), $a = 230$ mm ($0.072\lambda_o$), $b = 0.28$ mm ($0.88\lambda_o$), and $\alpha = 42.8$o. The thickness of the wafer is 140 μm (5.5 mil), where λ_o is the free-space wavelength at 94 GHz. Fig. 4.6 shows (a) the reflection and transmission coefficients, s_{11} and s_{21}, and (b) the reflectance and transmittance as a function of frequency. The structure without any reactive elements has a resonant frequency at 94 GHz.

To simulate the open switches capacitive metal strips are added on the pyramidal holes. Fig 4.7 shows the structure and the unit cell. By changing the gap,

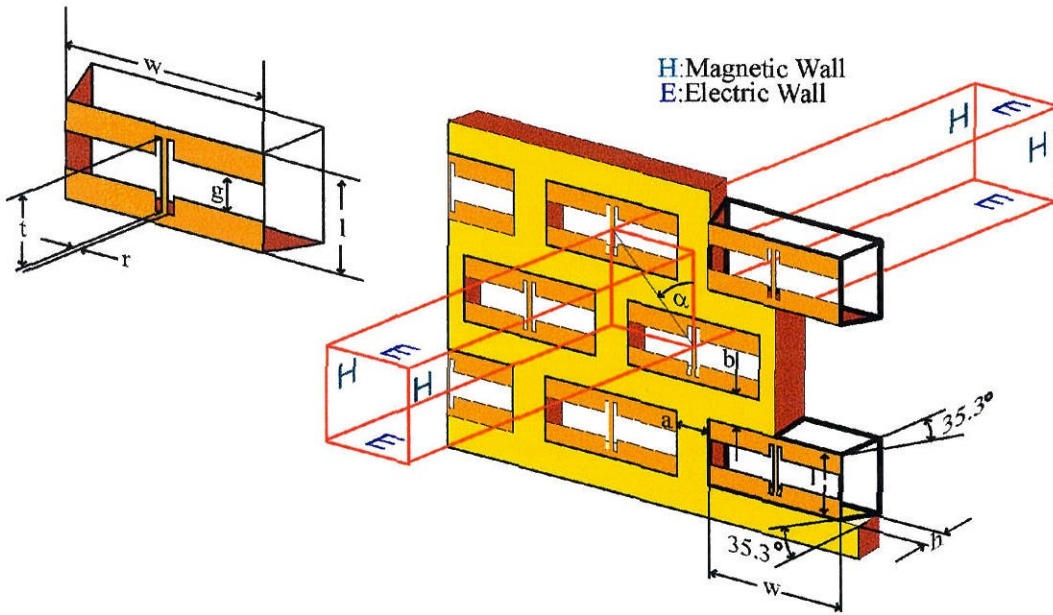(a)   (b)
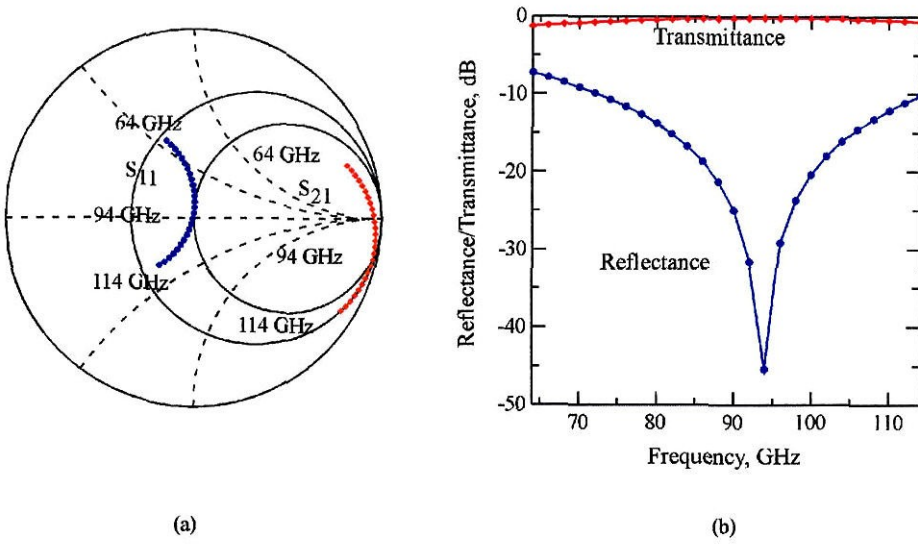
Fig. 4.6 (a) Reflection and transmission coefficients as a function of frequency, and (b) the reflectance and transmittance as a function of frequency.
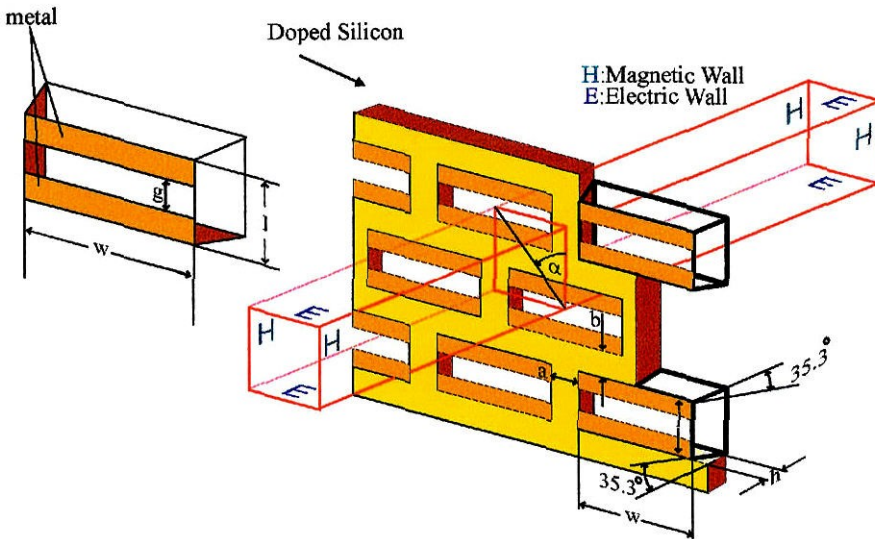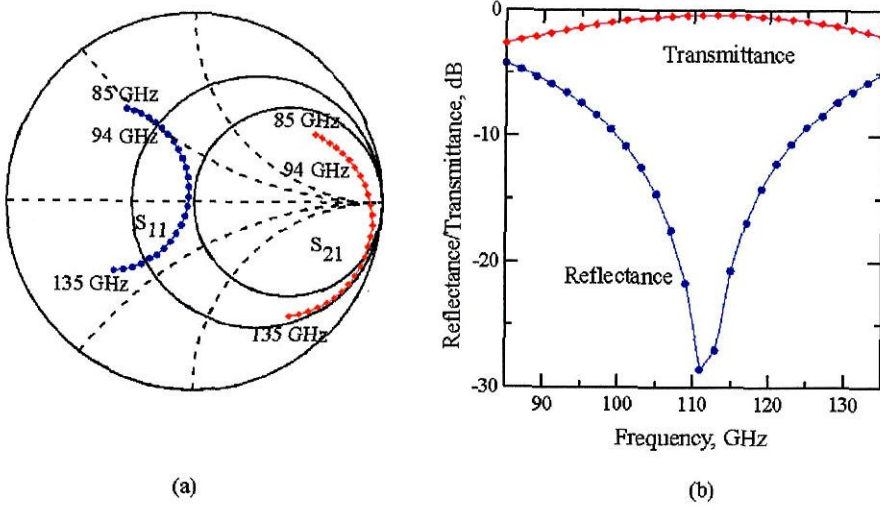

Fig. 4.7 Capacitive array that corresponds to the ON state of the switch. The gap, g adjusts the capacitive reactance.
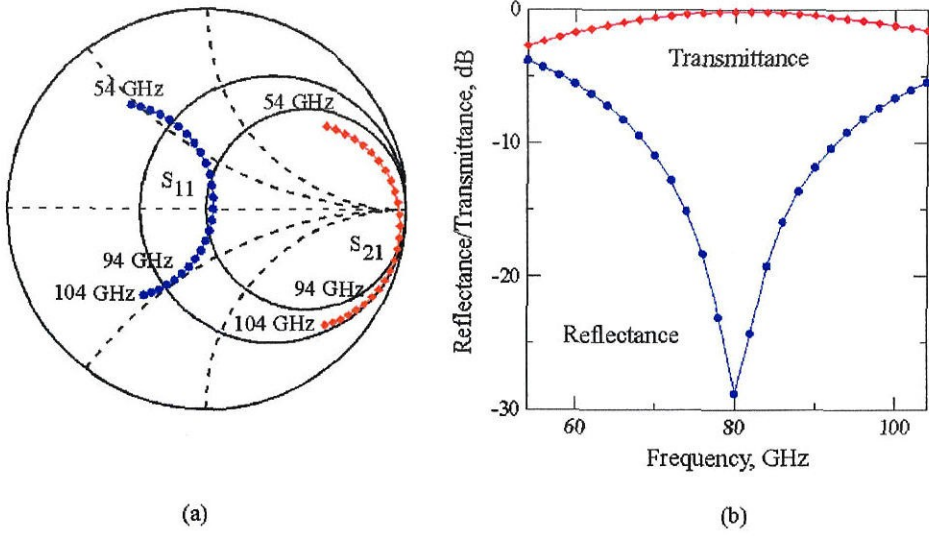
Fig. 4.8 HFSS simulation of the capacitive structure.

Fig. 4.9 Inductive array that corresponds to the ON state of the switch. The height, t and the width, k of the metal strip adjusts the inductive reactance.

Fig. 4.10 HFSS simulation of the inductive structure.

g different shunt capacitances can be obtained. Fig. 4.8 shows the simulation results for a gap, of 0.52mm. Inductive metal strips can be added on the pyramidal holes to simulate the closed switches. Fig. 4.9 shows the inductive array. By changing the width, k and the height, t of the strip different inductances can be achieved. Fig. 4.10 shows the results of the HFSS simulation for $k = 9.4\mu\,$m, $t = 0.91\,$mm and $r = 9.4\mu\,$m.

4.3.2 STRAIGHT-WALL STRUCTURE

The pyramidal holes were first suggested because the etching of silicon results in tilted sidewalls. The exact fabrication process and the problems encountered will be discussed later in detail. A new structure with vertical sidewalls is suggested. The thickness of the wafer is $h = 10mils$ and its resistivity is $\rho_{Si} = 5m\Omega\,$cm.
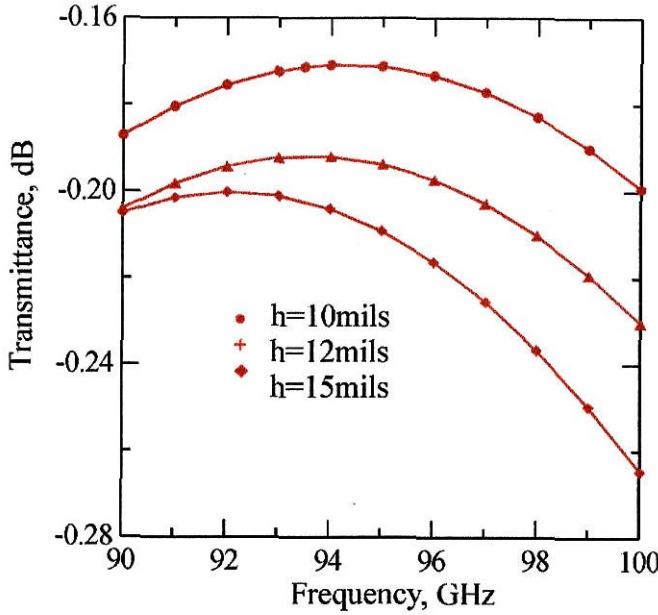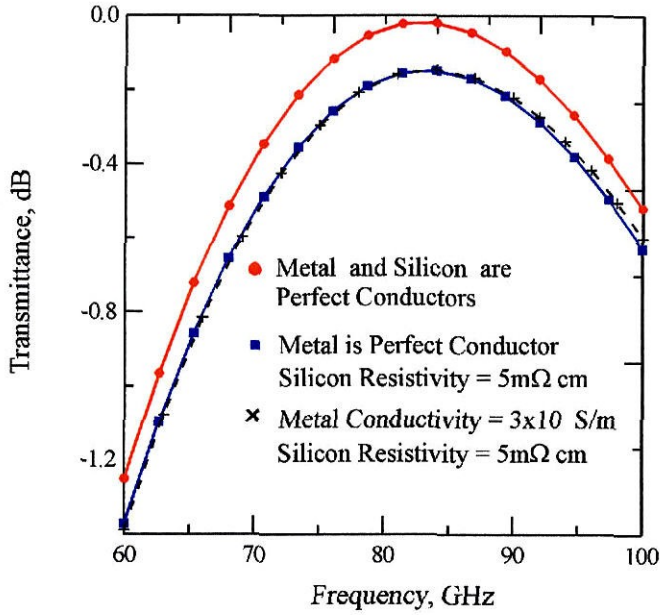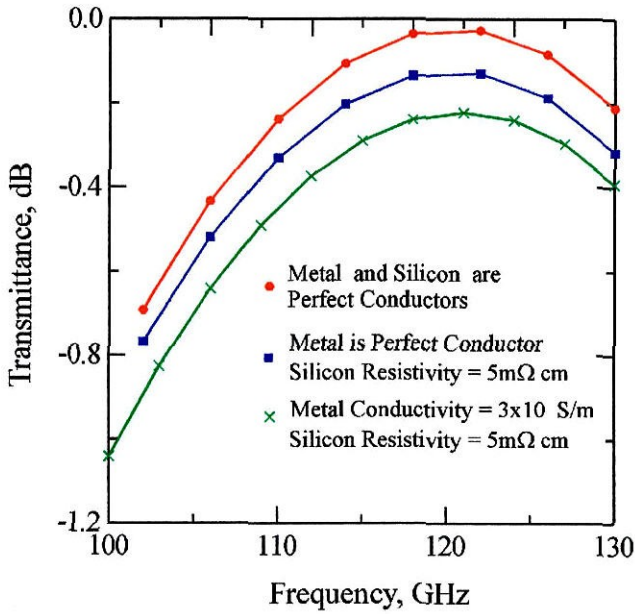
Fig. 4.11 HFSS simulation of an array of rectangular straight-wall waveguides. The simulations are carried out for 3 different thicknesses, $h = 10$mils, $h = 12$mils, and $h = 15$mils. The resistivity of the wafer is $\rho_{Si} = 5 m\Omega$ cm.

Lower resistivity is important because in this new structure the metalization of the sloped sidewalls is ommitted. Fig. 4.11 shows the calculated transmittances as a function of frequency of the low resistivity silicon wafers for different thicknesses. A 10-mils-thickness results only in 0.1 dB loss. Fig. 4.12 and fig. 4.13 show the simulation results for the structures with the added capacitive and inductive strips. In the simulations the finite conductivity of the gold, $\sigma_{Au} = 3 \times 10^7$ S/m is also taken into account.
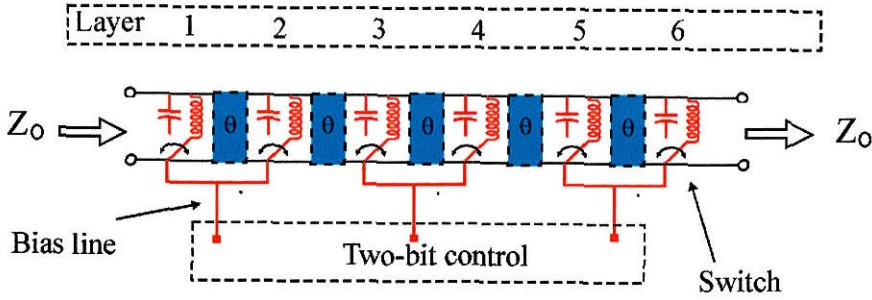
Fig. 4.12 HFSS simulation of a capacitive rectangular straight-wall array The wafer thickness is, $h = 10$ mils, and its resistivity is $\rho_{Si} = 5m\Omega$ cm.

Fig. 4.13 HFSS simulation of an inductive rectangular straight-wall array The wafer thickness is, $h = 10$ mils, and its resistivity is $\rho_{Si} = 5m\Omega$ cm.

**Fig. 4.14** Circuit model for a 6-layer 2-bit controlled beam steering grid.

It is expected that the finite gold conductivity will lower the transmittance of the inductive structure for a vertically polarized electric field because it induces RF currents on the strip. The finite conductivity of the metal pattern does not affect the capacitive array.

The design parameters are: $w = 2.42$ mm $(0.759\lambda_o)$, $l = 1.15$ mm $(0.36\lambda_o)$, $b = 0.15$ mm $(0.047\lambda_o)$, $a = 0.23$ mm $(0.0721\lambda_o)$, $g = 0.55$ mm,$(0.172\lambda_o)$, $r = 0.014$ mm $(0.0044\lambda_o)$, $t = 1$ mm $(0.313\lambda_o)$, $k = 10\mu$m.

4.3.3 CALCULATED PERFORMANCE

One layer of microswitches provides a binary phase shift. By stacking two layers together and adjusting the free-space electrical lenghts between them, minimum loss and optimal phase-shift resolution are achieved. A 6-layer system with proper spacings could provide phase shifts with a 90° resolution over 360° by a 2-bit control signal. Fig. 4.14 shows the approach. One layer includes a switch and a free-space electrical length, θ.

Simulations of a single layer and a two-layer configuration are carried out using HFSS. Fig. 4.15 shows the comparison between the transmission line theory for a pair and the finite-element (HFSS) theory for a pair. In the latter case the
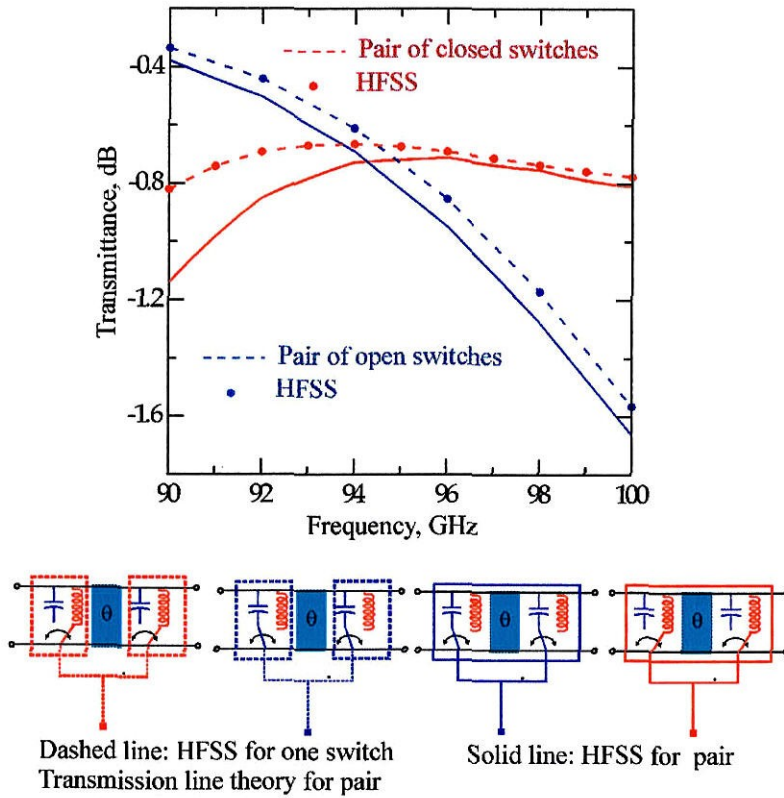
Fig. 4.15 Comparison of transmission line theory for one switch pair and HFSS.

evanescent modes coupled to the waveguide are also taken into account. Fig. 4.16

shows the transmission coefficient on a polar plot. The dashed lines indicate

	90 GHz	90 GHz	94 GHz	94 GHz	98 GHz	98 GHz
target	loss, dB	phase shift	loss, dB	phase shift	loss, dB	phase shift
0°	-1.12	0°	-0.76	0°	-0.86	0°
90°	-1.22	$-0.8°$	-1.56	6°	-2.24	$-8.4°$
180°	-2.36	0.3°	-3.2	$-8°$	-3.5	4.4°
270°	-2.36	0.2°	-3.4	7.3°	-2.44	$-5.2°$

Table 4.1. The phase-shifts and losses of a 6-layer, 2-bit controlled beam steering grid at 90 GHz, 94 GHz, 98 GHz.
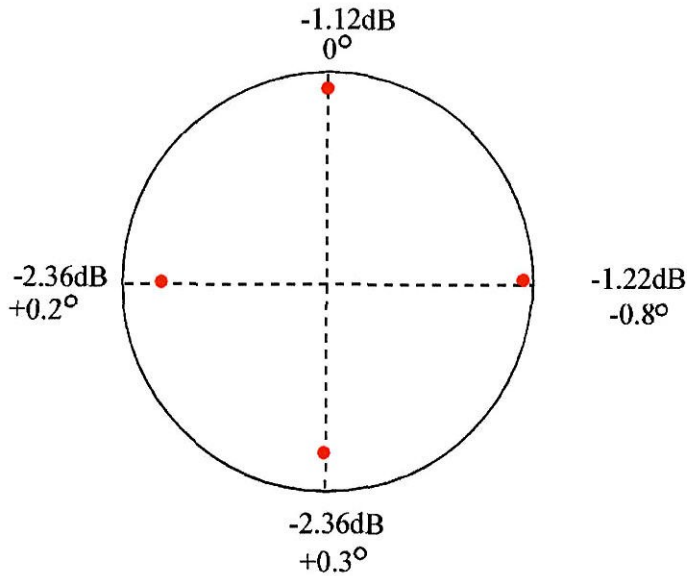
Fig. 4.16 Phase-shifts and losses at 94 GHz for a 6-layer system.

the desired phase-shift resolution (90° over 360°) and the distances from the outer 0 dB-circle to the markers indicate losses. RF conduction losses are also taken into account by assuming a finite conductivity for the metal paterns. The maximum phase shift error is 1° and the maximum loss is 2.36 dB. Table 4.1 reports the maximum losses and phase shift errors when there is a shift in the center frequency as expected very often due to the Doppler effect.

4.4. 35 GHZ DESIGN

Beam controlling grids would have many important systems applications in the frequency ranges from 30 to 130 GHz. These include military as well as civilian applications such as missile seekers, ground-or ship-based radars for aircraft-guiding, automotive collision avoidance, imaging cameras for low visibility environments.
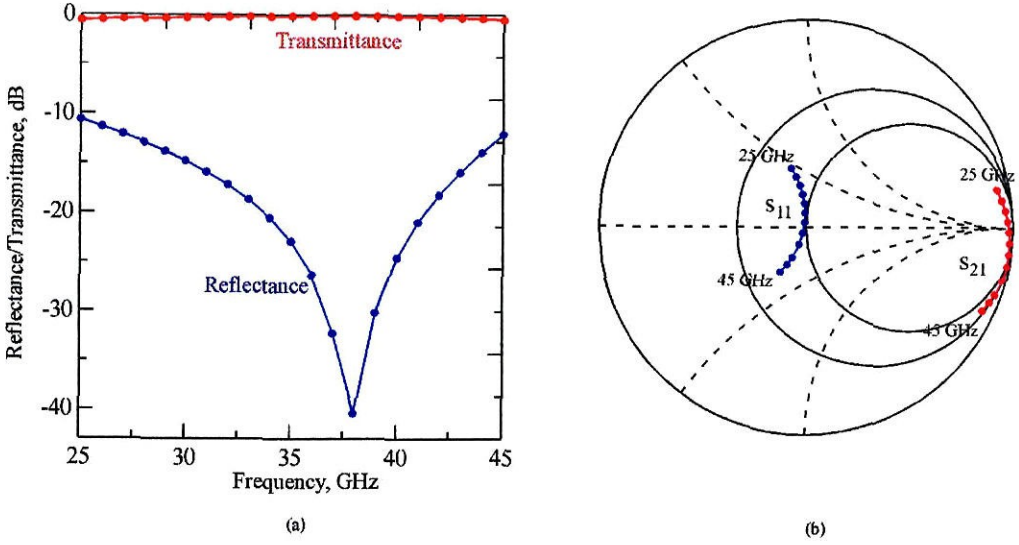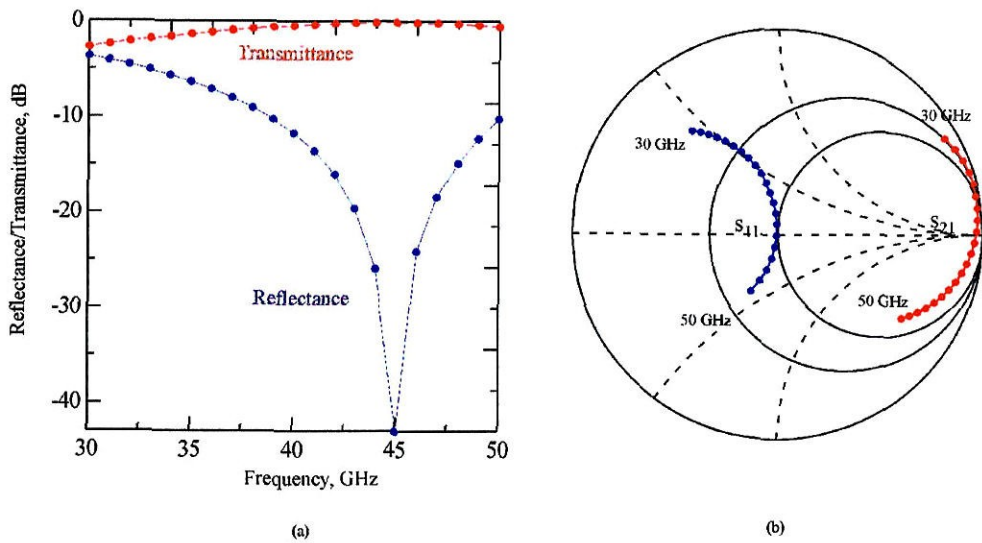
Fig. 4.17 Open-hole waveguide. (a) The reflectance and transmittance as a function of frequency and (b) s_{11} and s_{21}, plotted on a Smith Chart.

Based on the 94 GHz quasi-optical grid phase shifter, a new design for a 35 GHz grid is completed. This is done by scaling down the dimensions of the capacitive and inductive passive structure. This enables the grid to operate at lower frequencies. The dimensions are further tuned to minimize the reflection losses for a pair of switches. For a 90°resolution a stack of three pairs of switches is required. Free space is used to provide proper electrical lengths between the switches. The electrical lengths are adjusted to minimize the loss and to optimize the phase-shift resolution. As discussed in section 4.3, the unit-cell waveguide method is used for HFSS simulations. First, an array without any metal pattern is simulated to minimize the reflection loss. Then capacitive and inductive patterns are added on the surface to imitate the OFF/ON state of the switch respectively. The final design has the following parameters: $w = 6.5$ mm $(0.759\lambda_o)$, $l = 3.1$ mm $(0.36\lambda_o)$, $b = 0.4$ mm $(0.047\lambda_o)$, $a = 0.62$ mm $(0.0721\lambda_o)$, $g = 1.44$ mm, $(0.168\lambda_o)$, $r = 0.06$ mm $(0.007\lambda_o)$, $t = 2.7$ mm $(0.315\lambda_o)$, $k = 0.02$ mm.
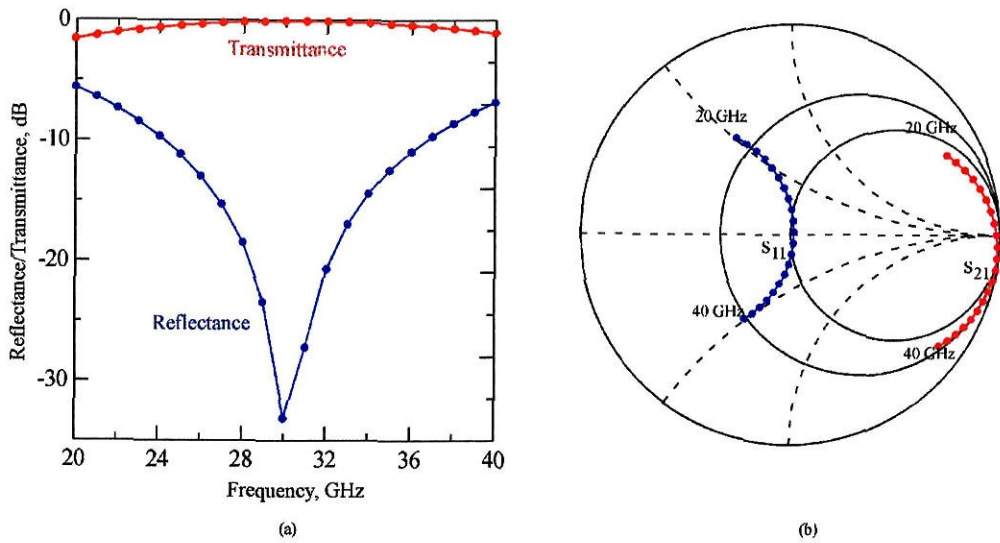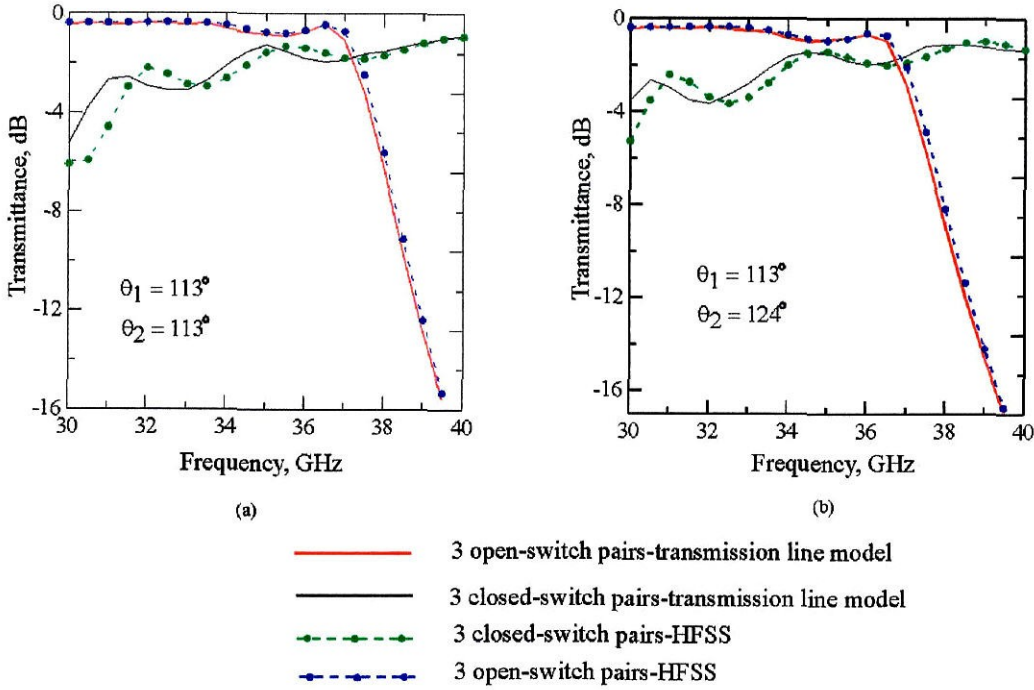
Fig. 4.18 Capacitive grid. (a) The reflectance and transmittance as a function of frequency and (b) s_{11} and s_{21}, plotted on a Smith Chart.

Fig. 4.19 Inductive grid. (a) The reflectance and transmittance as a function of frequency and (b) s_{11} and s_{21}, plotted on a Smith Chart.

Fig. 4.17 shows (a) the reflectance and transmittance and (b) the *s*- parameters plotted on a Smith Chart from 25 GHz to 45 GHz for the waveguide-cell *without metal patterns*. The waveguide is small enough so that only one mode propagates. The resonant frequency is 37 GHz.
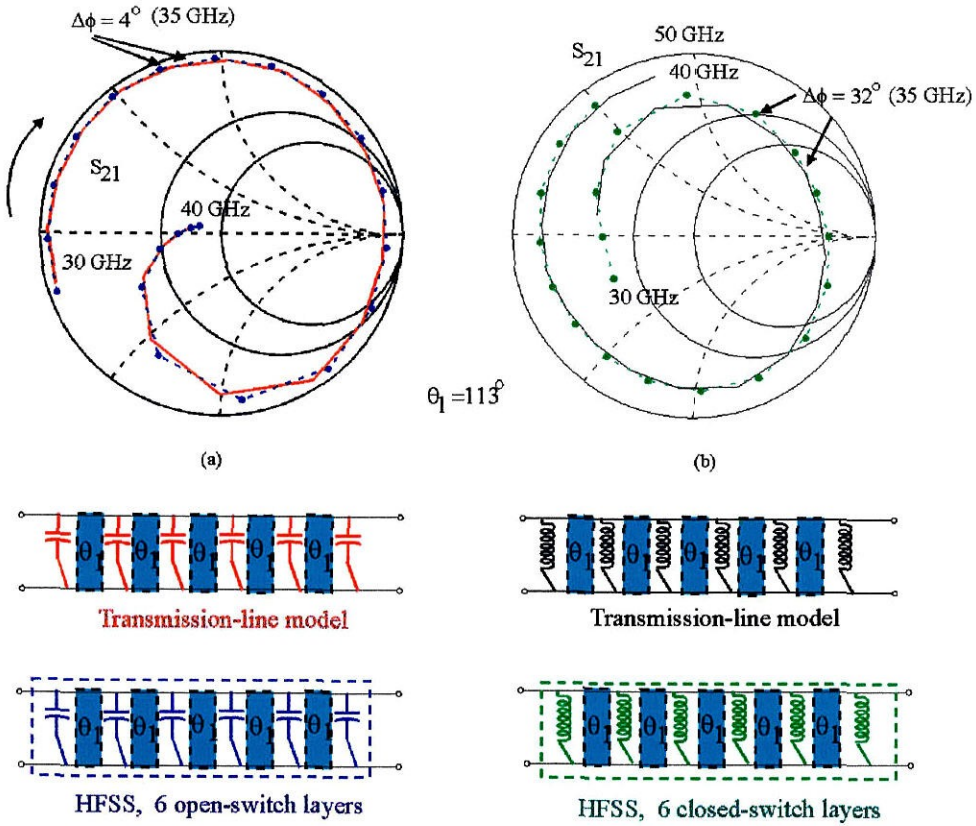
Fig.4.18 shows (a) the reflectance and transmittance and (b) the *s*- parameters from 20 GHz to 40 GHz for the capacitive grid. Fig. 4.19 shows (a) the reflectance and transmittance from 30 GHz to 50 GHz for the inductive grid.

———	3 open-switch pairs-transmission line model
———	3 closed-switch pairs-transmission line model
--•--•--	3 closed-switch pairs-HFSS
--•--•--	3 open-switch pairs-HFSS

Fig. 4.20 (a) The transmittance as a function of frequency for a 6-layer capacitive and inductive grid when all free-space layers are equal to $\theta = 113°$ and (b) when the last two layers are equal to $\theta = 124°$.

A transmission line equivalent circuit model for a 6-layer 2-bit controlled beam steering grid was proposed in section 4.3. This model does not take into account the coupling effect of evanescent waves that are induced by an incident wave on the layers. A 6-layer quarter-piece unit-cell waveguide with capacitive and inductive metal patterns was simulated, using HFSS. The free-space electrical length between the layers is $\theta = 113°$.

(a)

(b)

Transmission-line model

Transmission-line model
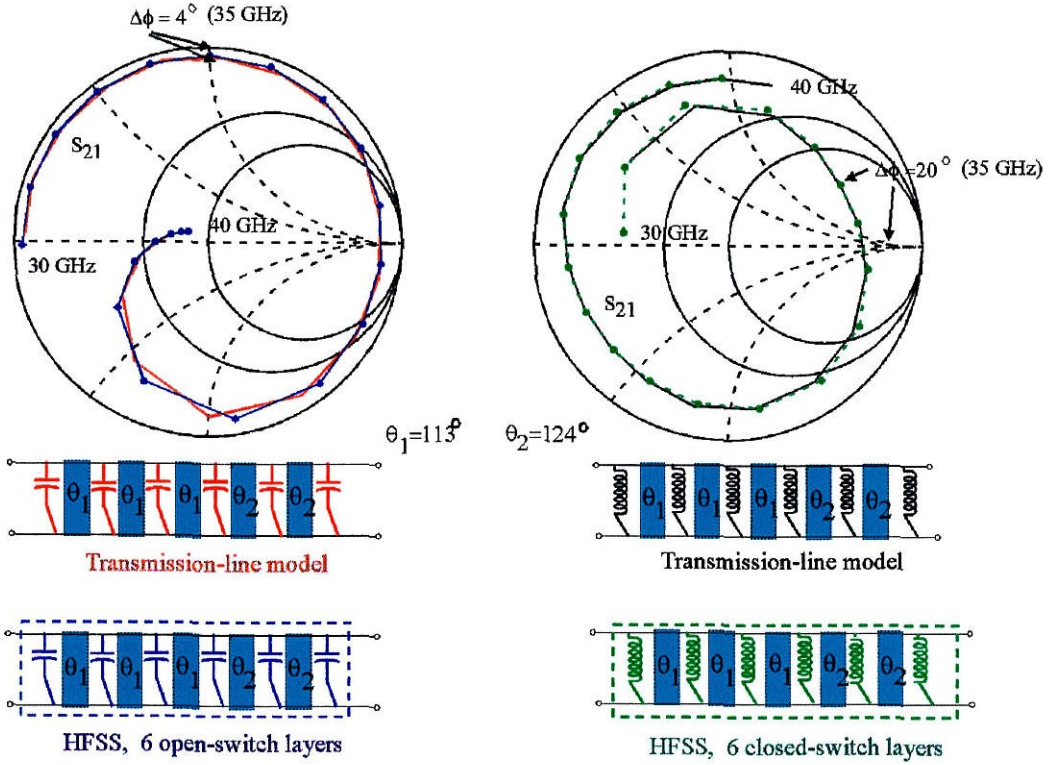
HFSS, 6 open-switch layers

HFSS, 6 closed-switch layers

Fig. 4.21 Transmission coefficient plotted on a Smith Chart when all free space layers are equal to $\theta = 113°$ (a) for a 6-layer capacitive grid and (b) for a 6-layer inductive grid.

Fig. 4.21 compares the s_{21} calculated from the transmission line model and from the HFSS of the whole structure for both the open and closed switches.

There is a phase delay, $\Delta\phi = 32°$ in the transmission coefficient for the 6-layer inductive structure. The phase delay for the 6-layer capacitive grid is only,

$\Delta\phi$=5°. The transmittance does not change significantly as seen in fig. 4.21. This is due to the strong attenuation of the evanescent waves. By setting the free-space electrical length of the last two layers to $\theta = 124°$ the phase delay for the 6-layer inductive structure is reduced to $\Delta\phi$=20°. The phase delay for the 6-layer capacitive structure as well as the transmittance is not affected by this change (Fig. 4.21 and Fig. 4.22 (a)).

**Fig. 4.22** Transmission coefficient plotted on a Smith Chart when the last two free space layers are equal to $\theta = 124°$ (a) for a 6-layer capacitive grid and (b) for a 6-layer inductive grid.

Based on the these simulations the calculated performance for the beam steering grid is shown in Fig. 4.23 The maximum phase shift error is 9° and the maximum loss is 2 dB. RF conduction losses are already taken into account

because the finite conductivity for the gold ($\sigma_{Au} = 3 \times 10^7$ S/m)is incorporated in the HFSS. By adding more layers in the structure a higher phase-shift resolution could be obtained.

It is shown in Fig. 4.21 and Fig. 4.22 that the inductive structure has stronger evanescent-wave coupling effect than the capacitive ones.
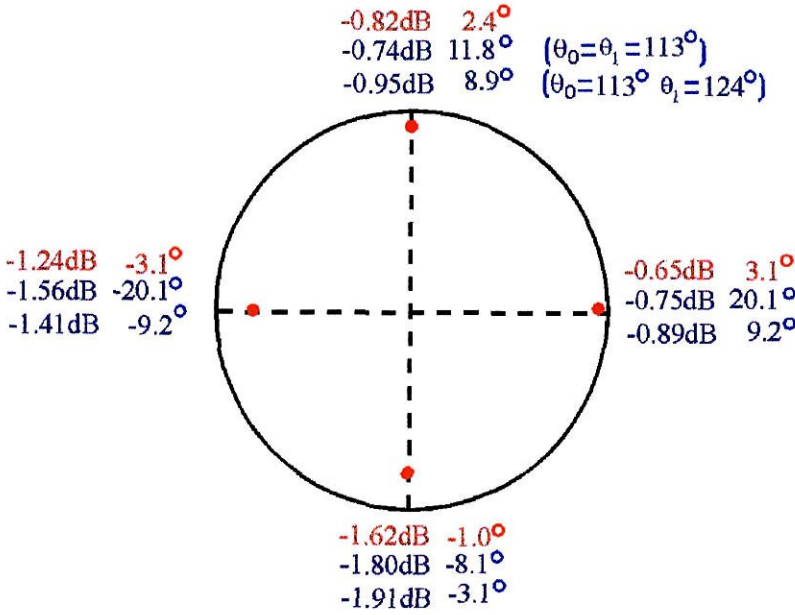
Fig. 4.23 Phase-shifts and losses at 94 GHz for a 6-layer system.

4.5. FABRICATION PROCEDURES

4.5.1. WET SUBSTRATE ETCH WITH DIELECTRIC MEMBRANE

The first attempt to fabricate the microrelays involved a low-temperature ($< 200°$ C) process developed at the Rockwell Science Center, and it was carried out by Dr. Rob Michailovich. The substrate used is a low-resistivity, highly-

doped, double-side polished silicon wafer. Low resistivity is important because it reduces the RF losses and because the metalization of the sloped silicon sidewalls after the etching of the substrate proved very difficult. First a $0.2\,\mu$m-thick membrane film stack (LPCVD Si_3N_4) is deposited on the substrate silicon, covering both the front and back side. This film serves as a mask to define the opening for the wet-etching of the silicon.
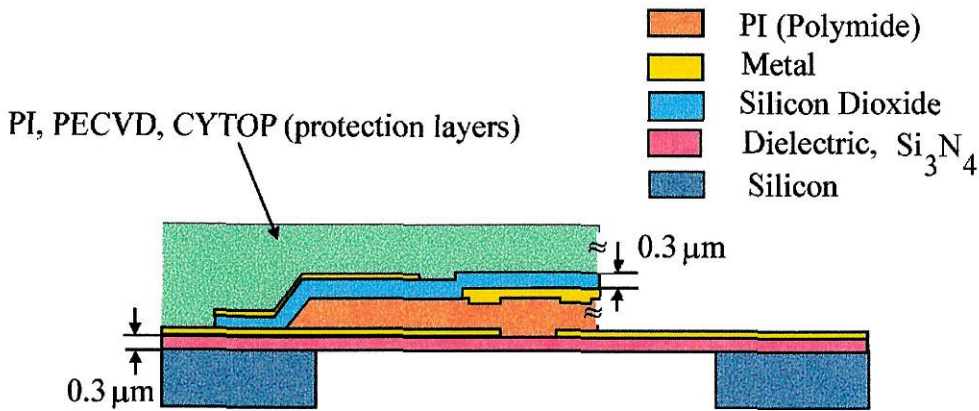
Fig. 4.24 Different layers deposited on the wafer during the fabrication.

Atop the frontside of the Si_3N_4 layer, a $0.2\,\mu$m-thick PECVD SiO_2 film is deposited. This layer prevents the DC bias currents from flowing through the contact that would result in taking away the charges formed to actuate electrostatically the motion of the switch. It also adds mechanical rigidity and helps the adhesion of the subsequent thin-film materials. The following step involves the formation of the metal pattern. Areas without metal are covered with a Polyimide (PI) sacrificial layer. Atop the PI/metal layers a $0.2\,\mu$m-thick PECVD oxide is deposited, patterned and etched to define the movable switch. The next and most challenging step is how to protect the frontside switch device during backside aperture etching and how to remove this protection after the

etching of the substrate. The protection layer must withstand the wet-chemical etching that uses KOH and TMAH (tetramethylammonium hydroxide) solutions. Other requirements for the protection layer are: coverage over 7μ m steps and low temperature process ($< 200°$ C).
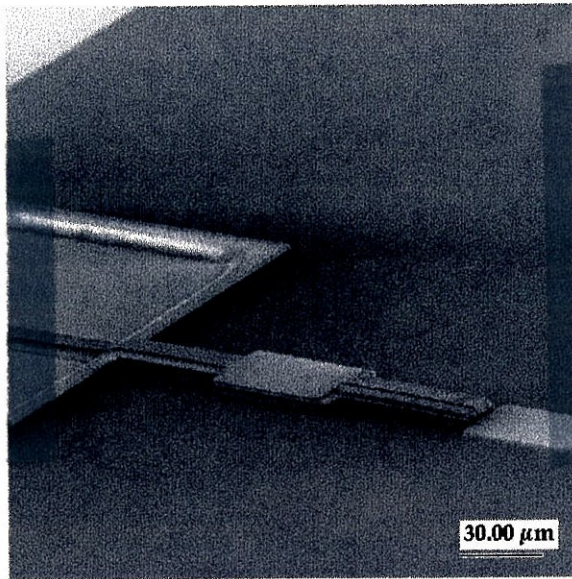

Fig. 4.25 Damaged and stuck switch after the wet-etch process.

The first approach used Polyimide that can only be removed in a dry-etch process so the structure could not be exposed to any chemicals. Second, PECVD oxide was used as a protection layer but it did not resist to the Silicon etchant. The device was attacked either from the edges or through pinholes. Third, spun-on organic CYTOP was used that provided protection from the KOH solution but it was impossible to remove. At last, a mechanical O-ring seal was attempted but the wafer was too thin and fragile and broke easily. Fig. 4.24 shows the different layers deposited during the wet-etch process. The switch could not be released with this process. Fig. 4.25 shows a photograph of a stuck and damaged switch as a result of this wet-etch process. Passive structure were realized but the organic CYTOP layer could not be removed.

4.5.2. Dry Substrate Etch with Dielectric Membrane

The wet-etch approach was put aside with the delivery of ICP (Inductive Coupled Plasma etcher). The expected benefits from this etch is that it does not require very thin wafers and it needs minimal frontside protection.
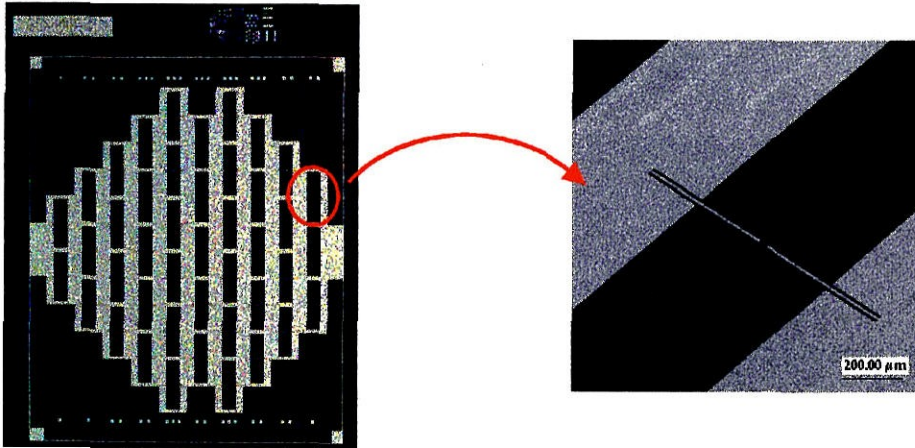

Fig. 4.26 Photograph of a passive capacitive structure.

The ICP fabrication technique uses a thicker, (10 mils) highly doped silicon wafer and LPCVD Si_3N_4 membrane. The whole wafer is flipped and mounted. The silicon is then etched with the ICP etcher. This process demonstrated fast etch rates (6-10 mil/hr) as opposed to the wet etch technique that was considerably slower (0.5 mil/hr). It is also moderately selective (50-75:1) and the perimeter etches faster by approximately 20. Significant undercutting of the sidewalls is also observed. Initial ICP etching resulted in wrinkling and thinning membranes most probably due to a change in stress caused by thermal cycles, non-uniformity and moderate etch selectivity. Further studies have been made to determine a process for flat membranes, using dry-etch substrate removal. A maskset with sized apertures and different membranes compositions was fabri-

cated and etched. The ICP etching of this wafer showed wrinkling for larger apertures and for all membrane compositions.
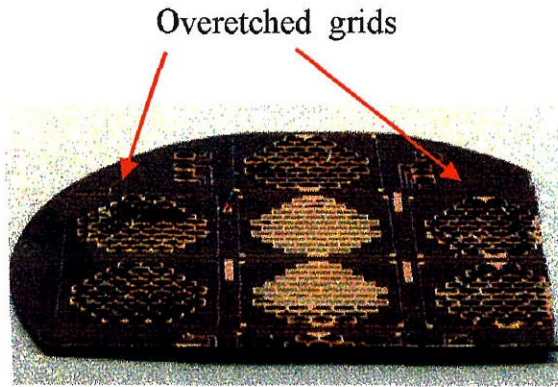
Fig. 4.27 Silicon wafer with two good passive structure.

Fig. 4.26 shows the frontside of the passive array. Passive structures are realized with no overetch, and Fig. 4.27 shows a silicon wafer with two good passive structures. The perimeter is overetched and damaged.

4.5.3. DRY SUBSTRATE ETCH WITH SILICON MEMBRANE

The previous technique severely deformed the membranes. The damage was either mechanical due to the Reactive Ion Etching (RIE) process or the change of properties of the film due to the thermal cycles of the fabrication. Obviously the wrinkling observed is very sensitive to overetching and it follows a ring pattern where the outside etches faster. A new approach is developed that uses silicon-on-insulation silicon wafer. The SOI wafer can have any thickness, doping orientation and the insulator is SiO2 and has a thickness of few microns. The membrane is formed by silicon and SiO_2 or silicon and can have arbitrary thickness. Fig. 4.28 shows the SOI etched substrate without the switch and Fig. 4.29 illustrates the cross-section of an etched wafer. This is the most promising technology for the fabrication of the microswitches on membranes.
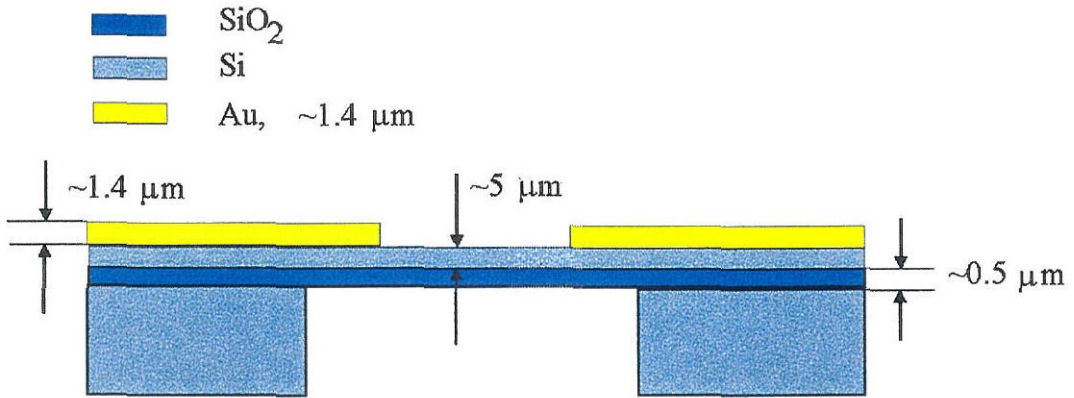
Fig. 4.28 Cross section of an etched Silicon-on-Oxide wafer.
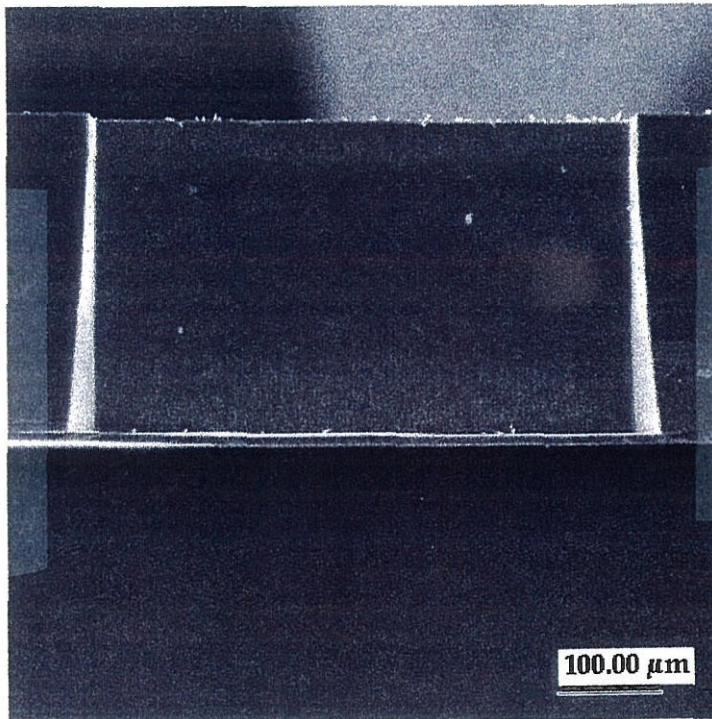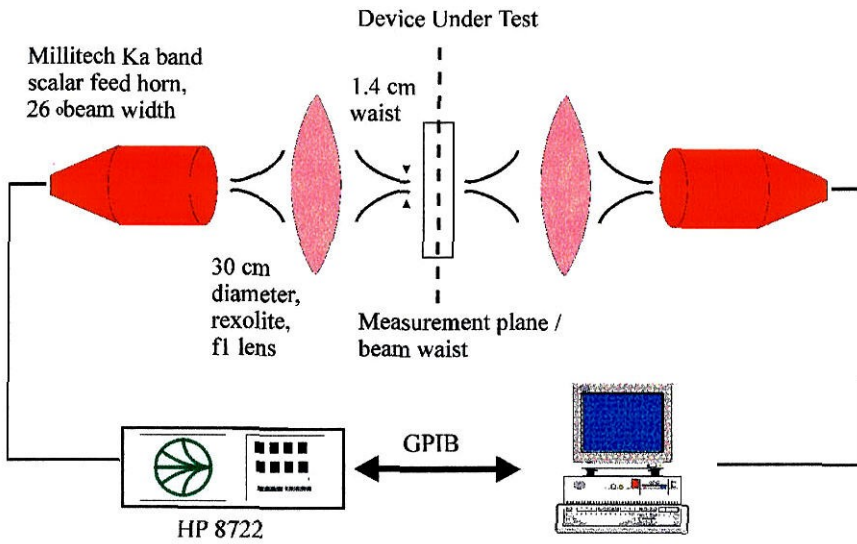

**Fig. 4.29** Photograph of the cross section of an etched Silicon-on-Oxide wafer.

4.6. MEASUREMENTS

The focused Gaussian beam set-up described in chapter 2 is used for the measurements of the transmittance of the passive capacitive grids. The schematic diagram of the measurement set-up is given in Fig. 4.30.


Fig. 4.30 Gaussian beam measurement set-up.

The technique uses rexolite lenses, with 1 ft focal distance to focus a highly Gaussian beam onto the array under test. The transmit and receive antennas are Millitech corrugated conical antennas. The size and location of the beam waist are determined using equations (2-1) and (2-2). For the Millitech horns, $a = 4.76$ mm, $w = 0.644a$ and $\alpha = 7.5°$. Using these numbers in (2-1) and (2-2) gives a beam waist of radius 3 mm at a distance of 38.8 mm from the aperture. A picture of the focused Gaussian beam set-up is shown in Fig. 4.33. To verify the accuracy of this measurement technique, a 0.85 mils thick AlN slab of known dielectric constant, $\varepsilon_r = 8.6$, was inserted at the reference plane of the W-Band set-up and measured.
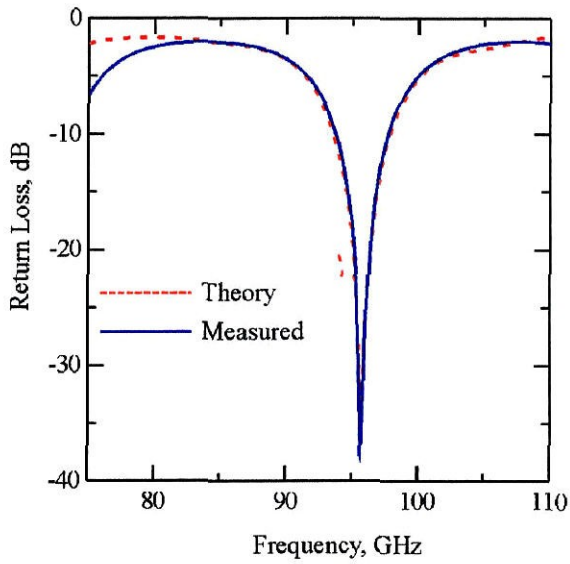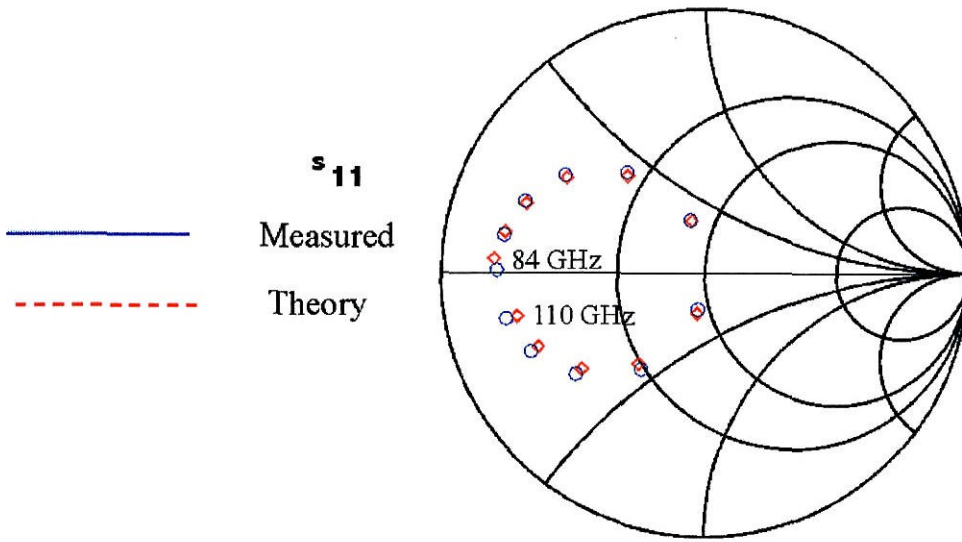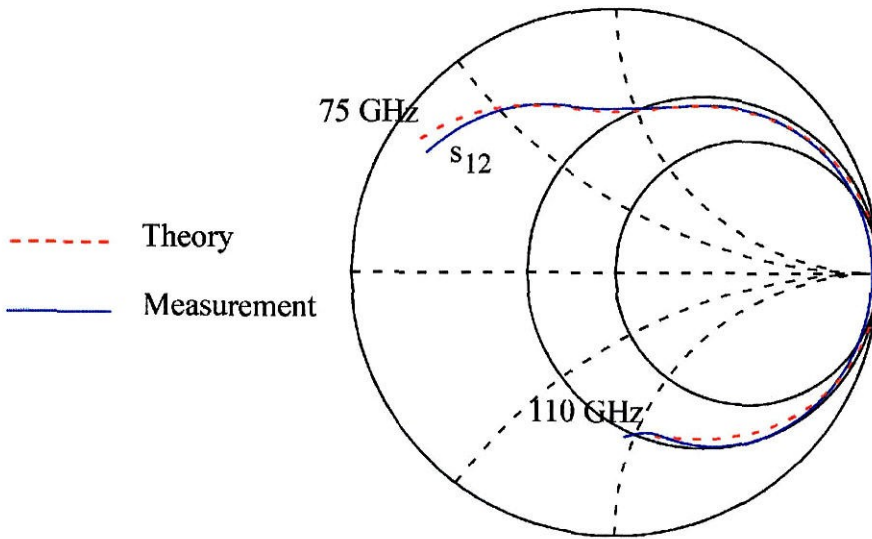
(a)
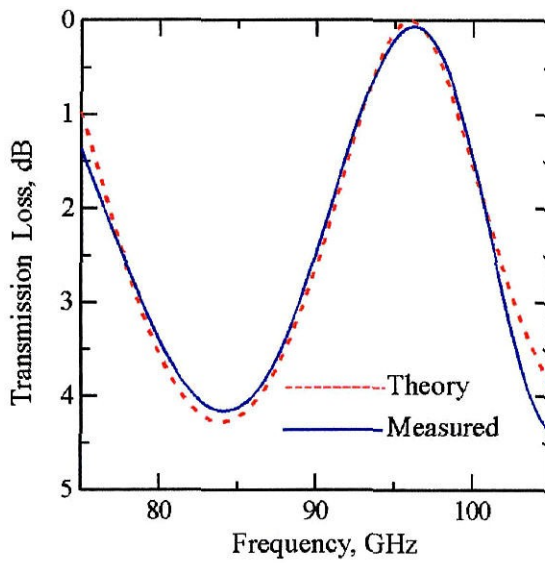
(b)

Fig. 4.31 (a) Reflectance measurement and theory for a 0.85 mils thick AlN slab and (b) Transmittance measurement and theory for the same slab.
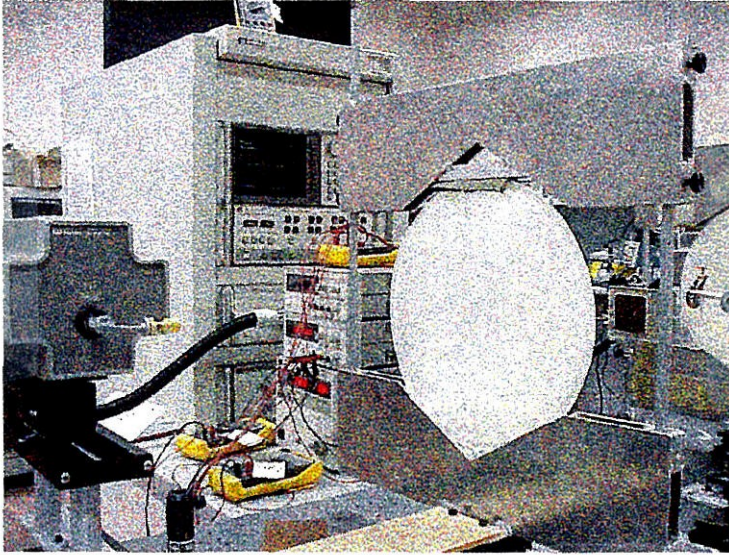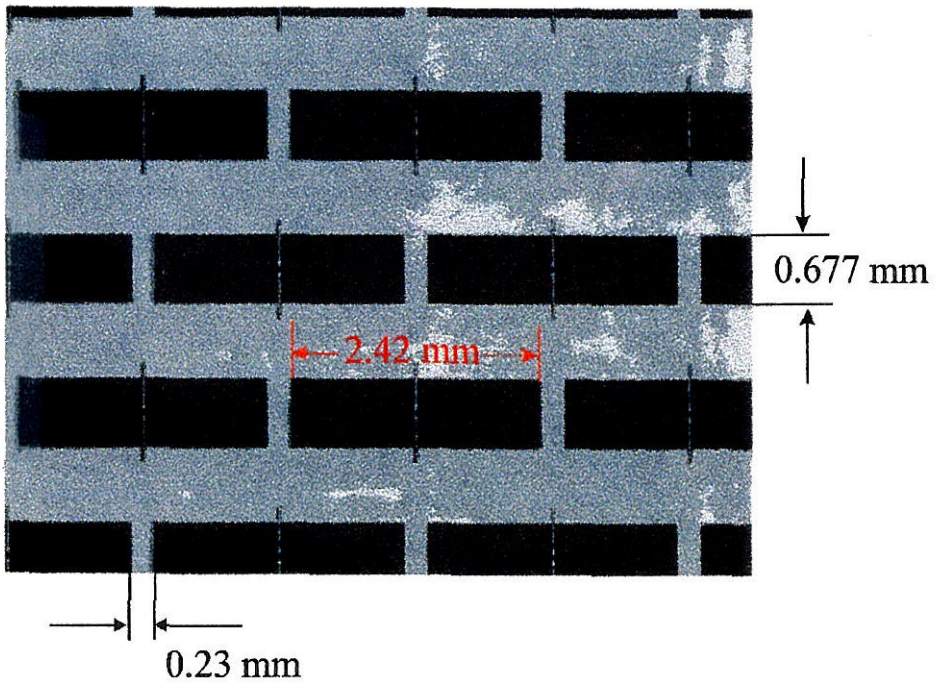
Fig. 4.32 (a) s_{11} measurement and theory for a 0.85 mils thick AlN slab and (b) s_{21} measurement and theory for the same slab.

**Fig. 4.33** Photograph of the measurement set-up.


0.677 mm

2.42 mm

0.23 mm

Fig. 4.34 Photograph of the 94 GHz capacitive grid. The dimensions shown are measured under a microscope.

A comparison between the measured results and theoretical simulations for the magnitude and phase of the transmission and reflection coefficients is shown in Fig 4.31 and fig. 4.32 respectively. Time-domain gating was used to remove a ripple due to multiple reflections between the slab and the antennas. The gating feature of the HP8510 network analyzer is used for implementation of time-domain gating in free-space s-parameter measurements. Information on time-domain gating is given by Rytting [11, 12] and Varadan *et al.* [13, 14]. The transmittance and reflectance of a grid with capacitive metal pattern as shown in Fig. 4.34 were measured to verify the resonant frequency. Fig. 4.35 shows the calculated and measured transmittance.
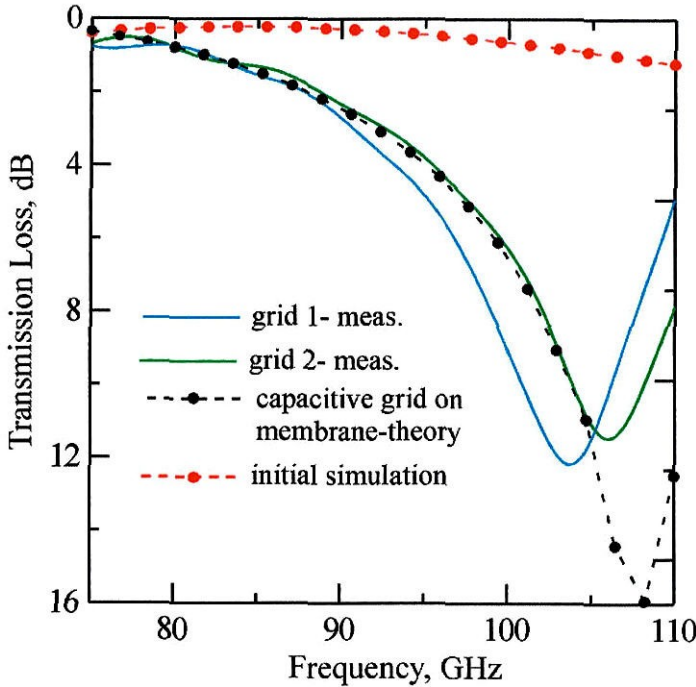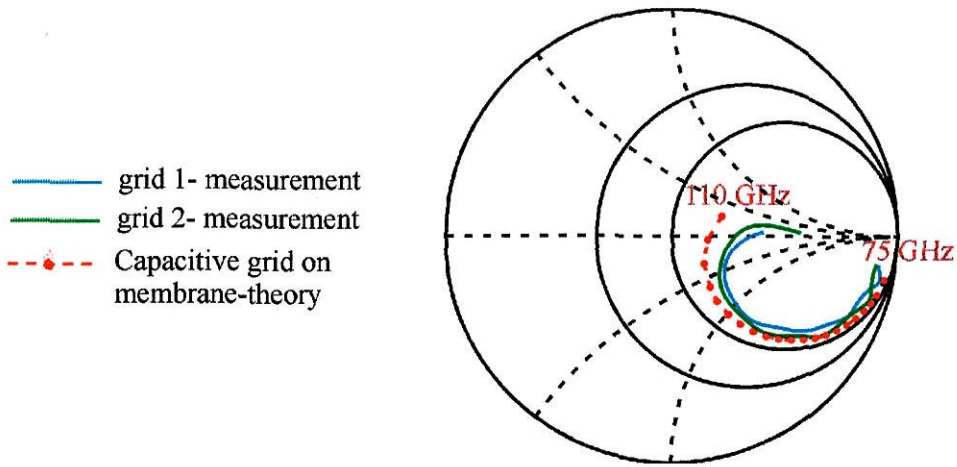

Fig. 4.35 Calculated and measured transmittances of a rectangular-window array with straight walls with capacitive metal patterns, as shown in Fig. 4.34 on the membrane for imitating the open switch.

The red dashed line is the simulation result when the thickness of the dielectric membrane is not taken into account (see also Fig. 4.12). The open vertical strip that imitates the open switch is not included in the simulation. The black solid line includes the thickness of the Si_3N_4 membrane ($\approx 1\,\mu m$) and the thin vertical strip. These two effects shift down the resonance frequency. Both the transmission (Fig. 4.35) and reflection (Fig. 4.36) curves indicate the resonant frequency for the capacitive grid is about 75 GHz. Fig. 4.37 shows the phase information for the calculated and measured transmission coefficient. Agreement is very good. The grid was originally designed to operate at 94 GHz. The measurements indicate that it could operate at a lower frequency.
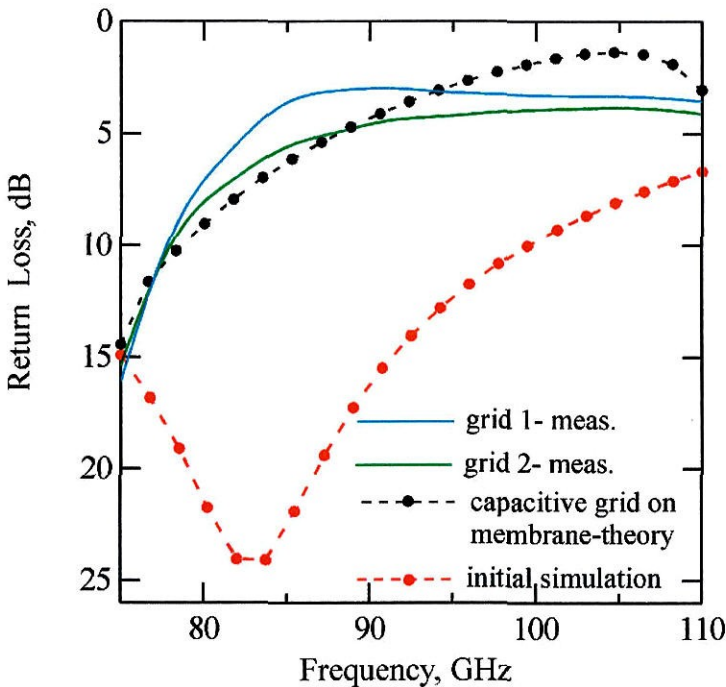
Fig. 4.36 Calculated and measured reflectance of a rectangular-window array with straight walls with capacitive metal patterns, as shown in Fig. 4.34 on the membrane for imitating the open switch.

Fig. 4.37 Calculated and measured s_{21} on a Smith Chart of a rectangular-window array with straight walls with capacitive metal patterns, as shown in Fig. 4.34 on the membrane for imitating the open switch.

References

[1] X.Qin, W.-M.Zhang, C.W.Domier, N.C.Luhmann, Jr., W.Berk, S.Duncan, and D.W. Tu, "Monolithic millimeter-wave beam control array," *IEEE Microwave Theory Tech. Symp. Dig.*, pp. 1669–1672, 1995.

[2] Xiaohui Qin, "Monolithic Millimeter Wave Beam Control Array," *Ph.D. Dissertation*, University of California, Los Angeles, 1995.

[3] D. Choudhury, J.J. Nicholson, R.F. Dec, E.L. Moore, "Development of a monolithic diode beam steering array for concealed weapon detection system," *Digest of the Twentieth International Conference on Infrared and Millimeter Waves*, Dec. pp. 289–290, 1995.

[4] J.Jason Yao, M.Frank Chang "A surface micromachined miniature switch for telecommunications applications with signal frequencies from DC up to 4 GHz," *The 8th International Conference on Solid-State Sensors and Actuators, Stockholm, Sweden*, pp. 384–387, 1995.

[5] A. Gopinath, J.B. Rankin, "GaAs FET RF Switches," *IEEE Trans. on Electron Dev.*, vol. ED-32, pp. 1272–1278, Jul. 1985.

[6] R.H. Caverly, "Distortion in Off-State Arsenide MESFET Switches," *IEEE Trans. On Microwave Theory and Tech.*, vol. 41, pp. 1323–1328, Aug. 1993.

[7] K.W Kobayashi, A.K. Oki, D.K. Umemoto, S.K.Z. Claxton, D.C. Streit, "Monolithic GaAs HBT p-I-n Diode Variable Gain Amplifiers, Attenuators and Switches," *IEEE Trans. On Microwave Theory and Tech.* , vol. 41, pp. 2295–2302, Dec. 1993.

[8] Ansoft Corp. HFSS Version 5.0,

[9] J.-C. Chiao, " Quasi-Optical Components for Millimeter and Submillimeter Waves ," Ph.D. Thesis, California Institute of Technology, Pasadena, CA, 1996.

[10] K.I. Natsume, D.B. Rutledge, Aiden Higgins, Robert Mihailovich, "Microswitch Beam Steering Grids," *Report prepared for the ARO*, June. 1997.

[11] D. Rytting, "Advances in microwave error correction techniques," *Hewlett-Packard, RF and MW Symp.*, pp. 5954–8378, June 1987.

[12] D. Rytting, "Let time domain response provide additional insight into network behaviour," *Hewlett-Packard, RF and MW Symp.*, pp. 5952–6660, Mar. 1985.

[13] D.K. Ghodgaonkar, V.V. Varadan, V.K. Varadan, "Free-space measurements of complex permittivity and complex permeability of magnetic materials at microwave frequencies," *IEEE Trans. Instrum. Meas.*, vol. 39, pp. 387–394, 1990.

[14] D.K. Ghodgaonkar, V.V. Varadan, V.K. Varadan,, "A Free-space method for measurement of dielectric constants and loss tangents at microwave frequencies," *IEEE Trans. Instrum. Meas.*, vol. 38, pp. 789–793, 1989.

Chapter 5

HEMT Grid Oscillator

This chapter discusses the design, construction, and performance of a 36-element hybrid grid oscillator that minimizes substrate-mode excitation. The active devices are InP-based High Electron Mobility Transistors (HEMT's). A locked output frequency spectrum was achieved, with an effective radiated power (ERP) of 200 mW at 43 GHZ. Ferrite slabs were used to suppress spurious bias line oscillations. Measurements show the E and H-plane radiation patterns have side lobes 10 dB below the main beam. These results are a significant improvement over a previous millimeter-wave grid oscillator, which had a divided beam because of substrate modes.

5.1. INTRODUCTION

In order to produce high power at microwave and millimeter-wave frequencies the output powers of many solid-state devices are combined. Quasi-optical free-space power combiners eliminate losses associated with waveguides and transmission lines. Quasi-optical grid oscillators are periodic, strongly coupled, oscillating structures based on integrating active devices directly into a planar array. Fig. 5.1 shows the approach. The grid is fabricated on a dielectric substrate and has a period much smaller than a free-space wavelength. The DC bias is fed along the horizontal leads. The radiating leads run in the vertical direction, and the output beam is vertically polarized.
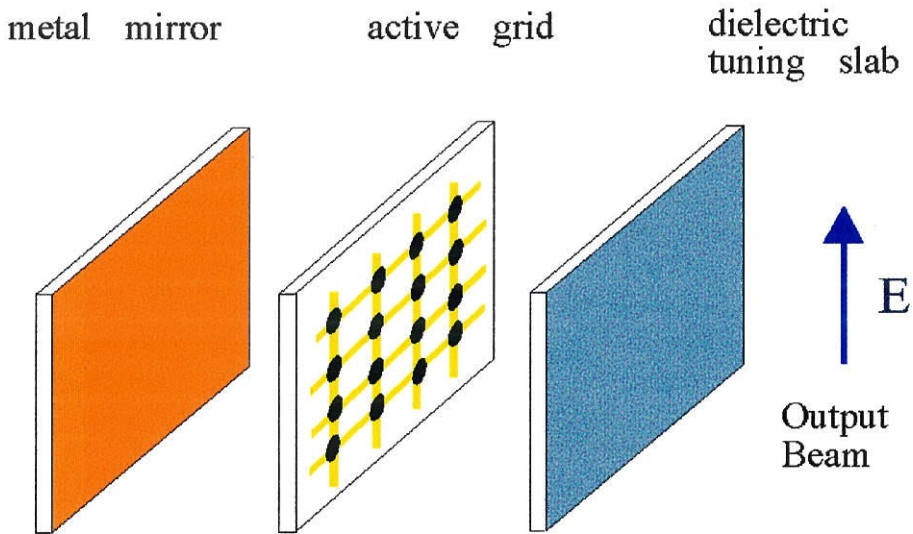
Fig. 5.1. Grid oscillator. The mirror and the dielectric slab provide tuning and help the devices to lock together.
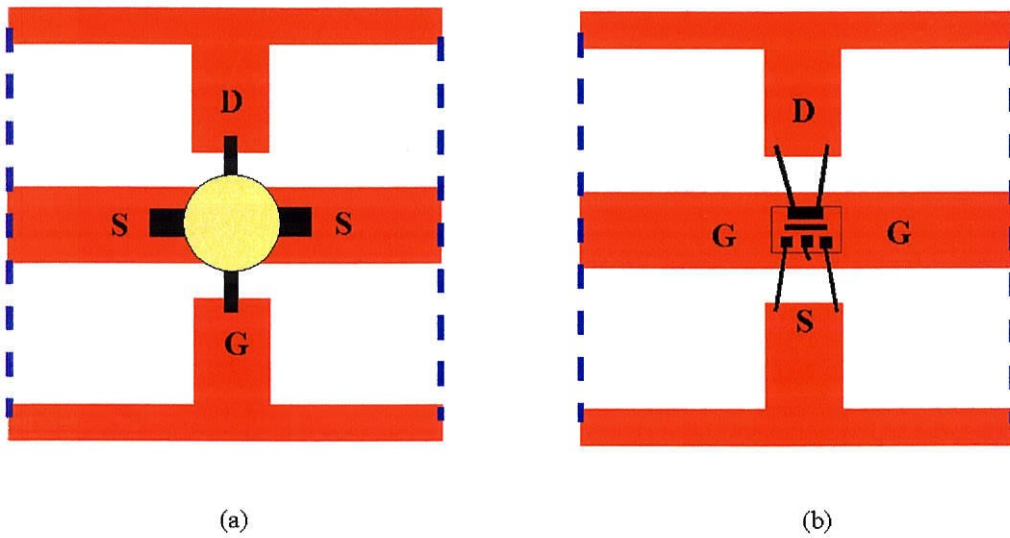
Fig. 5.2. Transistor oscillator grid unit cells: (a) source feedback configuration and (b) gate feedback configuration.

A mirror is placed behind the array and it provides the necessary positive feedback for the oscillation. Sometimes a tuner is placed in front of the grid. The tuner is just a piece of Duroid with high dielectric constant. The first transistor-grid oscillator was a 9.7-GHz 25-MESFET grid that delivered an ERP of 20.7 W at 9.7 GHz [1]. The power radiated from the grid was 474 mW. Popovic *et al.* [2] demonstrated a 5 GHz, 100-MESFET planar grid oscillator that produced an ERP of 22 W with DC-to RF conversion efficiency of 20%. In these grids the gate lead is parallel to the radiated electric field and the source leads are horizontal. This is the source-feedback configuration and the unit cell is shown in Fig. 5.2(a). The gate-feedback approach is shown in Fig. 5.2(b). The gate of the devices connects to the horizontal lead which is orthogonal to the radiated field. Several gate-feedback grid oscillators have been successul [3].
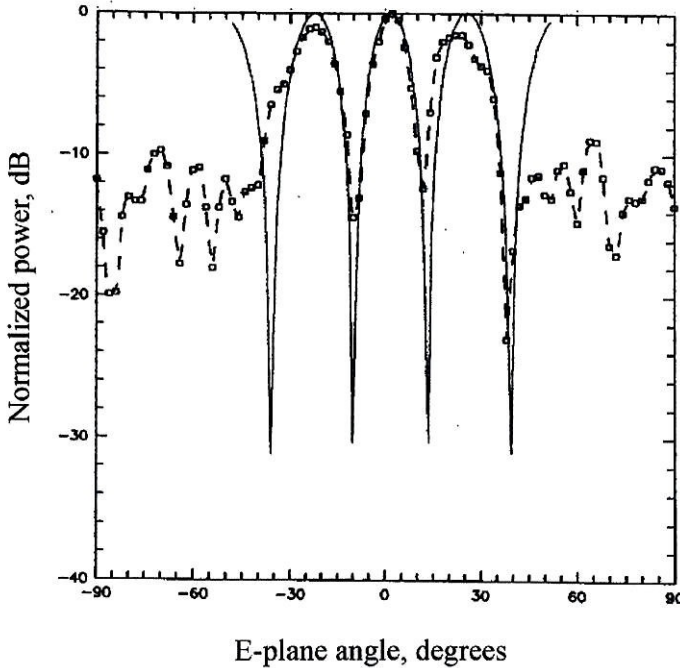
Fig. 5.3. E-plane radiation pattern of a 36-element monolithic grid oscillator operating at 35 GHz [5]. The solid line is the E-pattern of two sources 20 mm apart. The dashed line is the measurement.

Using this approach a 100-MESFET power grid oscillator produced 10 W at 10 GHz [4]. A 36-element HBT monolithic grid was demonstrated that oscillated at 35 GHz [5,6]. The E-plane radiation pattern of this grid is shown in Fig. 5.3. The side-lobes have a peak value only 2 dB less than the main-lobe peak. D.W. Griffin [7] pointed out that the unsatisfactory E-plane pattern is due to substrate-mode excitation that contributes to the radiation pattern through the edges of the grid. This chapter will present the design and performance of a 36-element InP HEMT grid oscillator. The motivation behind this work is to minimize the power in the substrate modes and produce an E-field with low side-lobes.

5.2. Grid Design and Construction
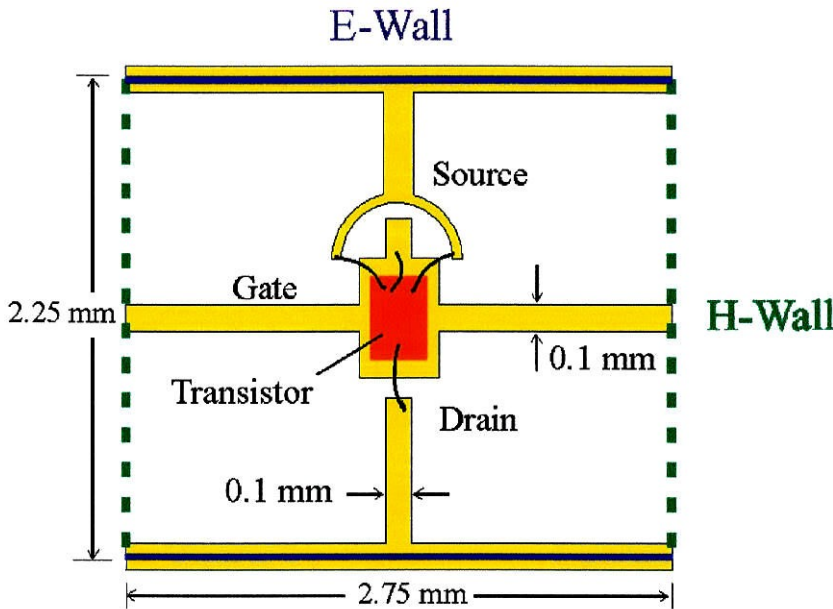
Fig. 5.4. The equivalent waveguide unit cell. Electric walls (solid lines) and magnetic walls (dashed lines) are imposed by symmetry on the boundaries of the unit cell. The drain and source of the devices are wire-bonded to the vertical leads. The gate is wire-bonded to the horizontal leads.

The active devices are AlInAs/GaInAs on InP HEMT's fabricated at Hughes Research Laboratories. The HEMT's have a total gate width of $75\,\mu$m [8,9]. The devices have a peak transconductance of $848\,$mS/mm and a full channel current of $750\,$mA/mm measured at a gate bias of $0.2\,$V and a drain bias of $1.5\,$V. In order to analyze the grid we assume that all devices are identical. Each device lies in an equivalent waveguide unit cell which is defined by the symmetry of the grid. This equivalent unit cell has magnetic walls on the sides and electric walls on the top and the bottom as shown in Fig. 5.4. The vertical spacing determines the excitation of TM modes and the horizontal spacing determines the TE mode power. We calculated the substrate-mode power for a 6×6 array of uniformly excited dipoles and another array with alternating 180° phase shifts. We selected spacings that gave low substrate-mode power levels. The period of the grid and the electrical thickness of the substrate, control the substrate-mode excitation. To minimize the power in the substrate modes we use a thin $(254\,\mu$m) Duroid substrate with a dielectric constant of 2.2. This gives an electrical thickness at the oscillation frequency of only 19°. We also chose the vertical and horizontal period of the grid to minimize substrate-mode excitation. A photograph of the grid is shown in Fig. 5.6. The devices are mounted onto an etched Duroid substrate. They are arranged such that adjacent rows share bias lines. The stubs along the upper and lower rows of the grid are an effective quarte-wavelength. These stubs present a low rf impedance as required by the electric wall boundary condition. The entire grid can be biased either with a single or multiple dc supplies. A Photograph of a HEMT attached to the etched substrate is shown in Fig. 5.5.

The transmission-line equivalent circuit is shown in Fig. 5.7. The inductances and capacitances shown are calculated using the EMF method [10,11]. Free space is represented by 377-Ω scaled by the aspect ratio b/a of the unit cell. The approach suggested by Martinez and Compton [12], is used to analyze the equivalent circuit.
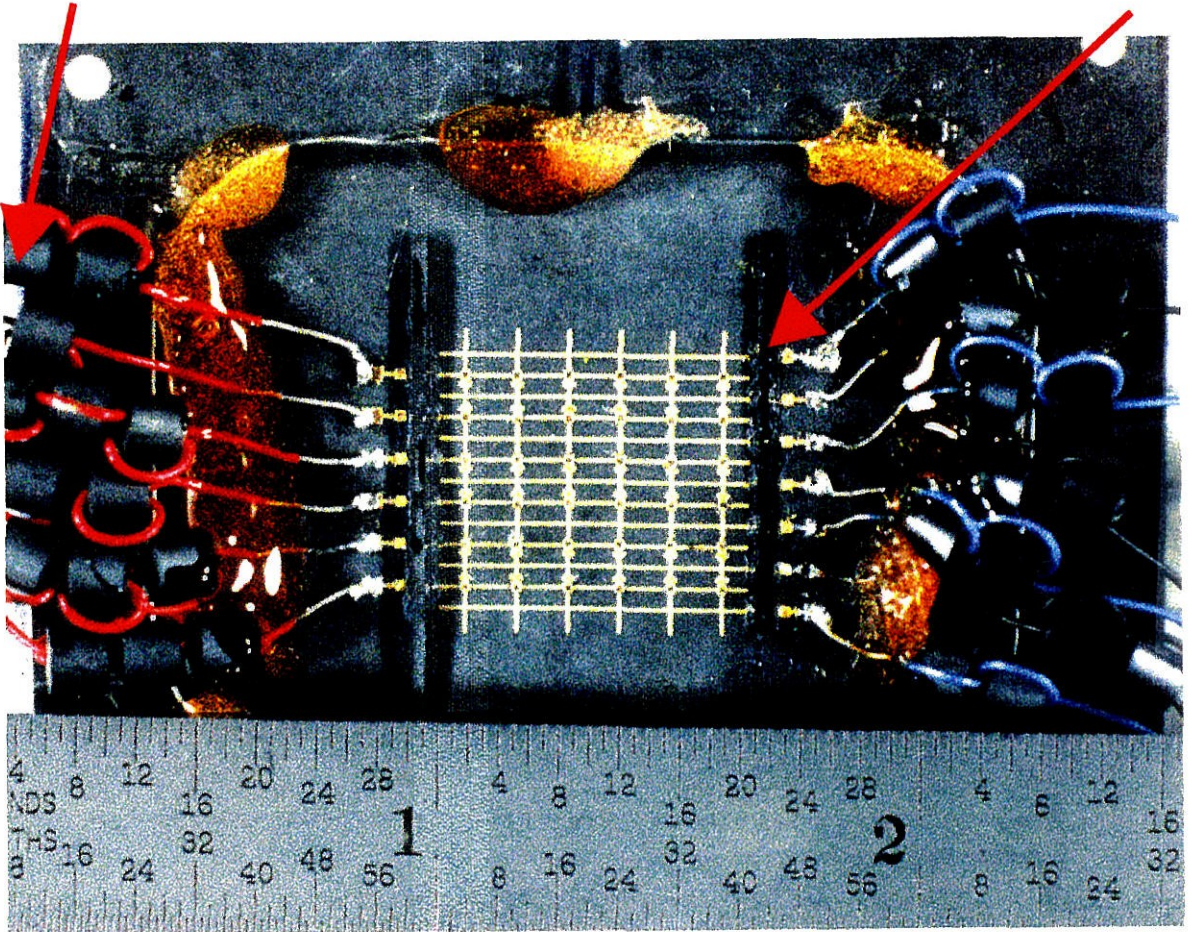
Fig. 5.5. Photograph of the 36-element hybrid HEMT grid oascillator. The horizontal lines are bias lines. Ferrite slabs are placed on each side of the grid underneath the bond wires to suppress oscillations at low frequencies. Ferrite beads are also added along the leads to suppress bias line oscillations.
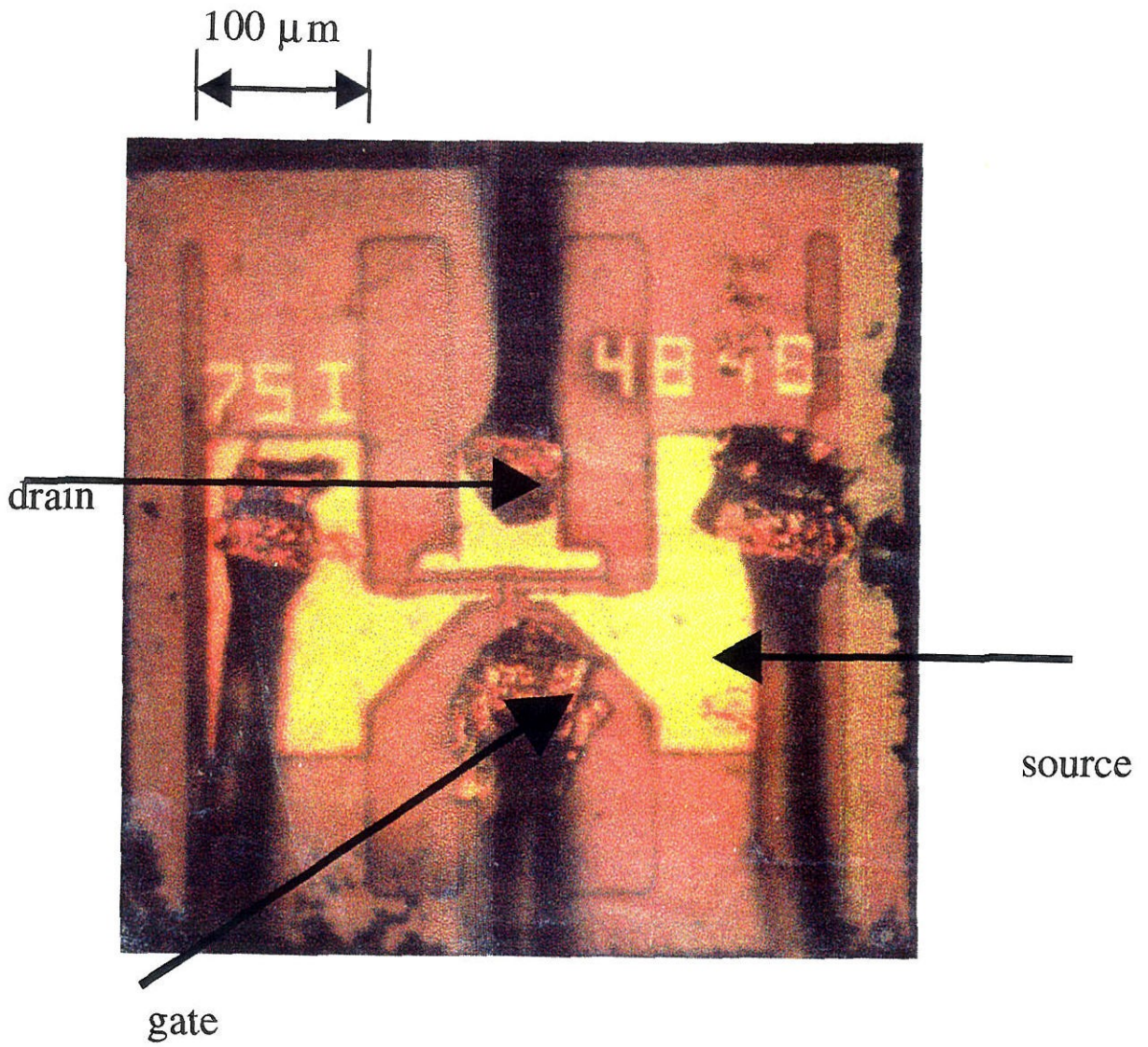
100 μm

drain

source

gate

Fig. 5.6. Photograph of an active chip attached to the etched substrate.

A circulator is inserted at the drain terminal to calculate the saturated circular function, that is the reflection coefficient from the circulator. The circular function can be thought of as a measure of the open loop gain of the circuit. The locus of the function crosses the zero-phase, unity-magnitude point at 44.3 GHz, indicating an oscillation at this frequency. Fig. 5.11 shows the saturated circular function of the grid. Saturation of the transistor is modelled by reducing the magnitude of s_{21} [13].
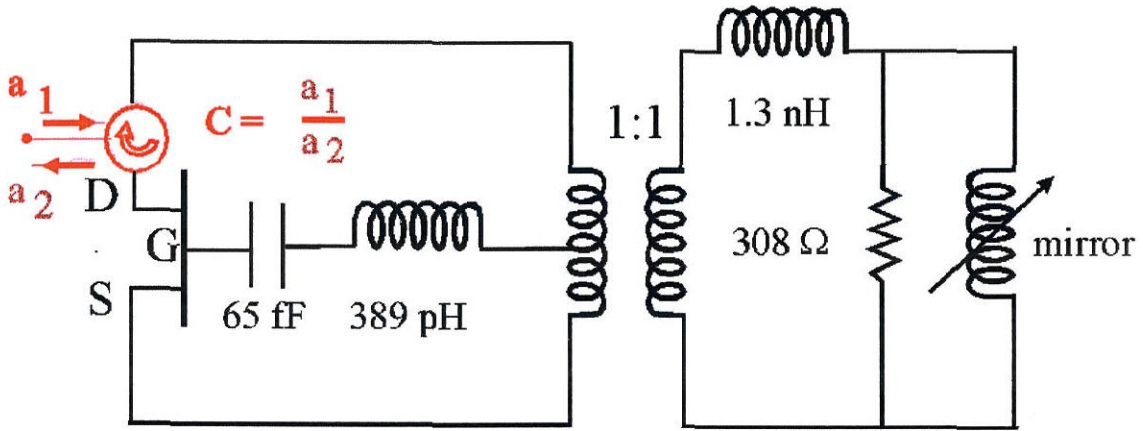
Fig. 5.7. Transmission-line equivalent circuit. The reflection coefficient at the circulator terminal calculates the circular function. The reactance of the mirror is determined by the thickness of the substrate and the spacing from the grid.
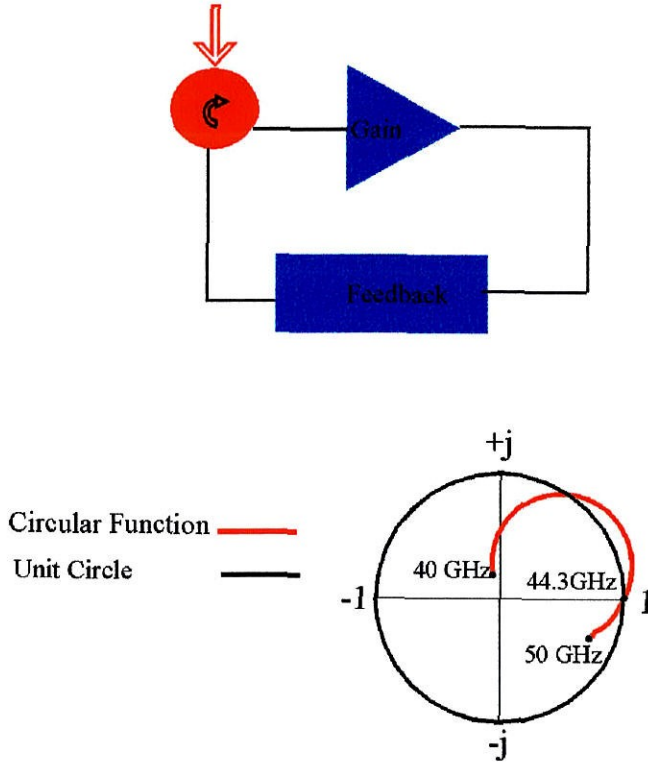
Fig. 5.8. Saturated circular function, C, of the grid. The oscilation criterion is satisfied at 44.3 GHz, where $C=1$.

5.3. MEASUREMENTS

An HP8563A spectrum analyzer with an HP11974-series preselected mixer was used to measure the oscillation spectrum of the grid (Fig.7). An output tuner was placed in front of the grid that stabilized the signal and maximized the output power. The tuner used is a $\lambda_0/4$-thick dielectric slab with a dielectric constant of 10.5 placed 6.5 mm in front of the grid. All devices in a single row are biased in parallel. Four separate dc supplies are used (one for each of the top and

bottom rows, one for rows 2 and 3, and another for rows 4 and 5). The separate
supplies allowed us to control the angle of the beam. The oscillation frequency
is 43 GHz, about 3% lower than the design frequency, 44.3 GHz. The spectrum
is very clean and this indicates that the devices are properly locked. A figure of
merit for quasi-optical sources is the Effective Radiated Power (ERP) [11]. The
ERP is the power an isotropic source would have to radiate to give the same
power density. ERP is given by the following formula:

$$\text{ERP} = P_{meas}\frac{4\pi R^2}{A_{ant}}, \tag{5.1}$$

where A_{ant} is the effective area of the receiving antenna and R is the distance
separating the antenna and the grid. P_{meas} is the power measured in the spectrum
analyzer.
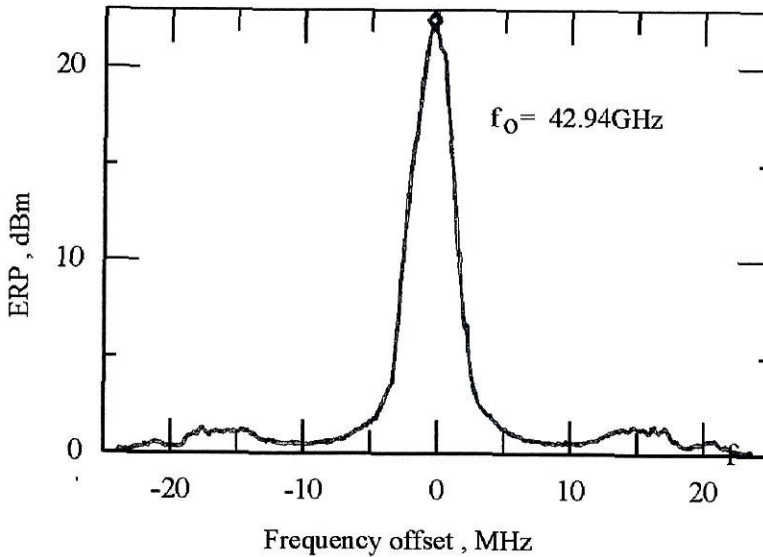
Fig. 5.9. Oscillation spectrum.

The highest effective radiated power (ERP) is 200 mW. The effective transmitter power (ETP) defined by Gouker [14] is low, only 5 mW. The ETP is related to ERP by:

$$\text{ETP} = \frac{\text{ERP}\lambda^2}{4\pi A_{array}} \tag{5.2}$$

where A_{array} is the physical area of the grid and λ is the free-space wavelength. The total dc power supplied was 272 mW.
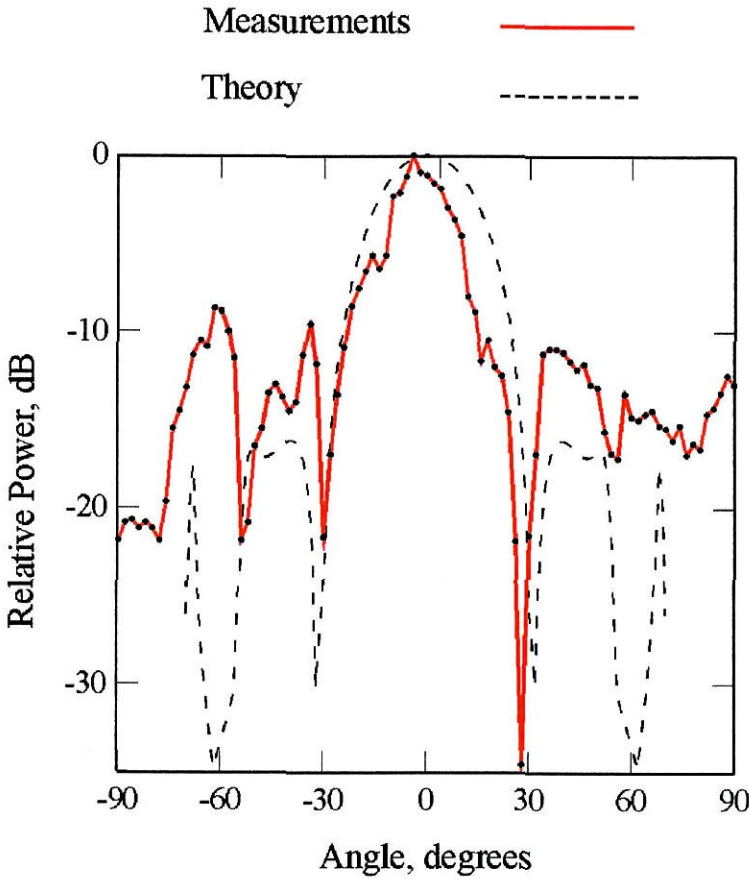
Fig. 5.10. Measured E-plane radiation pattern (solid line) with 6 mm mirror spacing and theoretical pattern (dashed line) with 5.8 mm mirror spacing.

The far-field radiation patterns of the grid were measured and are shown in Fig. 8. The theoretical patterns are for a uniformly excited array of 36 short dipoles spaced 2.75 mm apart in the H-plane and 2.25 mm apart in the E-plane and placed 5.8 mm in front of a mirror. Both E and H-plane patterns have side lobes about 10 dB lower than the main beam. No evidence of substarte-modes is seen. By changing the position of the mirror and the tuning slab the oscillator can be tuned to operate at other frequencies and different power levels. These tuning curves are shown in Fig. 9. The ERP and frequency repeat at half-wavelength intervals.
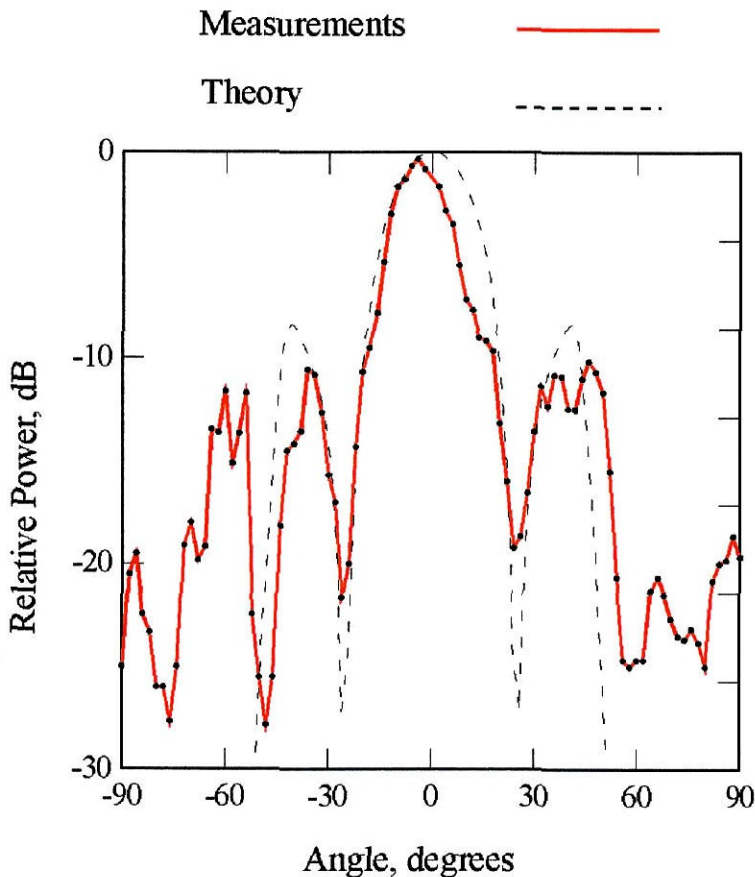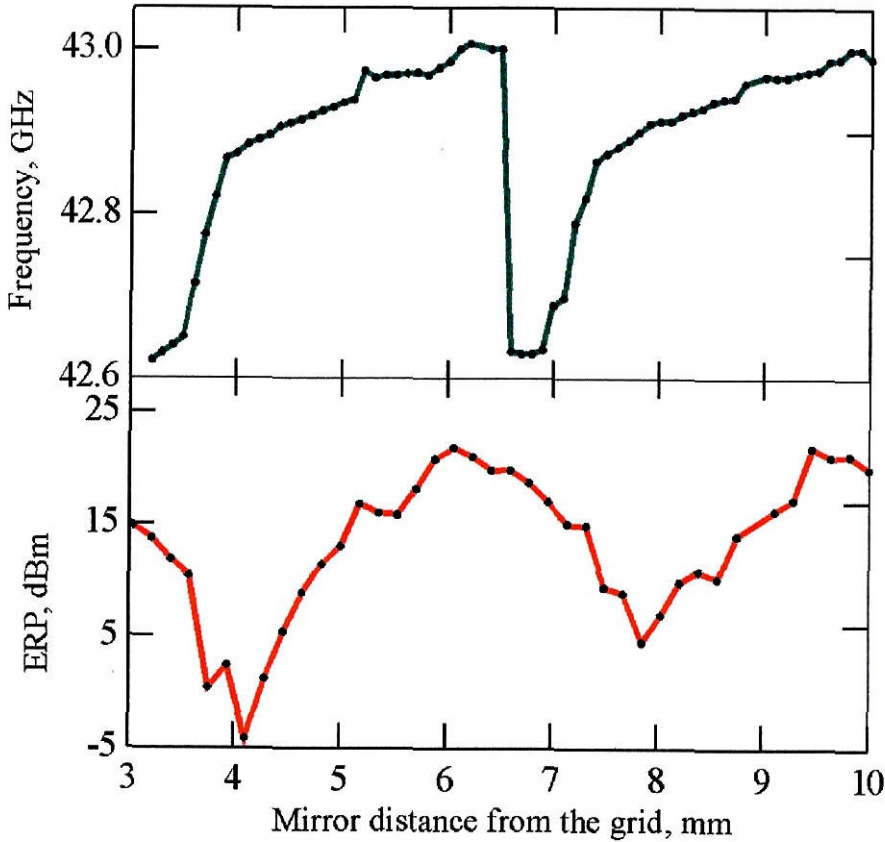

Fig. 5.11. Measured H-plane radiation pattern (solid line) with 6 mm mirror spacing and theoretical pattern (dashed line) with 5.8 mm mirror spacing.

Fig. 5.12. Frequency and power tuning of the grid as a function of mirror position For these measurements a dielectric slab was placed 6.5 mm in front of the grid.

5.4 SUMMARY

A 43-GHz 36-element grid oscillator has been demonstrated with an ERP of 200 mW. The grid was designed to reduce substrate-mode excitation that had plagued previous grids. No evidence of substrate modes was seen in the patterns. This grid also demonstrated that hybrid circuit techniques can be used for quasi-optical grids at millimeter-wave frequencies. The electrical thickness

and the geometry of the array (spacing of the devices) can control the excitation of substrate modes.

References

[1] Z.B. Popović, M. Kim, D.B. Rutledge, "Grid Oscillators," *Int. J. Infrared Millimeter Waves,* vol. 9, no. 7, pp. 647-654, 1988.

[2] Z.B. Popović, R.M. Weikle, M. Kim, D.B. Rutledge, "A 100-MESFET Planar Grid Oscillator," *IEEE Trans. Microwave Theory Tech., MTT–39.,* pp. 193-200, Feb. 1991.

[3] R.M. Weikle, M. Kim, J.B. Hacker, M.P. De Lisio, D.B. Rutledge, "Planar MESFET Grid Oscillators Using Gate Feedback," *IEEE Trans. Microwave Theory Tech.,* vol. 40, pp. 1997-2003, Nov. 1992.

[4] J.B. Hacker, M.P. De Lisio, M. Kim, C.-M. Liu, S.-J. Li, S.W. Wedge, D.B. Rutledge, "A 10-Watt X-Band Grid Oscillator," *1994 IEEE MTT–S Int. Microwave Symp. Dig.,* pp. 823-826, 1994.

[5] M. Kim, E.A. Sovero, R.M. Weikle, J.B. Hacker, M.P.De Lisio, D.B. Rutledge, "A 35 GHz HBT Monolithic Grid Oscillator," *Proc. SPIE, 17th Int. Conf. on Infrared and Millimeter Waves,* R.J. Temkin, Ed., pp. 402-403, 1992.

[6] M. Kim, "Grid Amplifiers," Ph.D. Thesis, California Institute of Technology, Pasadena, CA, 1993

[7] D.W. Griffin, "Monolithic Active Array Limitation Due to Substrate Modes," *1995 IEEE AP–S Int. Symp. Dig.,* pp. 1300-1303, 1995.

[8] M. Matloubian, L. Jelloian, A.S. Brown, L.D. Nguyen, L.E. Larson, M.J. Delaney, M.A. Thompson, R.A. Rhodes, J.E. Pence, "V-Band High-Efficiency High-Power AlInAs/GaInAs/InP HEMT's," *IEEE Trans. Microwave Theory Tech., MTT–41.,* pp. 2206-2210, Dec. 1993.

[9] M. Matloubian, L.D. Nguyen, A.S. Brown, L.E. Larson, M.A. Melendes, M.A. Thompson, "High Power and High Efficiency AlInAs/GaInAs on InP HEMTs," *1991 IEEE MTT–S Int. Microwave Symp. Dig. Vol. 2,* pp. 721-724, 1991.

[10] R.M. Weikle, "Quasi-optical planar grids for Microwave and Millimeter-

wave Power Combining," Ph.D. Thesis, California Institute of Technology, Pasadena, CA, 1992.

[11] R.M. Weikle, Z.B. Popović, W.A. Shiroma, "Grid Oscillators," *Active and Quasi-Optical Arrays for Solid State Power Combining,* John Wiley & Sons, Inc., 1997.

[12] R.D. Martinez, R.C. Compton, "A General Approach for the S-Parameter Design of Oscillators with 1 and 2-Port Active Devices," *IEEE Trans. Microwave Theory Tech., MTT–40.,* pp. 569-574, March 1992.

[13] K.M. Johnson, "Large Signal GaAs MESFET Oscillator Design," *IEEE Trans. Microwave Theory Tech., MTT–27.,* pp. 217-227, March 1979.

[14] M. Gouker, "Toward Standard Figures-of-Merit for Spatial and Quasi-Optical Power-Combined Arrays," *IEEE Trans. Microwave Theory Tech., MTT–43.,* pp. 1614-1617, July 1995.